

NUMERICAL MODELING OF GENERAL COMPRESSIBLE MULTI-PHASE  
FLOWS

A THESIS SUBMITTED TO  
THE GRADUATE SCHOOL OF NATURAL AND APPLIED SCIENCES  
OF  
MIDDLE EAST TECHNICAL UNIVERSITY

BORA KALPAKLI

IN PARTIAL FULFILLMENT OF THE REQUIREMENTS  
FOR  
THE DEGREE OF DOCTOR OF PHILOSOPHY  
IN  
ENGINEERING SCIENCES

OCTOBER 2013

Approval of the thesis:

**NUMERICAL MODELING OF GENERAL COMPRESSIBLE MULTI-PHASE  
FLOWS**

submitted by **BORA KALPAKLI** in partial fulfillment of the requirements for the degree of **Doctor of Philosophy in Engineering Sciences Department, Middle East Technical University** by,

Prof. Dr. Canan Özgen  
Dean, Graduate School of **Natural and Applied Sciences**

\_\_\_\_\_

Prof. Dr. Murat Dicleli  
Head of Department, **Engineering Sciences**

\_\_\_\_\_

Prof. Dr. Hakan I. Tarman  
Supervisor, **Engineering Sciences, METU**

\_\_\_\_\_

Prof. Dr. Yusuf Özyörük  
Co-supervisor, **Department of Aerospace Engineering, METU**

\_\_\_\_\_

**Examining Committee Members:**

Prof. Dr. İsmail Hakkı Tuncer  
Department of Aerospace Engineering, METU

\_\_\_\_\_

Prof. Dr. Hakan I. Tarman  
Engineering Sciences, METU

\_\_\_\_\_

Assoc. Prof. Dr. Cüneyt Sert  
Mechanical Engineering, METU

\_\_\_\_\_

Assoc. Prof. Dr. Utku Kanoğlu  
Engineering Sciences, METU

\_\_\_\_\_

Prof. Dr. Ünver Kaynak  
Mechanical Engineering, TOBB ETU

\_\_\_\_\_

**Date:**

\_\_\_\_\_

**I hereby declare that all information in this document has been obtained and presented in accordance with academic rules and ethical conduct. I also declare that, as required by these rules and conduct, I have fully cited and referenced all material and results that are not original to this work.**

Name, Last Name: BORA KALPAKLI

Signature :

## ABSTRACT

### NUMERICAL MODELING OF GENERAL COMPRESSIBLE MULTI-PHASE FLOWS

Kalpaktı, Bora

Ph.D., Department of Engineering Sciences

Supervisor : Prof. Dr. Hakan I. Tarman

Co-Supervisor : Prof. Dr. Yusuf Özyörük

October 2013, 149 pages

In this thesis, some novel methods for solution of compressible, multi-phase flows on unstructured grids were developed. The developed methods are especially advantageous for interface problems, while they are also applicable to multi-phase flows containing mixtures as well as particle suspensions. The first method studied was a multi-dimensional, multi-phase Godunov method for compressible multi-phase flows. This method is based on the solution of a hyperbolic equation system for compressible multi-phase flows. There are several difficulties with this hyperbolic equation system due to non-conservative volume fraction equation and non-conservative terms also known as throttling terms existing in momentum and energy equations. Robust and accurate multi-dimensional discretization of these terms were derived based on Abgrall [1] criterion. Next a new method based on discrete equations for multi-dimensional and multiphase problems on unstructured grids was developed. This method resolves all the problems associated with the non-conservative equations and terms. The high artificial numerical mixing of phase interfaces associated with available compressible schemes was resolved with a novel volume fraction differencing

scheme. The developed differencing scheme used for volume fraction is the only scheme providing comparable resolution of the interfaces with tracking methods on multi-dimensional unstructured grids and very robust compared to other interface capturing methods studied in the related literature. The resulting methods provide ignorable numerical mixing of phase interfaces on unstructured solution grids while giving physically correct results for pressure and energy in contrast to other methods available in the literature.

In addition to these solution methods, some special boundary conditions and preconditioning methods for low speed steady flows were applied. For high spatial resolution, combinations of linear reconstruction and Weighted Average Flux (WAF) methods were also applied in some problems.

**Keywords:** Compressible flow, Multi-phase , Particulate, Shock waves, Interface Capturing

## ÖZ

### GENEL SIKIŞTIRILABİLİR ÇOK FAZLI AKIŞLARIN SAYISAL MODELLENMESİ

Kalpaklı, Bora

Doktora, Mühendislik Bilimleri Bölümü

Tez Yöneticisi : Prof. Dr. Hakan I. Tarman

Ortak Tez Yöneticisi : Prof. Dr. Yusuf Özyörük

Ekim 2013 , 149 sayfa

Bu tezde, sıkıştırılabilir çok fazlı akışların çözümü için yeni sayısal yöntemler geliştirilerek yapısal olmayan çözüm ağlarına uygulanmıştır. Geliştirilen yöntemler özellikle arayüz problemleri için uygun olmasına rağmen karışım ve partiküllü akışlara da uygulanabilmektedir. Çalışmada ilk olarak bazı matematiksel ve sayısal formülasyonların çıkarılması için çalışıldı. Bu çalışma sonucunda elde edilen yöntemler üç başlıkta toplanabilir; 1. Çok fazlı sıkıştırılabilir akışları tanımlayan bir hiperbolik denklem sisteminin çözümü, 2. Seyreltik faz yakalşımının yapıldığı bir çözücü, 3. Ayrık korunum denklemlerine dayanan sonlu hacimler çözücüsü. Ek olarak yüksek çözünürlüklü bir arayüz yakalama yöntemi geliştirilerek ayrık korunum denklemlerine uygulanmıştır. Elde edilen yöntemlerin kararlı olduğu ve fiziksel olarak doğru sonuçlar sağladığı gözlenmiştir. Literatürde var olan ara yüz yakalama yöntemlerinin tersine, faz ara yüzleri mümkün olan en yüksek çözünürlükte arayüz izleme yöntemleri ile karşılaştırılabilir doğrulukta çözülebilmektedir. Bu tür sıkıştırılabilir çok fazlı problemler için geliştirilmiş olan yöntemlerde karşılaşılan ve korunumsuz denklem ve

terimlerle ilişkilendirilen sorunlar, bu tezde geliştirilen yöntemlerle saf dışı bırakılmışlardır.

Bunlara ek olarak bazı özel sınır koşulları ve düşük Mach sayılı akışlar için ön koşullandırma yöntemleri uygulanmıştır. Uzaysal yüksek çözünürlük için doğrusal yeniden yapılandırma ve ağırlıklı ortalama akı yöntemleri birleştirilmiştir.

Anahtar Kelimeler: Sıkıştırılabilir akış, Çok fazlı, Parçıklı akış, Şok dalgaları, Arayüz yakalama

*To my family.*

## **ACKNOWLEDGMENTS**

I would like to thank my supervisor Professor Hakan I. Tarman and co-supervisor Professor Yusuf Özyörük for their constant support and guidance. I also would like to thank Professor İsmail H. Tuncer and Utku Kanođlu for their guidance.

# TABLE OF CONTENTS

ABSTRACT . . . . .	iv
ÖZ . . . . .	vi
ACKNOWLEDGMENTS . . . . .	ix
TABLE OF CONTENTS . . . . .	x
LIST OF TABLES . . . . .	xvi
LIST OF FIGURES . . . . .	xvii
CHAPTERS	
1 INTRODUCTION . . . . .	1
1.1 Categorization of Compressible Multi-phase Problems . . . . .	1
1.2 Characteristics of Compressible Multi-phase Flows From Computational Point of View . . . . .	3
1.3 Related Literature . . . . .	5
1.4 Methodology and Outline of The Thesis . . . . .	8
1.5 Basic Numerical And Coding Framework . . . . .	9
2 NUMERICAL METHODS FOR SINGLE PHASE FLOWS . . . . .	11
2.1 Discretization of Euler Equations With Finite Volume Method (FVM) . . . . .	11
2.1.1 Coordinate Rotation . . . . .	13
2.2 The Split Multi-Dimensional Riemann Problem . . . . .	16

2.3	Explicit Scheme with Rusanov and Lax-Friedrich Fluxes . . .	17
2.4	HLL and HLLC Approximate Riemann Solvers for Approximate Godunov Methods . . . . .	19
2.5	Axisymmetric Flows . . . . .	21
2.6	Explicit Time Stepping . . . . .	23
2.7	Preconditioning For Low-Mach Number Flows . . . . .	23
2.8	Calculation of Time Steps . . . . .	25
2.9	Weighted Average Flux (WAF) Methods For High-Order Accuracy . . . . .	26
2.9.1	WAF Version of HLL Riemann Solver . . . . .	26
2.10	Unstructured Data Reconstruction for Higher Order Accuracy	30
2.11	Boundary Conditions . . . . .	32
2.11.1	Mass Flow Inlet . . . . .	32
2.11.2	Pressure Outlet . . . . .	34
2.11.3	Pressure Inlet . . . . .	35
2.11.4	Subsonic Pressure Inlet . . . . .	35
2.11.4.1	Supersonic Pressure Inlet . . . . .	36
2.11.5	Inviscid Wall . . . . .	36
2.11.6	Symmetry Boundary Condition . . . . .	37
2.11.7	Far Field Boundary Conditions . . . . .	37
2.11.8	Far Field Supersonic Inflow . . . . .	37
2.11.8.1	Far Field Subsonic Inflow . . . . .	38
2.11.8.2	Far Field Subsonic Outflow . . . . .	39
2.12	Single Phase Test Cases . . . . .	39

	2.12.1	Cylindrical Explosion in Two-Space Dimension . . .	40
	2.12.2	Spherical Explosion In Three Space Dimensions . . .	43
	2.12.3	Supersonic Flow Over a Circular Arc Bump . . . . .	47
	2.12.4	Transonic Flow Over Circular Bump . . . . .	48
	2.12.5	Blast Propagation In A Three Dimensional L-Shaped Tunnel . . . . .	50
3		MULTIDIMENSIONAL MULTI-PHASE GODUNOV METHODS FOR COMPRESSIBLE MULTI-PHASE FLOWS . . . . .	57
	3.1	Numerical Method . . . . .	59
	3.1.1	Non-conservative Terms . . . . .	59
		3.1.1.1 Godunov-Rusanov Scheme . . . . .	60
		3.1.1.2 Gradient of Gas Volume Fraction $\alpha$ . . . . .	61
		3.1.1.3 Discretization of Volume Fraction Equation . . . . .	62
		3.1.1.4 Godunov-HLL Scheme . . . . .	63
	3.2	Velocity Relaxation Procedure For Interface Problems . . . . .	64
	3.3	Pressure Relaxation . . . . .	67
		3.3.1 Solution Procedure . . . . .	70
4		DISCRETE APPROACH FOR COMPRESSIBLE MULTI-PHASE FLOWS . . . . .	73
	4.1	Wave Patterns in a multi-phase Mixture . . . . .	74
	4.2	Wave Patterns at an Interface Separating Two Pure Fluids . . . . .	75
	4.3	Definitions and Assumptions . . . . .	75
		4.3.1 Riemann Problem at a Cell Face . . . . .	77
	4.4	Solution of Riemann Problem By Utilizing HLLC Solver . . . . .	78

4.4.1	$(\Sigma_i, \Sigma_i)$ Interface . . . . .	79
4.4.2	$(\Sigma_i, \Sigma_j), i \neq j$ Interface . . . . .	79
4.4.3	$(\Sigma_j, \Sigma_i), j \neq i$ Interface . . . . .	81
4.4.4	Fluxes For Godunov Method . . . . .	81
4.5	Multifluid Test Cases . . . . .	82
4.5.1	Water/Air Shock Tube Problem . . . . .	82
4.5.2	Under Water Explosion . . . . .	82
5	METHODS FOR HIGHLY DILUTED MULTI-PHASE FLOWS . . . . .	89
5.1	Interface Drag . . . . .	91
5.2	Drag Models . . . . .	92
5.3	Inter-phase Heat Transfer . . . . .	93
5.4	Particle Phase Boundary Conditions . . . . .	94
5.4.1	Inlet Conditions . . . . .	94
5.4.2	Outlet Conditions . . . . .	94
5.5	Test Cases of Dilute Particle Phase Model . . . . .	94
5.5.1	Attenuation and Dispersion of Acoustic Waves by Particulate-relaxation Processes [27] . . . . .	94
5.5.1.1	Main Hypothesis . . . . .	95
5.5.1.2	Theoretical Development of The Test Case . . . . .	96
5.5.1.3	Attenuation and Dispersion Due to Nu- merical Diffusion . . . . .	99
5.5.1.4	Numerical Test Case . . . . .	99
5.5.1.5	Results . . . . .	101

5.5.2	Simulation of Two Phase Inert Tep [27]	103
5.5.2.1	Geometry and Grid	103
5.5.2.2	Boundary Conditions	104
5.5.2.3	Material Properties	105
5.5.2.4	Heat and Momentum Transfer Terms	105
5.5.2.5	Results	106
5.5.2.6	Comparison of Data on Plane i=10	106
5.5.2.7	Comparison of Data on Plane i=98	106
5.5.2.8	Discussion of TEP Test Case Results	116
6	HIGH RESOLUTION INTERFACE CAPTURING	121
6.1	Discretization of Volume Fraction	121
6.1.1	Definitions	121
6.1.2	Compressible High Resolution Interface Capturing (CHRIC) Scheme	124
6.1.3	Calculation of Downwind Face Volume Fraction $\alpha_{fU}$	126
6.1.4	Calculation of Face Courant Number	127
6.2	Volume Fraction Discretization On Multi-dimensional Unstructured Grids	127
6.2.1	Calculation of Upwind And Downwind Volume Fractions	128
6.2.2	Calculation of Face Courant Number	129
6.3	Considerations for Dilute Particulate Phases	130
6.4	The Algorithm	131
6.5	Test Cases for CHRIC Scheme	132

6.5.1	1D Water/Air Shock Tube Problem . . . . .	132
6.5.2	Under Water Explosion . . . . .	134
6.5.3	Liquid-Gas Interface Tangential Shock Wave Problem . . . . .	135
6.5.4	Highly Diluted multi-phase Test Cases . . . . .	138
6.5.4.1	Attenuation of Acoustic Waves by Suspended Particles . . . . .	138
6.5.4.2	Internal Ballistics of A Solid Propellant Rocket Motor . . . . .	141
7	CONCLUSION . . . . .	143
	REFERENCES . . . . .	145
	CURRICULUM VITAE . . . . .	149

## LIST OF TABLES

### TABLES

Table 2.1 Properties of plastic explosive and the calculated initial values for modeling the explosion. . . . .	50
Table 5.1 Gas and particle properties. . . . .	101
Table 5.2 Boundary conditions. . . . .	105
Table 5.3 Material Properties. . . . .	105

## LIST OF FIGURES

### FIGURES

Figure 1.1 Schematic representation of different multi-phase flows. [42]. . . . .	2
Figure 1.2 Schematic representation of the equivalence between a bubbly flow or a droplet flow with a stratified flow [2]. . . . .	7
Figure 2.1 Example of two dimensional quadrilateral and triangular computa- tional cells. . . . .	12
Figure 2.2 Structure of the solution of the three-dimensional $\hat{x}$ split Riemann problem. . . . .	18
Figure 2.3 The solution of the Riemann problem and the domain of the integral.	27
Figure 2.4 Far field inflow boundary. . . . .	38
Figure 2.5 Far field outflow boundary. . . . .	39
Figure 2.6 The unstructured multi zone grid structure and initial gauge pres- sure distribution. . . . .	40
Figure 2.7 Cylindrical explosion in two-space dimensions. Pressure distribu- tion at $7.7 \times 10^{-4}$ seconds calculated by the first order solver using HLLC Riemann solver. . . . .	41
Figure 2.8 Cylindrical explosion in two-space dimensions. Density distribu- tion at $7.7 \times 10^{-4}$ seconds calculated by the first order solver of CMPS using HLLC Riemann solver. . . . .	41

Figure 2.9 Cylindrical explosion in two-space dimensions. $x$ velocity distribution at $7.7 \times 10^{-4}$ seconds calculated by the first order solver of CMPS using HLLC Riemann solver. . . . .	42
Figure 2.10 Cylindrical explosion in two-space dimensions. Pressure distributions at $7.7 \times 10^{-4}$ seconds calculated by the first order solvers of CMPS using different flux functions. The solution with Roe solver is the result of FLUENT's first order explicit solver. . . . .	42
Figure 2.11 Cylindrical explosion in two-space dimensions. $x$ pressure distribution at $7.7 \times 10^{-4}$ seconds calculated by the high order solvers of CMPS.	43
Figure 2.12 Spherical explosion in three space dimensions. Initial pressure distribution and grid structure. The spherical zone at the center is the initial high pressure region. . . . .	44
Figure 2.13 Spherical explosion in three space dimensions. Pressure distribution at time $t = 4.7 \times 10^{-4}$ calculated with first order solver of CMPS using HLLC Riemann solver. . . . .	44
Figure 2.14 Spherical explosion in three space dimensions. Density distribution at time $t = 4.7 \times 10^{-4}$ calculated with first order solver of CMPS using HLLC Riemann solver. . . . .	45
Figure 2.15 Spherical explosion in three space dimensions. Internal energy distribution at time $t = 4.7 \times 10^{-4}$ calculated with first order solver of CMPS using HLLC Riemann solver. . . . .	45
Figure 2.16 Spherical explosion in three space dimensions. Density distributions at time $t = 4.7 \times 10^{-4}$ calculated with first order solver of CMPS using HLLC Riemann solver and first order solver of FLUENT using Roe.	46
Figure 2.17 Cylindrical explosion in two-space dimensions. $x$ pressure distribution at $7.7 \times 10^{-4}$ seconds calculated by the high order solvers of CMPS.	47
Figure 2.18 Mach number contours for supersonic flow over a circular bump calculated with first order HLLC Riemann solver of CMPS code. . . . .	48

Figure 2.19 Mach number along the supersonic flow over a circular bump shown in Fig. 2.18. . . . .	48
Figure 2.20 Pressure profile along the supersonic flow over a circular bump shown in Fig. 2.18 . . . . .	49
Figure 2.21 Mach number contours for transonic flow over a circular bump calculated with first order HLLC Riemann solver of CMPS code. . . . .	49
Figure 2.22 Mach number along the transonic flow over the bump shown in Fig. 2.21. . . . .	50
Figure 2.23 Geometry of the test case for blast wave propagation in L-Shaped tunnel. . . . .	51
Figure 2.24 Mach number contours at time $t = 0.30 \times 10^{-3}$ seconds. . . . .	52
Figure 2.25 Absolute pressure contours at time $t = 0.30 \times 10^{-3}$ seconds. . . . .	52
Figure 2.26 Mach number contours at time $t = 0.43 \times 10^{-3}$ seconds . . . . .	53
Figure 2.27 Absolute pressure contours at time $t = 0.43 \times 10^{-3}$ seconds. . . . .	53
Figure 2.28 Pressure probe at probe 1. . . . .	54
Figure 2.29 Pressure probe at probe 2. . . . .	54
Figure 2.30 Pressure probe at probe 3. . . . .	55
Figure 4.1 Rarefaction (R), contact (C) and shock (S) wave pattern in a compressible two phase mixture. Superscripts l and g denote liquid and gas phases respectively. . . . .	74
Figure 4.2 Rarefaction (R), contact (C) and shock (S) wave pattern at an interface. Superscripts l and g denote liquid and gas phases respectively. . . . .	75
Figure 4.3 Some of possible phase interface configurations at cell face. . . . .	77
Figure 4.4 Wave and phase patterns ignoring relaxation processes at a short time after $t = 0$ . . . . .	78

Figure 4.5	Solutions for water/air shock tube test problem at $t = 229 \times 10^{-6}$ s.	83
Figure 4.6	Solutions for water/air shock tube test problem at $t = 229 \times 10^{-6}$ s.	84
Figure 4.7	Volume fractions of water at times $t = 100 \times 10^{-6}$ , $t = 240 \times 10^{-6}$ , $t = 340 \times 10^{-6}$ and $t = 680 \times 10^{-6}$ seconds.	85
Figure 4.8	Water mixture densities at times $t = 100 \times 10^{-6}$ , $t = 240 \times 10^{-6}$ , $t = 340 \times 10^{-6}$ and $t = 680 \times 10^{-6}$ seconds	86
Figure 4.9	Mixture pressures at times $t = 100 \times 10^{-6}$ , $t = 240 \times 10^{-6}$ and $t = 340 \times 10^{-6}$ seconds	87
Figure 4.10	Mixture velocities at times $t = 100 \times 10^{-6}$ , $t = 240 \times 10^{-6}$ and $t = 340 \times 10^{-6}$ seconds	88
Figure 5.1	Attenuation of sound waves due to $15\mu\text{m}$ diameter particles [14].	99
Figure 5.2	Attenuation of sound waves due to numerical diffusion with differ- ent numerical schemes.	100
Figure 5.3	Schematic representation of the test case for propagation of sound waves in a channel including suspended particles.	100
Figure 5.4	Attenuation by particles of different diameters.	102
Figure 5.5	Dispersion by particles of different diameters.	103
Figure 5.6	Grid structure given by ONERA[14]	104
Figure 5.7	Boundary zones[14]	104
Figure 5.8	Grid points for comparison of results[14]	107
Figure 5.9	Axial velocities over line $i=10$ [27]	107
Figure 5.10	Radial velocities over line $i=10$ [27]	108
Figure 5.11	Gas temperatures over line $i=10$ [27]	108
Figure 5.12	Gas densities over line $i=10$ [27]	109

Figure 5.13 Static pressure over line i=10 [27] . . . . .	109
Figure 5.14 Axial particle velocities over line i=10 [27] . . . . .	110
Figure 5.15 Radial particle velocities over line i=10 [27] . . . . .	110
Figure 5.16 Particle temperatures over line i=10 [27] . . . . .	111
Figure 5.17 Particle densities over line i=10 [27] . . . . .	111
Figure 5.18 Axial gas velocities over line i=98 [27] . . . . .	112
Figure 5.19 Radial gas velocities over line i=98 [27] . . . . .	112
Figure 5.20 Gas temperature over line i=98 [27] . . . . .	113
Figure 5.21 Gas densities over line i=98 [27] . . . . .	113
Figure 5.22 Gas pressure over line i=98 [27] . . . . .	114
Figure 5.23 Particle axial velocities over line i=98 [27] . . . . .	114
Figure 5.24 Particle radial velocities over line i=98 [27] . . . . .	115
Figure 5.25 Particle temperatures over line i=98 [27] . . . . .	115
Figure 5.26 Particle densities over line i=98 [27] . . . . .	116
Figure 5.27 Contours of gas density $kg/m^3$ . . . . .	117
Figure 5.28 Contours of particle density $kg/m^3$ . . . . .	117
Figure 5.29 Contours of Mach number. . . . .	118
Figure 5.30 Contour of pressure $Pa$ . . . . .	118
Figure 5.31 Contours of gas temperature $K$ . . . . .	118
Figure 5.32 Contours of particle temperature $K$ . . . . .	118
Figure 5.33 Contours of gas axial velocity $m/s$ . . . . .	119
Figure 5.34 Contours of particle axial velocity $m/s$ . . . . .	119

Figure 5.35 Contours of gas radial velocity $m/s$ . . . . .	119
Figure 5.36 Contours of particle radial velocity $m/s$ . . . . .	120
Figure 6.1 Cell representation for CHRIC scheme. . . . .	122
Figure 6.2 Reconfiguration of phase topology on a face according to face courant number $c_{fw}$ . . . . .	124
Figure 6.3 Solution of 1D water air shock tube problem at $t = 900\mu s$ . . . . .	133
Figure 6.4 Left: Initial material positions for under water explosion problem. Right: Solution grid near the initial gas bubble surface. . . . .	135
Figure 6.5 Left: Volume fraction solution of underwater explosion problem at $t = 1.2 ms$ . Right: Close-up of the solution. . . . .	135
Figure 6.6 Solutions of pressure distribution (Pa) for underwater explosion problem. White lines show material interfaces. . . . .	136
Figure 6.7 Schematic representation of shock tube problem with liquid-water interface. . . . .	137
Figure 6.8 Color Schlieren like image (magnitude of the density gradient) of the solution at $t = 6 \times 10^{-4} s$ . . . . .	138
Figure 6.9 Liquid volume fraction at time $t = 6 \times 10^{-4} s$ . Right is the close-up view of mixing region. . . . .	138
Figure 6.10 Attenuation and dispersion of 1000 Hz acoustic waves due to dif- ferent sizes of particles suspended in a gas. . . . .	140
Figure 6.11 Volume fraction distribution of particles in a model SPRM. . . . .	141
Figure 6.12 Distribution of temperature and velocity differences between gas and particle phase ( $T_g - T_p$ and $ V_g - V_p $ ). . . . .	142

# CHAPTER 1

## INTRODUCTION

The use of computational methods especially in fluid dynamics applications is expanding throughout industry, academia, defense and research community. The flow fields of interest are becoming more complicated requiring complex three and two dimensional geometric modeling capabilities with high order spatial accuracy. Many applications include flow problems ranging from incompressible, low Mach number flows to supersonic compressible flows at the same time. The field of compressible multi-phase flow is one of the most complex research areas in computational fluid dynamics.

In compressible multi-phase flows, fluids have different physical states and thermodynamical properties and are separated by interfaces. Each phase may have different pressure, velocity and temperature values along with different thermophysical properties such as different equation of states.

### **1.1 Categorization of Compressible Multi-phase Problems**

Compressible multi-phase flows are encountered in many situations in industrial and especially in ballistic applications. Explosions, blast waves propagating in multi-phase media, particles in a rocket motor and some nuclear energy systems are few examples. Although all these examples are categorized as compressible multi-phase flows, they may consist of one or more of the three different multi-phase flow regimes. The first multi-phase system we can distinguish from others is multi-material interfaces separating two or more different compressible materials with different physical

and thermodynamical properties. In an interface problem, there are well defined or resolved interfaces which have an important impact in behavior of the physical system. Blast waves propagating through these interfaces may be encountered in explosion research. The second flow regime which can be categorized in the scope of compressible multi-phase flows is compressible mixtures. In a mixture, there are no well defined interfaces between phases and the effect of the inter-facial topologies are taken into account only for some bulk physical interactions between the compressible phases. Bubbly flow in a pressurized water nuclear reactor channel may be considered as a compressible mixture provided that we can define interactions between water and vapor bubbles in terms of volume fractions and bubble diameters. In many cases, even there may not be any topological information such as diameters of the secondary phases and the only information may be volume fractions. These can be considered as real mixtures. Some schematic representations of multi-phase topologies are shown in Fig. 1.1.

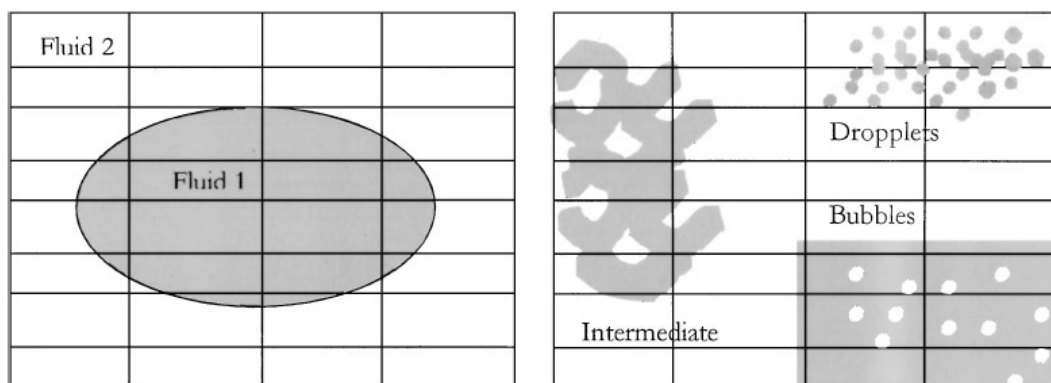


Figure 1.1: Schematic representation of different multi-phase flows. [42].

In computational practice, categorization of multi-phase flows is done according to required grid resolution of interfaces in a problem. For instance, using sufficiently fine solution grid, interfaces of microscopic particles suspended on a gas can be resolved and approached as an interface problem, although this may require some ten billions of grid points for a small region of three dimensional problem. Thus, the method one may approach a multi-phase problem is partly related to computational resources. In practice, microscopic particles in a primary gas or liquid phase can be approached as dilute particles in which phase interactions can be modeled with some

simple momentum drag and heat transfer correlations. These particle models provide sufficient accuracy for practical engineering.

## **1.2 Characteristics of Compressible Multi-phase Flows From Computational Point of View**

The main characteristic of the compressible flows is the occurrence of discontinuities (high and very rapid changes) in flow variables and also in fluid properties. In compressible multi-phase flows there are additional discontinuities which are the interfaces between phases. The occurrence of discontinuities and their interactions may have strong effects on flow characteristics. The continuous pressure waves (acoustic waves) also have complicated physics in a multi-phase flow [47].

Numerical simulation of multi-phase flows are mostly based on the Euler or Navier-Stokes equations augmented by one or several species of conservation equations. The classical one pressure two-fluid models in literature and in currently available commercial CFD codes are in this category. All these classical numerical methods produce artificial diffusion of contact discontinuities resulting in inaccurate pressure and temperature [42]. In addition, these methods show bad convergence characteristics and mostly it is impossible to get a convergent solution for the phases with very different properties. Some models utilize a dilute approximation in which the volume fraction of the primary phase is assumed to be unity, however this approximations leads to degenerate hyperbolic systems [43].

Well posed hyperbolic models for compressible two-phase models include non-conservative products. The occurrence of non-conservative terms is one of the most significant difficulties in these type of models. Non-conservative terms appear in momentum and energy equations, and generally one of the equations is written in non-conservative form.

Since discontinuous solutions are considered in these type of problems, non-conservative formulations lead to numerical and mathematical problems. Numerical solution may be very sensitive to the treatment of non-conservative terms and equations [25, 2].

The compressible multi-phase models with assumption of different pressure and equation of states for each phase have some nice mathematical properties listed below [29, 42];

- They are strictly hyperbolic. This means that equation system defining compressible multi-phase models admits distinct real Eigen values (wave speeds) for each state variable (momentum, density, energy) for each phase in all flow conditions. This property simplifies the development of proper numerical schemes such as Godunov type finite volume methods based on the flux calculations on the control volume faces for conserved variables (mass, momentum, energy).
- They apply to both interface and mixture problems.
- Unique formulation for all types of multi-phase problems allows solving the full set of equations with the same numerical method at each computational cell.
- Energy conservation is ensured at the interfaces with a pressure relaxation procedure. This pressure relaxation procedure must be added to the solution scheme due to the physical fact that each phase has the same pressure on the interface separating the phase materials.
- These models use pure material equation of states for each phase instead of a mixture equation of state which is based on unphysical equilibrium assumptions.

These models have also some drawbacks and difficulties in application;

- System of partial differential equations cannot be written in conservative form.
- It is not easy to derive robust and accurate numerical schemes even in one dimension.
- Solution steps for velocity and pressure relaxations are required.

### 1.3 Related Literature

Common way of treating multi-phase problems has been based on solution of conservation equations for the fractions of each phase's properties; density, momentum, energy and pressure. These fractions are naturally introduced into well known conservation equations through a volume fraction value  $\alpha$  defined for each phase, and the interactions, such as phase conversion, momentum and energy exchanges, between the phases are introduced into the equations through proper right-hand side sources. Additional constraining equations such as sum of the volume fractions being unity, and substantial derivative of a phase volume fraction being zero, accompany the mass, momentum, and energy conservation equations. Of course, the additional terms modeling the multi-phasic effects make numerical solution approach of such an equation system really different than that of conventional single-phase flow problems. The numerical solution of hyperbolic compressible multi-phase models including interfaces requires several ingredients [30, 29]. The numerical procedure involves a non-conservative hyperbolic hydrodynamic solver, an instantaneous velocity relaxation procedure and an instantaneous pressure relaxation procedure. A good example is the work of Saurel and Abgrall [42]. In their work, they proposed a multi-phase Godunov method for compressible multi-phase flows. This method is studied and extended to for more than one dimensions in Chapter 3 in this thesis.

Saurel and Abgrall's [42] multi-phase Godunov method with proper handling of non-conservative terms and application of relaxation procedures was able to solve the seven equation compressible two-phase flow model of [12, 44]. Although the missing data problem associated with missing waves, resulting from the averaging procedure, across the material interfaces was overcome by relaxation procedures, the method is not robust in some conditions especially when high gradients of flow variables such as shocks interact with volume fraction discontinuities (phase interfaces). This issue can be explained by considering the method's approach for handling the information flow across a phase interface. A material interface in this method may only be defined using very small volume fractions for one of the phases. The method passes information across the interface between the same phases first, and then propagates to the other phases by relaxation procedures. In this way the missing waves (missing

information) are recovered. However, because the phase with a very small volume fraction such as  $10^{-6}$  is to get the whole information on an interface first, the method is very prone to numerical difficulties related to the limits of the equation of state used for this phase. This problem becomes more significant especially when high pressure gradients such as shock waves interact with the material interfaces.

Massoni et al. [36] and Allaire et al. [3] proposed five equation models for two-phase compressible mixtures. The advantage of these models were simplicity and less computational requirements compared to seven equation two phase model of [12, 44] which was used in [42]. Murrone et al. [37] proposed a similar five equation model. In contrast to works of Massoni and Allaire [36, 3], they derive the five equation model by an asymptotic analysis of the seven equation model in the limit of zero relaxation times instead of using a priori closures [37]. The main disadvantage of these approaches is similar to that of the seven equation models due to lack of a conservative form. Also, artificial diffusion zones over the phase interfaces become very large with poor spatial resolution used in computations. Murrone et al. tried to overcome this high artificial diffusion by increasing order of the other solution variables using very high order methods in their test cases.

In fact, the problem with the methods mentioned above originates from the employed system of equations. This system is a pure Eulerian multi-phase model describing each phase as a continuum without a material discontinuity such as a phase interface. In principle, the difficulty can be overcome by approaching the problem at a more basic level. Discrete equations can be produced at material interfaces to supply a Godunov method with required numerical fluxes averaged over the cell faces. In fact, Abgrall and Saurel used this approach in a successful and mathematically elegant way [2] to overcome the problems existing in their previous study [42]. With Discrete Equations Method they were also able to solve difficulties associated with the non-conservative products that appear in the seven equations model. In their method, interface topology on the cell interfaces was reconstructed using a stratified equivalence of the real interface (see Fig.1.2 which was used in [2]). Mathematically this reconstruction with addition of the Lagrangian fluxes as source terms eliminates the problematic non-conservative throttling terms. However, in their reconstruction of new interface topology and calculation of Lagrangian fluxes, macro scale flow condi-

tions are not considered. This results in a high artificial mixing of the volume fractions inhibiting tracking of the sharp interfaces. Actually, derivation of such a method even in one dimension is not straightforward and unstructured multi-dimensional counterpart of the method was left unclear in the work of Abgrall and Saurel [2].

In this thesis, methods developed in Chapters 3, 4 and 6 provides more powerful and robust schemes for multi-dimensional applications. All the problems associated with the methods given in cited studies are resolved in this thesis study. In Chapter 3, the method given in [42] is extended to multidimensional problems with more than two phases. Multidimensional and multi-phase versions of the artificial viscosity terms are derived to stabilize the solution of seven equation model used in [42]. Non-conservative terms are discretized with similar methods in the same Chapter. In Chapter 4, a new method based on discrete equations is introduced. This method resolves all the problems associated with the non-conservative equations and terms. In contrast to the method given in [2], the application of the method derived in Chapter 4 to multi-dimensional and multi-phase problems is very straightforward. The high artificial mixing of interfaces associated with the methods given in [3, 36, 2, 37] are fully resolved in Chapter 6. The volume fraction discretization method derived in Chapter 6 provides the highest possible resolution of phase interfaces (in one cell) when used with the interface capturing method derived in Chapter 4. A more detailed outline of the study is given in the next section.

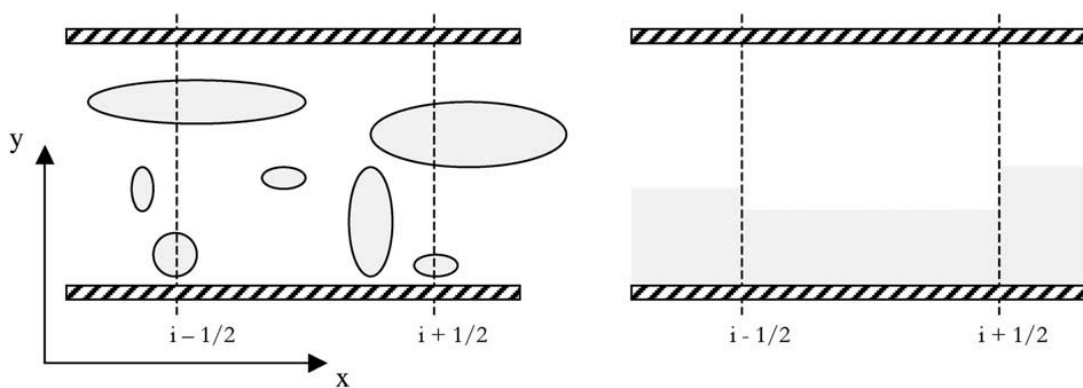


Figure 1.2: Schematic representation of the equivalence between a bubbly flow or a droplet flow with a stratified flow [2].

## 1.4 Methodology and Outline of The Thesis

In Chapter 3, the method proposed by Saurel and Abgrall [42] is extended to multi dimensional unstructured grids and the solution procedure is explained. Two different mathematical and numerical models in addition to a dilute phase solver is developed. Constructing the models is not straightforward even for one dimensional cases studied in the cited papers. Some symbolic calculation packages (mainly Maple [35]) was utilized to develop multidimensional unstructured counterparts of the models. In this study, the steps below are followed for constructing and testing the developed methods.

- The complex numerical methods for compressible multi-phase flows are in fact extensions of methods for compressible single phase flows. Before studying on multi-phase flows, single phase flows should be well defined and tested. In Chapter 2, basic numerical methods are defined which will be used in developing multi-phase methods in later chapters. In Section 2.11 some important numerical boundary condition schemes are explained for general Godunov methods. Finally, these methods explained in first two Sections applicable to single phase flows are tested in Section 2.12.
- In Chapter 3, the first multi-phase method for solution of compressible multi-phase flows is developed. This method is based on the one dimensional scheme given in [42]. In Chapter 3, multi-dimensional counterparts of the formulations are derived and other basic processes such as pressure and velocity relaxations are explained in detail. In Chapter 4, a discrete equations based approach is introduced. This approach is introduced as an alternative to continuous approach given in Chapter 3. These two methods are compared in Section 4.5 using two test problems.
- Since both continuous and discrete approaches developed in Chapters 3 are not applicable to diluted particle phases, a dilute phase approach for particulate flows and suspensions is introduced in Chapter 5. This numerical is validated against some tests cases in Chapter 5.5.
- The discretization method of volume fraction on sharp phase interfaces is cru-

cial for successful implementation of the interface capturing schemes developed in Chapters 3 and 4. Thus a novel high resolution volume fraction discretization method which is applicable to compressible interface, mixture and particulate problems is developed in Chapter 6. This method is validated in Chapter 6.5 for some test cases which are also used in previous chapters.

## 1.5 Basic Numerical And Coding Framework

The goal of this study was to develop methods for the solution of multidimensional compressible multi-phase flows. Due to complexity of the physical problem, special numerical and mathematical models were developed in addition to the methods developed for multi-phase flows. The developed code framework is named as CMPS and used for testing the models developed in this study. CMPS code framework utilizes the following methods;

- Unsplit Godunov finite volume method
- HLLC numerical fluxes (approximate Riemann solvers)
- Combination of Weighted Average Flux (WAF) and MUSCLE reconstruction methods for high order spatial accuracy
- Preconditioning for near incompressible secondary phases and low Mach number flows
- All speed versions of flux solvers for preconditioned equations
- Combination of low-Mach-number preconditioning and artificial compressibility methods for incompressible fluids
- Unstructured, multi domain, multi zone, mixed element, 2-D, 3-D and axisymmetric solver
- Object-oriented methods in C++.



## CHAPTER 2

### NUMERICAL METHODS FOR SINGLE PHASE FLOWS

The complex numerical methods for compressible multi-phase flows are in fact extensions of methods for compressible single phase flows. Before studying on multi-phase flows, single phase flows should be well defined and tested. In this chapter basic numerical methods are defined which will be used in developing multi-phase methods in later chapters.

#### 2.1 Discretization of Euler Equations With Finite Volume Method (FVM)

FVM is a powerful approach which can be used with complex multidimensional unstructured grids. In FVM, the integral equations for governing conservation laws are discretized directly in physical space with reference to a Cartesian coordinate frame. Detailed information about application of FVM on fluid dynamics can be found in the books [23, 9]. For a more brief description of the method, reference [48] is recommended. A general fully discrete explicit scheme using FVM for a general computing cell  $C_0$  (see Fig. 2.1) is written as,

$$U^{n+1} = U^n - \frac{\Delta t}{V} \sum_{s=0}^N A_s T_s^{-1} \hat{F}_s^n \quad (2.1)$$

In Eq. (2.1),  $n$  and  $s$  specifies the time and cell face indexes respectively.  $\Delta t$  is the time step and  $V$  is the volume of the computational cell.  $A_s$  is the area of the cell face  $s$ .  $\hat{F}_s$  is the inter-cell flux at cell face  $s$ .  $\hat{F}_s$  is calculated with an exact or approximate Riemann solver using the left and right state vectors rotated to to local coordinate

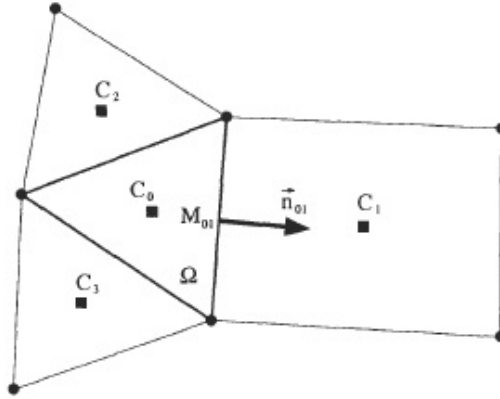


Figure 2.1: Example of two dimensional quadrilateral and triangular computational cells.

frame aligned with the face normal of face  $s$ . This will be explained in the next section.  $T_s$  is the rotation matrix for face  $s$ .  $U$  is the vector of conserved variables given below for two and three dimensions respectively.

$$U = \begin{bmatrix} \rho \\ \rho u \\ \rho v \\ \rho E \end{bmatrix} \quad (2.2)$$

$$U = \begin{bmatrix} \rho \\ \rho u \\ \rho v \\ \rho w \\ \rho E \end{bmatrix} \quad (2.3)$$

here  $\rho$  is density,  $u$  is x-velocity,  $v$  is y-velocity,  $w$  is z-velocity and  $E$  is the total energy per unit volume

$$E = \rho \frac{1}{2} (u^2 + v^2 + w^2) + \rho e \quad (2.4)$$

where  $e$  is the internal energy.

### 2.1.1 Coordinate Rotation

In Eq. 2.1,  $\hat{F}_s$  is calculated using left and right states denoted by the indexes 0 and 1 respectively. 0 always denotes the current computational cell while the index 1 denotes neighboring cell. Figure 2.1 shows this notation. In calculation of  $\hat{F}_s$ , we used Rotational Invariance property of the Euler equations. This property is used to deal with domains that are not aligned with Cartesian coordinate frames. Interested reader can see the reference [48] for a proof of this property of Euler equations. For the assessment of this property in a computational algorithm, one should calculate rotation matrices  $T_s$  for each face. These rotation matrices are used to rotate data vectors  $U_0$  and  $U_1$  in such a way that the new  $\hat{x}$  coordinate is aligned with the face normal. The positive  $\hat{x}$  direction is from left cell  $C_0$  to the right cell  $C_1$  (see Figure 2.1).

The rotation matrices in two and three dimensions are given as

$$T = \begin{bmatrix} 1 & 0 & 0 & 0 \\ 0 & \cos(\theta_s) & \sin(\theta_s) & 0 \\ 0 & -\sin(\theta_s) & \cos(\theta_s) & 0 \\ 0 & 0 & 0 & 1 \end{bmatrix} \quad (2.5)$$

$$T = \begin{bmatrix} 1 & 0 & 0 & 0 & 0 \\ 0 & \cos(\theta_y)\cos(\theta_z) & \cos(\theta_y)\sin(\theta_z) & \sin(\theta_y) & 0 \\ 0 & -\sin(\theta_z) & \cos(\theta_z) & 0 & 0 \\ 0 & -\sin(\theta_y)\cos(\theta_z) & -\sin(\theta_y)\sin(\theta_z) & \cos(\theta_y) & 0 \\ 0 & 0 & 0 & 0 & 1 \end{bmatrix} \quad (2.6)$$

In Eq. 2.5,  $\theta_s$  is the angle between the face normal vector of face  $s$  and the  $x$  coordinate in the counterclockwise direction. The application of three dimensional coordinate rotation is more complicated and interested reader can see some books such as on computer graphics. The methodology used in this study is explained below.

In three dimensions, one need only two rotations not three and the rotation matrix can be written as product two rotation matrices

$$T = T_y T_z \quad (2.7)$$

with

$$T_y = \begin{bmatrix} 1 & 0 & 0 & 0 & 0 \\ 0 & \cos(\theta_y) & 0 & \sin(\theta_y) & 0 \\ 0 & 0 & 1 & 0 & 0 \\ 0 & -\sin(\theta_y) & 0 & \cos(\theta_y) & 0 \\ 0 & 0 & 0 & 0 & 1 \end{bmatrix} \quad (2.8)$$

and

$$T_z = \begin{bmatrix} 1 & 0 & 0 & 0 & 0 \\ 0 & \cos(\theta_z) & \sin(\theta_z) & 0 & 0 \\ 0 & -\sin(\theta_z) & \cos(\theta_z) & 0 & 0 \\ 0 & 0 & 0 & 1 & 0 \\ 0 & 0 & 0 & 0 & 1 \end{bmatrix} \quad (2.9)$$

where  $\theta_y$  and  $\theta_z$  are angles of rotation about  $y$  and  $z$  coordinates. Rotations are done in counter clockwise. Below simple and efficient methods are given for calculation of rotation matrices using face normal vectors  $\vec{n}$ .

In two dimensions

$$\cos(\theta) = \frac{n_1}{|\vec{n}|}, \quad \sin(\theta) = \frac{n_2}{|\vec{n}|} \quad (2.10)$$

Then the two dimensional rotation matrix becomes,

$$T = \begin{bmatrix} 1 & 0 & 0 & 0 \\ 0 & n_1 & n_2 & 0 \\ 0 & -n_2 & n_1 & 0 \\ 0 & 0 & 0 & 1 \end{bmatrix} \quad (2.11)$$

For three dimensional cases the trigonometric functions in rotation matrices can be defined in terms of the face normal vectors in two steps. First the elements of the  $T_z$  are calculated as,

$$\cos(\theta_z) = \frac{n_1}{\sqrt{n_1^2 + n_2^2}} \quad \sin(\theta_z) = \frac{n_2}{\sqrt{n_1^2 + n_2^2}} \quad (2.12)$$

Then the elements of the rotation matrix  $T_y$  is calculated using the face normal vector in the new coordinate system rotated about the  $z$  - axis,

$$\cos(\theta_y) = \frac{n_3}{\sqrt{n_1^2 + n_2^2 + n_3^2}} \quad \sin(\theta_y) = \frac{\sqrt{n_1^2 + n_2^2}}{\sqrt{n_1^2 + n_2^2 + n_3^2}} \quad (2.13)$$

The inter-cell flux  $\hat{F}_s$  is calculated using rotated data vectors  $\hat{U}_0 = T_s U_0$  and  $\hat{U}_1 = T_s U_1$ . After calculating inter-cell fluxes on each face, calculated fluxes should be rotated back to original Cartesian frame using the inverses of the rotation matrices given below.

For two dimensions

$$T^{-1} = \begin{bmatrix} 1 & 0 & 0 & 0 \\ 0 & n_1 & -n_2 & 0 \\ 0 & n_2 & n_1 & 0 \\ 0 & 0 & 0 & 1 \end{bmatrix} \quad (2.14)$$

For three dimensions

$$T^{-1} = (T_y T_z)^{-1} = T_z^{-1} T_y^{-1} \quad (2.15)$$

with

$$T_y^{-1} = \begin{bmatrix} 1 & 0 & 0 & 0 & 0 \\ 0 & \cos(\theta_y) & 0 & -\sin(\theta_y) & 0 \\ 0 & 0 & 1 & 0 & 0 \\ 0 & \sin(\theta_y) & 0 & \cos(\theta_y) & 0 \\ 0 & 0 & 0 & 0 & 1 \end{bmatrix} \quad (2.16)$$

and

$$T_z^{-1} = \begin{bmatrix} 1 & 0 & 0 & 0 & 0 \\ 0 & \cos(\theta_z) & -\sin(\theta_z) & 0 & 0 \\ 0 & \sin(\theta_z) & \cos(\theta_z) & 0 & 0 \\ 0 & 0 & 0 & 1 & 0 \\ 0 & 0 & 0 & 0 & 1 \end{bmatrix} \quad (2.17)$$

## 2.2 The Split Multi-Dimensional Riemann Problem

In a Godunov type Finite Volume Method as in Section 2.1, one requires the solution of split Riemann problems at cell faces. The  $\hat{x}$  – *split* Riemann problem for the Euler equations can be written as the initial value problem given below,

$$\frac{\partial \hat{U}}{\partial t} + \frac{\partial F(\hat{U})}{\partial \hat{x}} = 0$$

$$\hat{U}(\hat{x}, 0) = \begin{cases} \hat{U}_L & \text{if } \hat{x} < 0, \\ \hat{U}_R & \text{if } \hat{x} > 0, \end{cases} \quad (2.18)$$

where

$$\hat{U} = \begin{bmatrix} \rho \\ \rho \hat{u} \\ \rho \hat{v} \\ \rho \hat{w} \\ \rho E \end{bmatrix}, \quad \hat{F} = \begin{bmatrix} \rho \hat{u} \\ \rho \hat{u}^2 + P \\ \rho \hat{u} \hat{v} \\ \rho \hat{u} \hat{w} \\ \hat{u}(\rho E + P) \end{bmatrix} \quad (2.19)$$

The structure of the similarity solution for initial value problem 2.18 is shown in Fig. 2.2. The solution of Riemann problem for split three dimensional Euler equations is fundamentally the same as the solution for corresponding one-dimensional problem. There are two additional characteristic fields associated with the two eigen values having the values  $\hat{u}$ . These are two shear waves across which the tangential velocity components  $\hat{v}$  and  $\hat{w}$  change discontinuously. The region between the right and left waves is usually denoted as the Star Region. Both pressure  $P$  and the normal velocity  $\hat{u}$  are constant across the middle wave in the Star Region.

In sections 2.3 and 2.4, some approximate solution methods of split Riemann problem are given for calculation of inter-cell fluxes.

### 2.3 Explicit Scheme with Rusanov and Lax-Friedrich Fluxes

The numerical flux  $\hat{F}_s$  can be approximated by Rusanov flux [41] as

$$\hat{F}_s = \frac{1}{2} \left[ \hat{F}_{s,0} + \hat{F}_{s,1} - \hat{S} (\hat{U}_{s,1} - \hat{U}_{s,0}) \right] \quad (2.20)$$

where the index  $s, 0$  refers to the current computational cell side of face  $s$ , and the

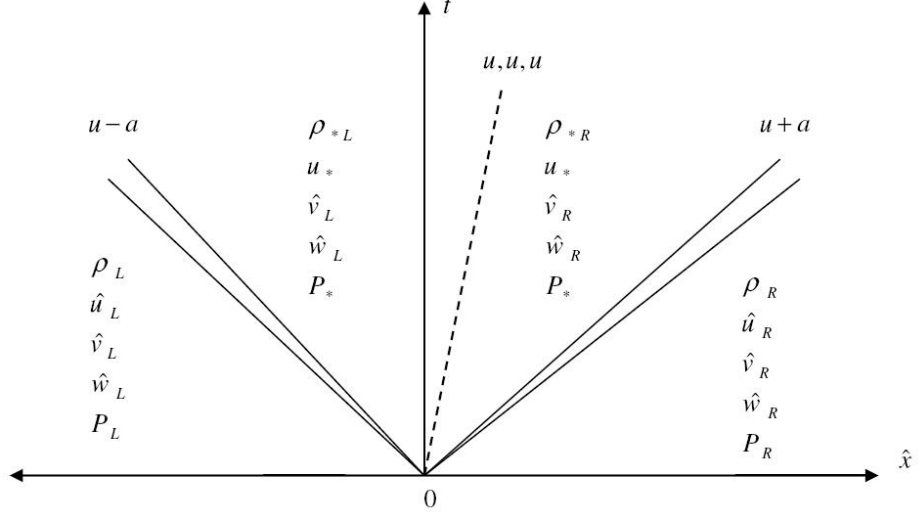


Figure 2.2: Structure of the solution of the three-dimensional  $\hat{x}$  split Riemann problem.

index  $s$ , 1 refers to the neighboring cell side of face  $s$ .  $\hat{U}$  is the rotated state vector of conserved variables calculated as  $\hat{U} = TU$ ,

$$\hat{U} = \underbrace{\begin{bmatrix} \rho \\ \rho \hat{u} \\ \rho \hat{v} \\ \rho E \end{bmatrix}}_{In\ 2D} \qquad \hat{U} = \underbrace{\begin{bmatrix} \rho \\ \rho \hat{u} \\ \rho \hat{v} \\ \rho \hat{w} \\ \rho E \end{bmatrix}}_{In\ 3D} \quad (2.21)$$

with  $\hat{u} = un_1 + vn_2$  and  $\hat{v} = -un_2 + vn_1$  in two dimensions. For three dimensional calculations

$$\begin{aligned} \hat{u} &= \cos(\theta_y) \cos(\theta_z) u + \cos(\theta_y) \sin(\theta_z) v + \sin(\theta_y) w \\ \hat{v} &= -\sin(\theta_z) u + \cos(\theta_z) v \\ \hat{w} &= -\sin(\theta_y) \cos(\theta_z) u - \sin(\theta_y) \sin(\theta_z) v + \cos(\theta_y) w \end{aligned} \quad (2.22)$$

with

$$\cos(\theta_z) = \frac{n_1}{\sqrt{n_1^2 + n_2^2}} \quad \sin(\theta_z) = \frac{n_2}{\sqrt{n_1^2 + n_2^2}} \quad (2.23)$$

$$\cos(\theta_y) = \frac{n_3}{\sqrt{n_1^2 + n_2^2 + n_3^2}} \quad \sin(\theta_y) = \frac{\sqrt{n_1^2 + n_2^2}}{\sqrt{n_1^2 + n_2^2 + n_3^2}} \quad (2.24)$$

While  $\hat{u}$  is the real rotated value of the  $u$  velocity,  $\hat{v}$  and  $\hat{w}$  are not, since we only need to solve split three-dimensional Riemann problem in the direction of rotated  $\hat{x}$  coordinate. The flux vector  $\hat{F}$  is written as below in split form

$$\hat{F} = \underbrace{\begin{bmatrix} \rho\hat{u} \\ \rho\hat{u}^2 + P \\ \rho\hat{u}\hat{v} \\ \hat{u}(\rho E + P) \end{bmatrix}}_{\text{In } 2D}, \quad \hat{F} = \underbrace{\begin{bmatrix} \rho\hat{u} \\ \rho\hat{u}^2 + P \\ \rho\hat{u}\hat{v} \\ \rho\hat{u}\hat{w} \\ \hat{u}(\rho E + P) \end{bmatrix}}_{\text{In } 3D} \quad (2.25)$$

The wave speed  $\hat{S}$  in Eq. (2.20) can be calculated according to Davis [11]

$$\hat{S} = \max\{|\hat{u}_L - a_L|, |\hat{u}_R - a_R|, |\hat{u}_L + a_L|, |\hat{u}_R + a_R|\} \quad (2.26)$$

where  $a$  is the speed of sound. Another possibility for the speed  $\hat{S}$  is the maximum wave speed  $\hat{S}_{max}$  found by imposing the stability condition Eq. (2.55) with  $C_{cfl} = 1$ ,

$$\hat{S}_{max} = \frac{V_i}{(\hat{A}_x + \hat{A}_y + \hat{A}_z) \Delta t} \quad (2.27)$$

Using the wave speed  $\hat{S}_{max}$ , the Lax-Friedrichs numerical flux is obtained

$$\hat{F}_s = \frac{1}{2} \left[ \hat{F}_{s,0} + \hat{F}_{s,1} - \frac{V_i}{(\hat{A}_x + \hat{A}_y + \hat{A}_z) \Delta t} (\hat{U}_{s,1} - \hat{U}_{s,0}) \right] \quad (2.28)$$

## 2.4 HLL and HLLC Approximate Riemann Solvers for Approximate Godunov Methods

For the purpose of computing a Godunov flux, Harten, Lax and Leer [20] presented a method for solving the Riemann problem. The resulting Riemann solvers are known

as HLL Riemann solvers. The main idea in these solvers is the assumption of a wave configuration which consists of two waves instead of three. The resulting HLL Riemann solvers form the bases of very efficient and robust approximate Godunov type methods [48]. The inter-cell flux at a face  $s$  for the approximate Godunov method based on HLL Riemann solvers is given by

$$\hat{F}_s^{hll} = \begin{cases} \hat{F}_{s,0} & \text{if } 0 \leq \hat{S}_{s,0} \\ \frac{\hat{S}_{s,1}\hat{F}_{s,0} - \hat{S}_{s,0}\hat{F}_{s,1} + \hat{S}_{s,0}\hat{S}_{s,1}(\hat{U}_{s,1} - \hat{U}_{s,0})}{\hat{S}_{s,1} - \hat{S}_{s,0}} & \text{if } \hat{S}_{s,0} \leq 0 \leq \hat{S}_{s,1} \\ \hat{F}_{s,1} & \text{if } 0 \geq \hat{S}_{s,1} \end{cases} \quad (2.29)$$

One shortcoming of these schemes is the assumption of two-wave configuration. As a consequence of this assumption, the resolution of physical features such as contact discontinuity, shear waves and material interfaces can be very inaccurate. In view of these shortcomings Toro, Spruce and Speares [49] put forward a modification called the HLLC Riemann solver where C stands for contact. In this scheme the missing middle waves are put back into the structure of the approximate Riemann solver. The HLLC flux for the approximate Godunov method is given by

$$F_s^{hllc} = \begin{cases} \hat{F}_{s,0} & \text{if } 0 \leq \hat{S}_{s,0} \\ F_{s,0}^* = \hat{F}_{s,0} + \hat{S}_{s,0}(U_{s,0}^* - \hat{U}_{s,1}) & \text{if } \hat{S}_{s,0} \leq 0 \leq \hat{S}_s^* \\ F_{s,1}^* = \hat{F}_{s,1} + \hat{S}_{s,1}(U_{s,1}^* - \hat{U}_{s,1}) & \text{if } \hat{S}_s^* \leq 0 \leq \hat{S}_{s,1} \\ \hat{F}_{s,1} & \text{if } 0 \geq \hat{S}_{s,1} \end{cases} \quad (2.30)$$

where  $U_{s,K}^*$  for  $K = 0$  and  $K = 1$  is calculated as below

$$U_{s,K}^* = \rho_K \left( \frac{\hat{S}_{s,K} - \hat{u}_{s,K}}{\hat{S}_{s,K} - \hat{S}_s^*} \right) \begin{bmatrix} 1 \\ \hat{S}_s^* \\ v_K \\ w_K \\ \frac{E_K}{\rho_K} + (\hat{S}_s^* - u_K) \left[ \hat{S}_s^* + \frac{P_K}{\rho(S_{s,K} - u_K)} \right] \end{bmatrix} \quad (2.31)$$

The middle wave speed  $\hat{S}_s^*$  can be calculated by the expression [6]

$$\hat{S}_s^* = \frac{P_{s,1} - P_{s,0} + \rho_{s,0}\hat{u}_{s,0}(\hat{S}_{s,1} - \hat{u}_{s,0}) - \rho_{s,1}\hat{u}_{s,1}(\hat{S}_{s,1} - \hat{u}_{s,1})}{\rho_{s,0}(\hat{S}_{s,0} - \hat{u}_{s,0}) - \rho_{s,1}(\hat{S}_{s,1} - \hat{u}_{s,1})} \quad (2.32)$$

The left and right wave speeds  $\hat{S}_{s,0}$  and  $\hat{S}_{s,1}$  can be calculated by simple direct estimates below suggested by Davis [11]

$$\begin{aligned} \hat{S}_{s,0} &= \min(\hat{u}_{s,0} - a_{s,0}, \hat{u}_{s,1} - a_{s,1}) \\ \hat{S}_{s,1} &= \max(\hat{u}_{s,0} + a_{s,0}, \hat{u}_{s,1} + a_{s,1}) \end{aligned} \quad (2.33)$$

Another method based on Roe eigenvalues [40] for wave speed estimation is proposed by Einfeldt [15]. These estimations are reported to lead effective and robust schemes [48].

$$\hat{S}_{s,0} = \tilde{u} - \tilde{d}, \quad \hat{S}_{s,1} = \tilde{u} + \tilde{d} \quad (2.34)$$

$$\tilde{d}^2 = \frac{\sqrt{\rho_{s,0}}a_{s,0}^2 + \sqrt{\rho_{s,1}}a_{s,1}^2}{\sqrt{\rho_{s,0}} + \sqrt{\rho_{s,1}}} + \frac{1}{2} \frac{\sqrt{\rho_{s,0}} \sqrt{\rho_{s,1}}}{(\sqrt{\rho_{s,0}} + \sqrt{\rho_{s,1}})^2} \quad (2.35)$$

Where  $\tilde{u}$  is the Roe averaged speed of fluid normal to the cell face.

$$\tilde{u} = \frac{\sqrt{\rho_{s,0}}\hat{u}_{s,0} + \sqrt{\rho_{s,1}}\hat{u}_{s,1}}{\sqrt{\rho_{s,0}} + \sqrt{\rho_{s,1}}} \quad (2.36)$$

## 2.5 Axisymmetric Flows

In axisymmetry, the domain is symmetric about a coordinate axis. This symmetry axis in axial direction is chosen as the  $x$  - axis. The second coordinate is the radial direction which is measured from the axis of symmetry  $x$ . The Euler equations in axisymmetric coordinates are written as

$$\frac{\partial U}{\partial t} + \frac{\partial F(U)}{\partial x} + \frac{\partial G(U)}{\partial r} = S(U) \quad (2.37)$$

where

$$\begin{aligned}
 U &= \begin{bmatrix} \rho \\ \rho u \\ \rho v \\ \rho E \end{bmatrix}, & F &= \begin{bmatrix} \rho u \\ \rho u^2 + P \\ \rho uv \\ u(\rho E + P) \end{bmatrix} \\
 G &= \begin{bmatrix} \rho v \\ \rho uv \\ \rho v^2 + P \\ v(\rho E + P) \end{bmatrix}, & S &= -\frac{1}{r} \begin{bmatrix} \rho v \\ \rho uv \\ \rho v^2 \\ v(\rho E + P) \end{bmatrix}
 \end{aligned} \tag{2.38}$$

In axisymmetric coordinate system, finite volumes are represented by 3D axisymmetric rings created by rotation of the 2D surfaces around the x-axis. Analogously, cell faces are created by rotation of 2D edges around the x-axis. Cell volumes and face areas are calculated by multiplying their areas or lengths by radial coordinate of their centroids.

$$\begin{aligned}
 V_{ax} &= 2\pi r_c A \\
 A_{ax} &= 2\pi r_c L
 \end{aligned} \tag{2.39}$$

If geometric quantities are calculated as in Eq. 2.39, the source terms in Eq. 2.38 are not calculated and the solution procedure is the same as in 2D case. In this case a source term defined in Eq. 2.40 should be added to the radial momentum equation which is the net effect of of the balancing force in the radial direction due to normal stresses in the azimuthal direction [57, 51]. This method has its attractions from a numerical point of view [48].

$$S = \begin{bmatrix} 0 \\ 0 \\ \frac{2\pi P A}{V_{ax}} \\ 0 \end{bmatrix} = \frac{1}{y} \begin{bmatrix} 0 \\ 0 \\ P \\ 0 \end{bmatrix} \tag{2.40}$$

## 2.6 Explicit Time Stepping

An explicit scheme starts from a known solution  $U^n$  at time  $t$  and employs the Eq. 2.1 to obtain a new solution  $U^{n+1}$  at time  $(t+\Delta t)$ . The new solution  $U^{n+1}$  depends solely on the values already known. The most popular and wide spread explicit methods are the Runge-Kutta multi stage time-stepping schemes. The multistage scheme advances the solution in a number of steps called stages. Applied to fully discrete explicit scheme of Eq. 2.1, a four stages Runge-Kutta scheme is written as

$$\begin{aligned}
 U^{(0)} &= U^n \\
 U^{(1)} &= U^{(0)} - \alpha_1 \frac{\Delta t}{V} \sum_{s=0}^N A_s T_s^{-1} \hat{F}_s^{(0)} \\
 U^{(2)} &= U^{(0)} - \alpha_2 \frac{\Delta t}{V} \sum_{s=0}^N A_s T_s^{-1} \hat{F}_s^{(1)} \\
 U^{(3)} &= U^{(0)} - \alpha_3 \frac{\Delta t}{V} \sum_{s=0}^N A_s T_s^{-1} \hat{F}_s^{(2)} \\
 U^{n+1} &= U^{(0)} - \alpha_4 \frac{\Delta t}{V} \sum_{s=0}^N A_s T_s^{-1} \hat{F}_s^{(3)}
 \end{aligned} \tag{2.41}$$

where  $\alpha$  are the stage coefficients. The stage coefficients can be tuned to increase maximum time step and to improve the stability for a spatial discretization. For a first order upwind spatial discretization the values below are recommended for stage coefficients [31], which increase the  $CFL$  number to 2.

$$\alpha_1 = 0.0833 \quad \alpha_2 = 0.2069 \quad \alpha_3 = 0.4265 \quad \alpha_4 = 1.000 \tag{2.42}$$

For second order spatial discretization following values for stage coefficients are recommended [31],

$$\alpha_1 = 0.1084 \quad \alpha_2 = 0.2602 \quad \alpha_3 = 0.5052 \quad \alpha_4 = 1.000 \tag{2.43}$$

## 2.7 Preconditioning For Low-Mach Number Flows

The density based methods provide good stability and convergence characteristics when solving compressible flows at transonic and supersonic speeds. However, in

general, these methods are not suitable for efficiently solving low Mach number or incompressible flows due to large ratio of acoustic and convective timescales at the low-speed flow regimes. To alleviate this stiffness problem a time-derivative preconditioning of the flow equations is applied.

The preconditioning matrix applied to time derivative of the Euler equations is given below [55],

$$\Gamma = \begin{bmatrix} \Theta & 0 & 0 & 0 & \rho_T \\ \Theta u & \rho & 0 & 0 & \rho_T u \\ \Theta v & 0 & \rho & 0 & \rho_T v \\ \Theta w & 0 & 0 & \rho & \rho_T w \\ \Theta H - 1 & \rho u & \rho v & \rho w & \rho_T H + \rho C_p \end{bmatrix} \quad (2.44)$$

The total enthalpy  $H$  is related to total energy  $E$  by  $E = H - p/\rho$ , where  $H = h + |u|^2 / 2$  and  $h = C_p T$ . And  $\rho_T$  is defined as

$$\rho_T = \left. \frac{\partial \rho}{\partial T} \right|_p \quad (2.45)$$

The term  $\Theta$  is defined as,

$$\Theta = \left( \frac{1}{U_r^2} - \frac{\rho_T}{\rho C_p} \right) \quad (2.46)$$

Here  $U_r$  is the reference velocity defined as follows for an ideal gas,

$$U_r = \begin{cases} \epsilon c & \text{if } |u| \leq \epsilon c \\ |u| & \text{if } \epsilon c \leq |u| \leq c \\ c & \text{if } |u| \geq c \end{cases} \quad (2.47)$$

In the preceding expressions,  $\epsilon$  is a small number ( $\approx 10^{-5}$ ) included to prevent singularities at stagnation points. The preconditioned system in conservation form is obtained as,

$$\Gamma = \frac{\partial}{\partial t} \int \int \int Q dV + \int \int F \cdot d\vec{A} = 0 \quad (2.48)$$

$Q$  is the vector of primitive variables where  $Q = [P, u, v, w, T]^T$ . The resultant eigenvalues of the preconditioned system are given by

$$\lambda \left( \Gamma^{-1} \frac{\partial F}{\partial Q} \right) = u, u, u, \hat{u} + \acute{a}, \hat{u} - \acute{a} \quad (2.49)$$

where

$$u = u \cdot \vec{n} = \hat{u} \quad (2.50)$$

$$\hat{u} = u(1 - \alpha) \quad (2.51)$$

$$\acute{a} = \sqrt{\alpha^2 u^2 + U_r^2} \quad (2.52)$$

$$\alpha = (1 - \beta U_r^2) / 2 \quad (2.53)$$

$$\beta = \left( \rho_p + \frac{\rho_T}{\rho C_p} \right) \quad (2.54)$$

## 2.8 Calculation of Time Steps

In Eq. 2.1,  $\Delta t$  is calculated for each cell according to stability condition [54] as,

$$\Delta t_i = \frac{C_{cfl} V_i}{(\Lambda_x + \Lambda_y + \Lambda_z)_i} \quad (2.55)$$

where  $C_{cfl}$  and  $V_i$  are the CFL number and the volume of the cell  $i$  respectively.  $\Lambda$  are the convective spectral radii calculated as,

$$\Lambda_x = (|u| + a) \hat{A}_x, \quad \Lambda_y = (|v| + a) \hat{A}_y, \quad \Lambda_z = (|w| + a) \hat{A}_z \quad (2.56)$$

where  $a$  is the speed of sound. The variables  $\hat{A}_x$ ,  $\hat{A}_y$  and  $\hat{A}_z$  represent projections of the control volume on the  $y - z$ ,  $x - z$  and  $x - y$  plane respectively. They are given by the following formulas,

$$\hat{A}_x = \frac{1}{2} \sum_{s=0}^{N_F-1} |\vec{A}_x|_s, \quad \hat{A}_y = \frac{1}{2} \sum_{s=0}^{N_F-1} |\vec{A}_y|_s, \quad \hat{A}_z = \frac{1}{2} \sum_{s=0}^{N_F-1} |\vec{A}_z|_s \quad (2.57)$$

where  $\vec{A}_x, \vec{A}_y, \vec{A}_z$  are the  $x, y$  and  $z$  components of the face normal vector  $\vec{A}_s$ .

## 2.9 Weighted Average Flux (WAF) Methods For High-Order Accuracy

In the WAF method the inter-cell flux is an integral average of the physical flux across the full structure of the solution of a local Riemann problem [48]. The structured multidimensional versions of this method can be found in reference [7]. Here multi-dimensional unstructured versions of the WAF fluxes are developed. The WAF flux is given by

$$\hat{F}_s = \frac{1}{\hat{x}_R - \hat{x}_L} \int_{\hat{x}_L}^{\hat{x}_R} \hat{F}(\hat{U}_s(\hat{x}, \frac{\Delta t}{2})) d\hat{x} \quad (2.58)$$

where  $\hat{x}_L$  and  $\hat{x}_R$  are the positions of cell centers on the  $\hat{x}$  coordinate in the rotated coordinate system. So the integral is evaluated on the  $\hat{x}$  coordinate line which is perpendicular to the cell surface  $s$ .  $\hat{U}_s$  is the solution of the  $\hat{x}$  split multi-dimensional Riemann problem. The solution of the split Riemann problem across the surface  $s$  consists of four constant states  $\hat{U}^1, \hat{U}^2, \hat{U}^3$  and  $\hat{U}^4$  separated by the lines corresponding to the three wave speeds  $\hat{S}_1, \hat{S}_2$  and  $\hat{S}_3$  (see section 2.2). The left wave  $\hat{S}_1$  and the right wave  $\hat{S}_3$  may be shock or rarefaction waves. Using these constant states the integral 2.58 is calculated as (see Figure 2.3)

$$\hat{F}_s = \sum_{k=1}^{N+1} \beta_k \hat{F}(U^{(k)}) \quad (2.59)$$

### 2.9.1 WAF Version of HLL Riemann Solver

There are two waves  $S_1$  and  $S_2$  in a HLL based solution of Riemann problem. In formula 2.59,  $\beta_k$  values for three constant states are calculated as

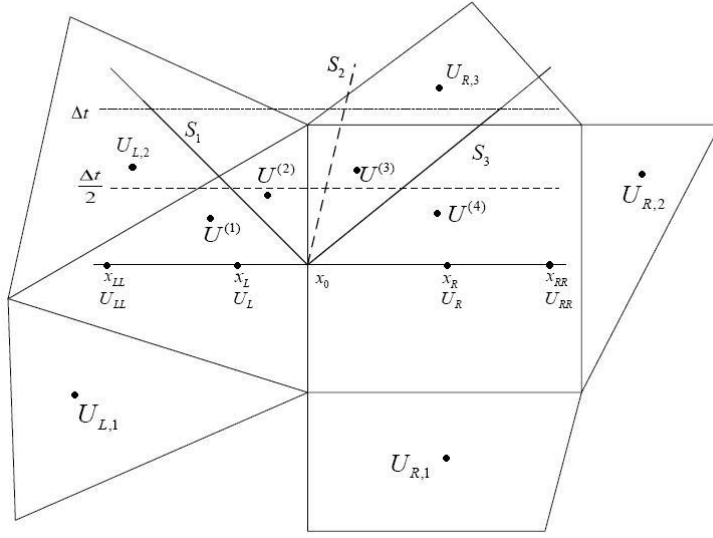


Figure 2.3: The solution of the Riemann problem and the domain of the integral.

$$\begin{aligned}
 \beta_1 &= \frac{2\hat{x}_0 - 2\hat{x}_L + \hat{S}_1 \Delta t}{2(\hat{x}_R - \hat{x}_L)} \\
 \beta_2 &= \frac{\Delta t (\hat{S}_2 - \hat{S}_1)}{2(\hat{x}_R - \hat{x}_L)} \\
 \beta_3 &= \frac{2\hat{x}_R - 2\hat{x}_0 - \hat{S}_2 \Delta t}{2(\hat{x}_R - \hat{x}_L)}
 \end{aligned} \tag{2.60}$$

Using equations 2.60, WAF version of HLL inter-cell flux is written as

$$\begin{aligned}
 \hat{F}_s &= \frac{1}{\Delta \hat{x}} \left[ (\hat{x}_0 - \hat{x}_L) \hat{F}_1 + (\hat{x}_R - \hat{x}_0) \hat{F}_3 \right] \\
 &\quad - \frac{1}{2} \left[ \frac{\Delta t \hat{S}_1}{\Delta \hat{x}} (\hat{F}_2 - \hat{F}_1) + \frac{\Delta t \hat{S}_2}{\Delta \hat{x}} (\hat{F}_3 - \hat{F}_2) \right]
 \end{aligned} \tag{2.61}$$

The TVD version of the equation 2.61 can be written as

$$\begin{aligned}
 \hat{F}_s &= \frac{1}{\Delta \hat{x}} \left[ (\hat{x}_0 - \hat{x}_L) \hat{F}_1 + (\hat{x}_R - \hat{x}_0) \hat{F}_3 \right] \\
 &\quad - \frac{1}{2} \left[ \text{sign}(c_1) \phi_s^{(1)} (\hat{F}_2 - \hat{F}_1) + \text{sign}(c_2) \phi_s^{(2)} (\hat{F}_3 - \hat{F}_2) \right]
 \end{aligned} \tag{2.62}$$

where  $c_k$  is the Courant number for wave  $k$  with speed  $S_k$  and defined as

$$c_k = \frac{\Delta t \hat{S}_k}{\Delta x} \quad (2.63)$$

$\hat{F}_1$  and  $\hat{F}_3$  are flux vectors  $F(\hat{U}_L)$  and  $F(\hat{U}_R)$ . Flux vector  $\hat{F}_2$  is calculated using HLL Riemann solver

$$\hat{F}_2 = \frac{\hat{S}_2 \hat{F}_L - \hat{S}_1 \hat{F}_R + \hat{S}_1 \hat{S}_2 (\hat{U}_R - \hat{U}_L)}{\hat{S}_2 - \hat{S}_1} \quad (2.64)$$

WAF limiter functions  $\phi_s^{(k)}$  in equation 2.62 can be calculated by four different approaches written below [48]

$$\phi_{mb}(r_k, |c_k|) = \begin{cases} 1 & \text{if } r_k \leq 0, \\ 1 - (1 - |c_k|) r_k & \text{if } 0 \leq r_k \leq 1, \\ |c_k| & \text{if } r_k \geq 1. \end{cases} \quad (2.65)$$

$$\phi_{va}(r_k, |c_k|) = \begin{cases} 1 & \text{if } r_k \leq 0, \\ 1 - \frac{(1-|c_k|)(1+r_k)r_k}{1+r_k^2} & \text{if } 0 \leq r^{(k)} \leq 1. \end{cases} \quad (2.66)$$

$$\phi_{vl}(r_k, |c_k|) = \begin{cases} 1 & \text{if } r_k \leq 0, \\ 1 - \frac{(1-|c_k|)2r_k}{1+r_k} & \text{if } 0 \leq r_k \leq 1. \end{cases} \quad (2.67)$$

$$\phi_{sb}(r_k, |c_k|) = \begin{cases} 1 & \text{if } r_k \leq 0, \\ 1 - 2(1 - |c_k|) r_k & \text{if } 0 \leq r_k \leq \frac{1}{2}, \\ |c_k| & \text{if } \frac{1}{2} \leq r_k \leq 1, \\ 1 - (1 - |c_k|) r_k & \text{if } 1 \leq r_k \leq 2, \\ 2|c_k| - 1 & \text{if } r \geq 2. \end{cases} \quad (2.68)$$

The WAF limiter functions are related and equivalent to conventional flux limiters.  $\phi_{mb}$  is related to MINBEE,  $\phi_{va}$  is related to van Albada's limiter,  $\phi_{vl}$  is related to van Leer's limiter and  $\phi_{sb}$  is related to SUPERBEE. The flow parameter  $r_k$  in limiter functions refers to wave  $k$  in the solution of the Riemann problem is defined as the ratio,

$$r_k = \begin{cases} \frac{\Delta q_{LL}^{(k)}}{\Delta q^{(k)}} & \text{if } c_k > 0, \\ \frac{\Delta q_{RR}^{(k)}}{\Delta q^{(k)}} & \text{if } c_k < 0. \end{cases} \quad (2.69)$$

where  $\Delta q_{LL}^{(k)}$  is the jump in  $q$  across the wave  $k$  in the solution of Riemann problem for states  $U_{LL}$  and  $U_L$ ,  $\Delta q_{RR}^{(k)}$  is the jump in  $q$  across the wave  $k$  in the solution of Riemann problem for states  $U_R$  and  $U_{RR}$  and  $\Delta q^{(k)}$  is the jump across the wave  $k$  in solution of Riemann problem for states  $U_L$  and  $U_R$  (see Figure 2.3). For the Euler equations the choice  $q \equiv \rho$  (density) gives satisfactory results. <sup>1</sup>Density values  $\rho_{LL}^{(k)}$  and  $\rho_{RR}^{(k)}$  are needed for calculating the jumps  $\Delta\rho_{LL}^{(k)}$  and  $\Delta\rho_{RR}^{(k)}$ . These values are calculated by a weighted averaging process described below.

$$\rho_{LL}^{(1)} = \frac{\sum_{s=1}^{N-1} (\rho_s)_L (\vec{A}_s)_L \cdot \vec{A}}{\sum_{s=1}^{N-1} (\vec{A}_s)_L \cdot \vec{A}} \quad (2.70)$$

where  $N$  is the number of neighboring cells of left cell. The index  $s$  refers to the neighboring cells, and  $\vec{A}_s$  are the face normal vectors directed into the left cell.  $\vec{A}$  is the face normal vector directed to the the right cell.  $\rho_{LL}^{(3)}$  is calculated using HLL solver,

$$\rho_{LL}^{(2)} = \frac{\hat{S}_{LL}^{(2)}\rho_L - \hat{S}_{LL}^{(1)}\rho_{LL}^{(1)} + \hat{u}_{LL}^{(1)}\rho_{LL}^{(1)} - \hat{u}_L\rho_L}{\hat{S}_{LL}^{(2)} - \hat{S}_{LL}^{(1)}} \quad (2.71)$$

Equation 2.71 is written assuming  $\rho_{LL}^{(3)} = \rho_L$  and  $u_{LL}^{(3)} = u_L$ . The unknown values  $u_{LL}^{(1)}$ ,  $S_{LL}^{(2)}$  and  $S_{LL}^{(1)}$  in equation 2.71 are calculated by a method similar to the one in equation 2.70. The jump  $\Delta\rho_{RR}^{(1)} \equiv \rho_{LL}^{(2)} - \rho_{LL}^{(1)}$  across wave  $S_{LL}^{(1)}$  is found

$$\Delta\rho_{LL}^{(1)} = \frac{\hat{S}_{LL}^{(2)}(\rho_L - \rho_{LL}^{(1)}) + \hat{u}_{LL}^{(1)}\rho_{LL}^{(1)} - \hat{u}_L\rho_L}{\hat{S}_{LL}^{(2)} - \hat{S}_{LL}^{(1)}} \quad (2.72)$$

Similarly, the jump  $\Delta\rho_{LL}^{(2)} \equiv \rho_L - \rho_{LL}^{(2)}$  is found as

---

<sup>1</sup> The index  $k$  over scalars (not jumps or waves) refers to the constant state zones in solution of Riemann problem.

$$\Delta\rho_{LL}^{(2)} = \frac{\hat{S}_{LL}^{(1)}(\rho_{LL}^{(1)} - \rho_L) - \hat{u}_{LL}^{(1)}\rho_{LL}^{(1)} + \hat{u}_L\rho_L}{\hat{S}_{LL}^{(2)} - \hat{S}_{LL}^{(1)}} \quad (2.73)$$

The jumps  $\Delta\rho_{RR}^{(1)}$  and  $\Delta\rho_{RR}^{(2)}$  are calculated with the same methods described above,

$$\Delta\rho_{RR}^{(1)} = \frac{\hat{S}_{RR}^{(2)}(\rho_{RR}^{(3)} - \rho_R) + \hat{u}_R\rho_R - \hat{u}_{RR}^{(3)}\rho_{RR}^{(3)}}{\hat{S}_{RR}^{(2)} - \hat{S}_{RR}^{(1)}} \quad (2.74)$$

$$\Delta\rho_{RR}^{(2)} = \frac{\hat{S}_{RR}^{(1)}(-\rho_{RR}^{(3)} + \rho_R) - \hat{u}_R\rho_R + \hat{u}_{RR}^{(3)}\rho_{RR}^{(3)}}{\hat{S}_{RR}^{(2)} - \hat{S}_{RR}^{(1)}} \quad (2.75)$$

Also in the same way, the jumps  $\Delta\rho^{(1)}$  and  $\Delta\rho^{(2)}$  across the solution of the Riemann problem at the face shown in the figure 2.3 are calculated as

$$\Delta\rho^{(1)} = \frac{\hat{S}^{(2)}(\rho_R - \rho_L) + \hat{u}_L\rho_L - \hat{u}_R\rho_R}{\hat{S}^{(2)} - \hat{S}^{(1)}} \quad (2.76)$$

$$\Delta\rho^{(2)} = \frac{\hat{S}^{(1)}(\rho_L - \rho_R) - \hat{u}_L\rho_L + \hat{u}_R\rho_R}{\hat{S}^{(2)} - \hat{S}^{(1)}} \quad (2.77)$$

## 2.10 Unstructured Data Reconstruction for Higher Order Accuracy

High order accuracy can be achieved by reconstructing cell-centered data within hybrid cells (including polyhedral) to cell faces for flux computation. The face value  $\phi_f$  is reconstructed by the following expression:

$$\phi_f = \phi + \nabla\phi \cdot \vec{r} \quad (2.78)$$

where  $\phi$  and  $\nabla\phi$  are the cell centered value and its gradient at the cell center.  $\vec{r}$  is the vector from cell centroid to the face centroid. The gradient of the scalar  $\phi$  at the cell center  $c_0$  is calculated by Green-Gauss theorem,

$$(\nabla\phi)_{c0} = \frac{1}{V} \sum_f \bar{\phi}_f \vec{A}_f \quad (2.79)$$

$\bar{\phi}_f$  is the value of  $\phi$  at the face centroid and  $\vec{A}_f$  is the face area normal vector. The face value  $\bar{\phi}_f$  is calculated simply by averaging.

$$\bar{\phi}_f = \frac{\phi_{c0} + \phi_{c1}}{2} \quad (2.80)$$

The gradient  $\nabla\phi$  should be limited near high gradients to prevent oscillations and spurious solutions. One of the widely used limiter functions for unstructured grids is of Barth and Jespersen [5]. The limiter for the cell  $c$  is defined as

$$\Psi_c = \min_s \begin{cases} \min\left(1, \frac{\phi_{max} - \phi_s}{\Delta_2}\right) & \text{if } \Delta_2 > 0 \\ \min\left(1, \frac{\phi_{min} - \phi_s}{\Delta_2}\right) & \text{if } \Delta_2 < 0 \\ 1 & \text{if } \Delta_2 = 0 \end{cases} \quad (2.81)$$

where,

$$\begin{aligned} \Delta_2 &= \nabla\phi_c \cdot \vec{r}_{cs} \\ \phi_{max} &= \max(\phi_c, \max_s \phi_s) \\ \phi_{min} &= \min(\phi_c, \min_s \phi_s) \end{aligned} \quad (2.82)$$

In Eq. 2.82,  $\vec{r}_{cs}$  denotes the vector from centroid of the cell  $c$  to the mid point of the face between cell  $c$  and cell  $s$ .  $\max_s$  and  $\min_s$  means the maximum and minimum value of all direct neighbors  $s$  of cell  $c$ .  $\Delta_2$  is modified as  $Sign(\Delta_2)(|\Delta_2| + \omega)$ .

Another more popular limiter is of Venkatakrishnan's [52]. This limiter is widely used due to its better convergence properties.

$$\Psi_c = \min_s \begin{cases} \frac{1}{\Delta_2} \left[ \frac{(\Delta_{1,max}^2 + \epsilon^2) + 2\Delta_2^2 \Delta_{1,max}}{\Delta_{1,max}^2 + 2\Delta_2^2 + \Delta_{1,max} \Delta_2 + \epsilon^2} \right] & \text{if } \Delta_2 > 0 \\ \frac{1}{\Delta_2} \left[ \frac{(\Delta_{1,min}^2 + \epsilon^2) + 2\Delta_2^2 \Delta_{1,min}}{\Delta_{1,min}^2 + 2\Delta_2^2 + \Delta_{1,min} \Delta_2 + \epsilon^2} \right] & \text{if } \Delta_2 < 0 \\ 1 & \text{if } \Delta_2 = 0 \end{cases} \quad (2.83)$$

where

$$\begin{aligned} \Delta_{1,max} &= \phi_{max} - \phi_c \\ \Delta_{1,min} &= \phi_{min} - \phi_c \end{aligned} \quad (2.84)$$

In Eq. 2.84,  $\phi_{max}$  and  $\phi_{min}$  denote maximum or minimum values of all neighboring cells  $s$  and the cell  $c$  itself. The parameter  $\epsilon$  controls the amount of limiting.

## 2.11 Boundary Conditions

In this section, discretization and calculation procedures for some important boundary condition types are explained. Correct formulation of boundary conditions is crucial for robust simulations and also for physically correct results.

### 2.11.1 Mass Flow Inlet

Mass flow boundary condition can be used to provide a prescribed mass flow rate at a boundary face zone. The user provided total mass flow rate is used to calculate a mass flux for each face in the boundary zone. Mass flux  $\dot{m}$  is calculated by dividing the total mass flow rate  $\dot{m}_B$  with the total area  $A_B$  of the boundary face zone. The mass flux is at the same direction with the face normal vector and equal to  $\rho \hat{u}$ . Density is calculated with the procedure described below.

For an ideal gas, density is calculated using static pressure  $P$  and static temperature  $T$ ,

$$\rho = \frac{P}{RT} \quad (2.85)$$

Where the static pressure is calculated according to sign of the local wave speeds. If the inlet is supersonic the static pressure is equal to the user specified supersonic inlet pressure. Otherwise it is calculated from interior cells. The total temperature and the static temperature are related with the equation,

$$\frac{T_0}{T} = 1 + \frac{\gamma - 1}{2} \frac{u^2}{a^2} \quad (2.86)$$

The below relations for sound speed  $a$  and normal speed  $u$  can be used to derive a second order equation for density  $\rho$

$$a = \sqrt{\frac{\gamma P}{\rho}} \quad , \quad u = \frac{\dot{m}}{\rho} \quad (2.87)$$

Putting the right hand sides of the equations 2.87 in to the Eq. 2.86 the equation below is found,

$$2RT_0\rho^2\gamma - 2\rho\gamma P - (\gamma - 1)\dot{m}^2 = 0 \quad (2.88)$$

Solving the above equation for density  $\rho$ ,

$$\rho = \frac{\gamma P + \sqrt{\gamma^2 P^2 + 2RT_0\gamma^2\dot{m}^2 - 2RT_0\gamma\dot{m}^2}}{2RT_0\gamma} \quad (2.89)$$

In a more compact form,

$$\rho = \frac{\gamma P + \sqrt{\gamma} \sqrt{2Rm^2(\gamma - 1)T_0 + \gamma P^2}}{2RT_0\gamma} \quad (2.90)$$

The implementation of this boundary condition is done using the far field methods described in Section 2.11.7.

### 2.11.2 Pressure Outlet

At a pressure outlet face zone, a specified static pressure is used to calculate the pressures at the faces. The face pressures are calculated by a method based on the  $AUSM^+$  scheme [34]. In all the  $AUSM$ -family schemes, a general interface pressure formula [33] is used,

$$P_{1/2} = \mathcal{P}_n^+(M_L) P_L + \mathcal{P}_n^-(M_R) P_R \quad (2.91)$$

where  $\mathcal{P}_n$  are the  $n$ 'th order polynomials.  $M_L$  and  $M_R$  are the face normal Mach numbers defined as,

$$M_{L/R} = \frac{\hat{u}_{L/R}}{a_{1/2}} \quad (2.92)$$

where  $\hat{u}$  is the normal velocity. For the boundary faces, Eq. 2.91 is used in the following form (see Picture 2.5),

$$P_F = \mathcal{P}_5^+(M_n) P_D + \mathcal{P}_5^-(M_n) P_B \quad (2.93)$$

where  $M_n$  is the face normal Mach number. Then the face pressure  $P_F$  is a function of interior cell pressure  $P_D$ , specified boundary pressure  $P_B$  and normal Mach number  $M_n$ . The fifth order polynomials  $\mathcal{P}_{(5)}^\pm$  are given by the following formula,

$$\mathcal{P}_{(5)}^\pm = \begin{cases} \frac{1}{M_n} \mathcal{M}_{(1)}^\pm & \text{if } |M_n| \geq 1 \\ \mathcal{M}_{(2)}^\pm [(\pm 2 - M_n) \mp 16\alpha M_n \mathcal{M}_{(2)}^\mp] & \text{otherwise} \end{cases} \quad (2.94)$$

where  $\alpha$  were set to be 3/16 in [33] under the conditions described in the same reference. The split Mach numbers  $\mathcal{M}_{(m)}^\pm$  are polynomial functions of degree  $m$  as given in [33]:

$$\mathcal{M}_{(1)}^{\pm}(M_n) = \frac{1}{2}(M_n \pm |M_n|) \quad (2.95)$$

$$\mathcal{M}_{(2)}^{\pm}(M_n) = \pm \frac{1}{4}(M_n \pm 1)^2$$

### 2.11.3 Pressure Inlet

### 2.11.4 Subsonic Pressure Inlet

In this boundary condition, total pressure, total temperature is specified by user. The outgoing Riemann invariant is employed to determine speed of sound at the boundary [24, 9]. The outgoing Riemann invariant is defined as

$$\mathcal{R}^- = \vec{v}_d \cdot \vec{n} - \frac{2a_d}{\gamma - 1} \quad (2.96)$$

where the index  $d$  denotes the state inside the domain (Figures 2.4 and 2.5). The unit normal vector  $\vec{n}$  is assumed to point outwards of the domain. The speed of sound at the boundary for subsonic inlets is calculated as

$$a_b = \frac{-\mathcal{R}^-(\gamma - 1)}{(\gamma - 1)\cos^2\theta + 2} \left\{ 1 + \cos\theta \sqrt{\frac{[(\gamma - 1)\cos^2\theta + 2]a_0^2}{(\gamma - 1)(\mathcal{R}^-)^2} - \frac{\gamma - 1}{2}} \right\} \quad (2.97)$$

where  $\theta$  is the flow angle relative to the boundary and  $a_0$  is the stagnation speed of sound,

$$\cos\theta = -\frac{\vec{v}_d \cdot \vec{n}}{\|\vec{v}_d\|_2} \quad (2.98)$$

$$a_0^2 = a_d^2 + \frac{\gamma - 1}{2} \|\vec{v}_d\|_2^2 \quad (2.99)$$

Other quantities like static temperature  $T_b$ , static pressure  $P_b$ , density  $\rho_b$  and absolute velocity which are required to calculate fluxes on the boundary are found as,

$$T_b = T_0 \left( \frac{a_b^2}{a_0^2} \right) \quad (2.100)$$

$$P_b = P_0 \left( \frac{T_b}{T_0} \right)^{\frac{\gamma}{\gamma-1}} \quad (2.101)$$

$$\rho_b = \frac{P_b}{RT_b} \quad (2.102)$$

$$|u| = \sqrt{2C_p (T_0 - T_b)} \quad (2.103)$$

#### 2.11.4.1 Supersonic Pressure Inlet

If the inlet flow becomes supersonic the flow information comes from the boundary only. In this case static pressure  $P_b$  given by the user is used in addition to defined values of total pressure  $P_0$  and total temperature  $T_0$ .

$$T_b = T_0 \left( \frac{P_b}{P_0} \right)^{\frac{\gamma-1}{\gamma}} \quad (2.104)$$

$$\rho_b = \frac{P_b}{RT_b} \quad (2.105)$$

$$|u| = \sqrt{2C_p (T_0 - T_b)} \quad (2.106)$$

#### 2.11.5 Inviscid Wall

Wall boundary conditions are used to bound fluid zones. This boundary condition can also be used to separate two fluid zones or fluid and solid zones. For unstructured grids it was suggested to employ one layer of dummy cells in Ref. [17] and [16]. The velocity vector  $\vec{v}_d$  in a dummy cell were obtained by reflecting the velocity vector  $\vec{v}_w$  in the boundary cell at the wall. The velocity vector would become

$$\vec{v}_B = \vec{v}_D - 2|\vec{v}_D \cdot \vec{n}|\vec{n} \quad (2.107)$$

where  $\vec{n}$  is the wall face unit normal vector (see Pic.2.4) . Since the coordinate system was rotated so that the  $\hat{x}$  – *axis* is aligned with the face normal, the state vector  $U_B$  in the dummy cell is calculated easily as,

$$\hat{U}_B = \begin{bmatrix} \rho \\ -\rho\hat{u}_D \\ \rho\hat{v}_D \\ \rho\hat{w}_D \\ \rho E \end{bmatrix} \quad (2.108)$$

### 2.11.6 Symmetry Boundary Condition

The implementation of the symmetry boundary condition is done by employing dummy cells. The flow variables in the dummy cells are reflected while the scalar quantities like density and pressure are set equal to the values in the interior cells. The velocity components are reflected as indicated in Eq. 2.107.

### 2.11.7 Far Field Boundary Conditions

### 2.11.8 Far Field Supersonic Inflow

For supersonic inflow, all eigenvalues have the same sign. The conservative variables in the state on the boundary are determined by free stream values only (see Fig.2.4). Thus,

$$U_F = U_B \quad (2.109)$$

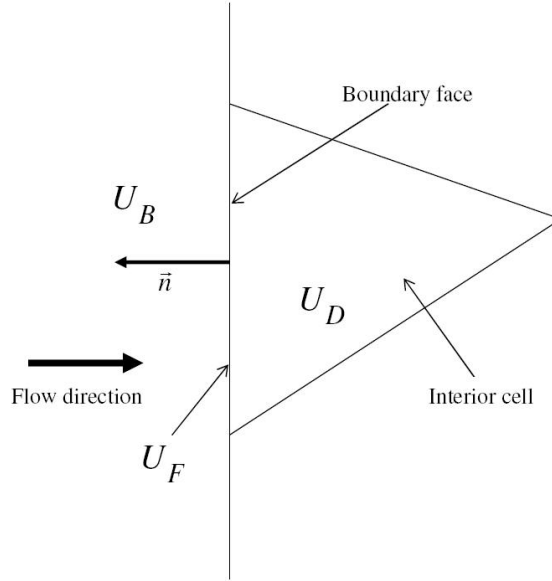


Figure 2.4: Far field inflow boundary.

### 2.11.8.1 Far Field Subsonic Inflow

In a subsonic inlet, four characteristics enter and one leaves the domain. Therefore four characteristic variables are prescribed based on the free stream values. One characteristic variable is extrapolated from the interior of the domain [9]. This leads to the following set of boundary conditions written in the local coordinate system [56] (see Fig. 2.5).

$$\begin{aligned}
 P_F &= \frac{1}{2} [P_B + P_D - \rho_0 a_0 (\hat{u}_B - \hat{u}_D)] \\
 \rho_F &= \rho_B + \frac{(P_F - P_B)}{a_0^2} \\
 \hat{u}_F &= \hat{u}_B - \frac{(P_B - P_F)}{\rho_0 a_0}
 \end{aligned} \tag{2.110}$$

where subscripts 0 represents reference state which is set equal to the state at the interior cell.

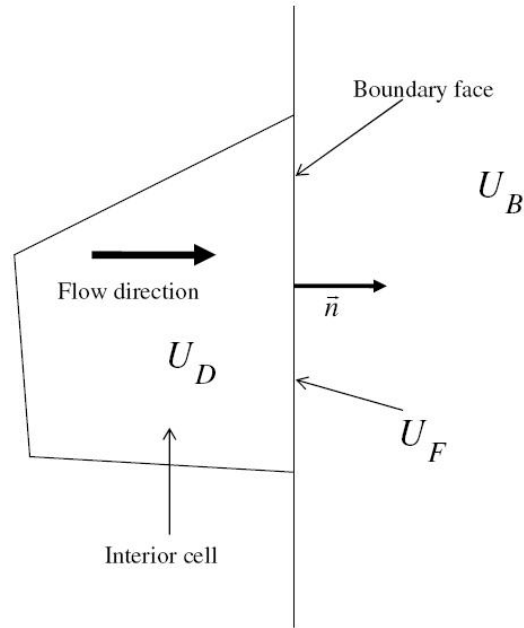


Figure 2.5: Far field outflow boundary.

### 2.11.8.2 Far Field Subsonic Outflow

For subsonic outflow boundary conditions, the static pressure must be defined by the user (see Fig. 2.5). Other flow variables are extrapolated from the interior of the solution domain [56].

$$\begin{aligned}
 P_F &= P_B \\
 \rho_F &= \rho_D + \frac{(P_F - P_D)}{a_0^2} \\
 \hat{u}_F &= \hat{u}_D + \frac{(P_D - P_F)}{\rho_0 a_0}
 \end{aligned}
 \tag{2.111}$$

## 2.12 Single Phase Test Cases

An explicit compressible flow solver named CMPS is developed based on the methods given previous chapters. This solver is validated against some test cases in the following sections.

### 2.12.1 Cylindrical Explosion in Two-Space Dimension

This test problem is like a two-dimensional counterpart of the shock tube problem. The two dimensional Euler equations are solved on a square domain of two zones. The square is  $2.0 \times 2.0$  in the  $x - y$  plane and there is a circle with radius  $R = 0.4$  at center of the square. Initially the flow variables takes constant values in each zone and joined by a circular discontinuity at the zone boundaries at time  $t = 0$  as shown in Fig. 2.6. The initial two constant states for two-dimensional Euler equations are chosen to be

$$\begin{aligned}
 P_{in} &= 1 \times 10^6 Pa & , & & P_{out} &= 101325 Pa \\
 T_{in} &= 375 K & , & & T_{out} &= 300 K \\
 u_{in} &= 0.0 & , & & u_{out} &= 0.0 \\
 v_{in} &= 0.0 & , & & v_{out} &= 0.0
 \end{aligned} \tag{2.112}$$

Subscripts *in* and *out* denote the values inside and outside the circle respectively.

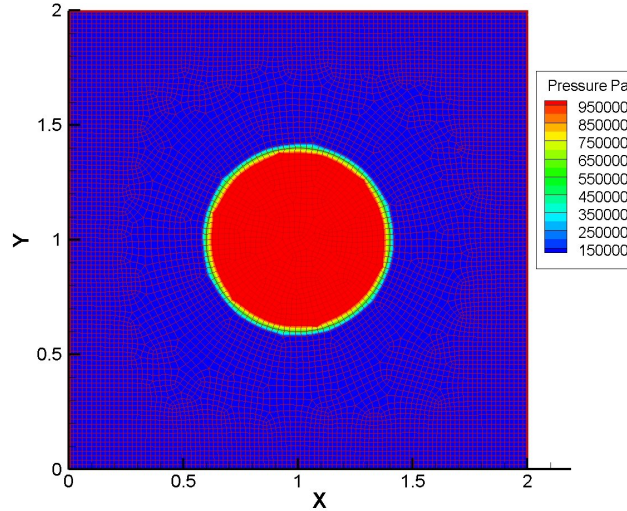


Figure 2.6: The unstructured multi zone grid structure and initial gauge pressure distribution.

The full two-dimensional Euler equations are solved by the CMPS code based on methods explained in previous sections in this chapter. The solution is repeated with Rusanov, Lax-Friedrichs, HLL and HLLC Riemann solvers with CFL number  $C_{CFL} = 2.0$ . Additionally the same solution is repeated with commercial CFD software FLUENT with its first order explicit Roe solver. The pressure, density and  $x$

velocity contours at time  $t = 7.7 \times 10^{-4}$  calculated with HLLC Riemann solver are shown in Figures 2.7, 2.8 and 2.9 respectively. The effects of the mesh on the solution can be seen in the all contours. The same effects are also observed with FLUENT and the results are indistinguishable from the results obtained by CMPS with HLLC Riemann solver.

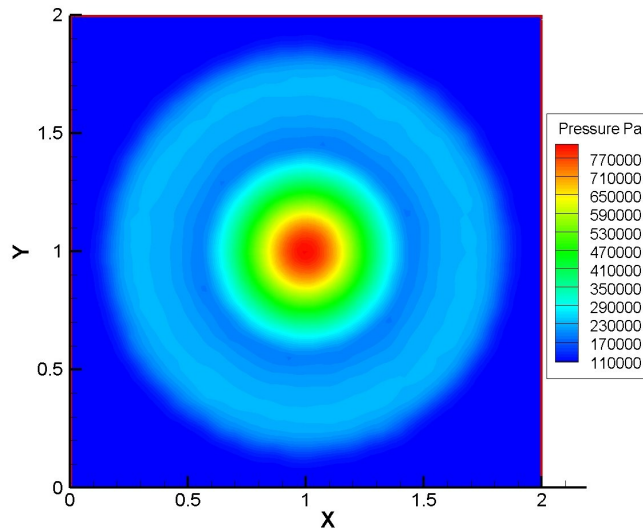


Figure 2.7: Cylindrical explosion in two-space dimensions. Pressure distribution at  $7.7 \times 10^{-4}$  seconds calculated by the first order solver using HLLC Riemann solver.

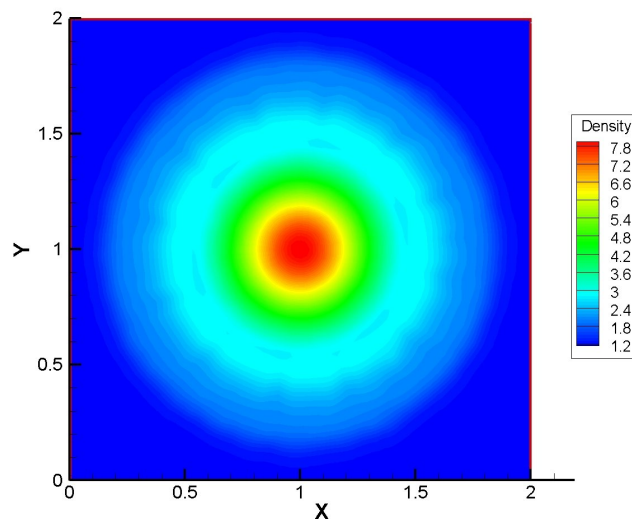


Figure 2.8: Cylindrical explosion in two-space dimensions. Density distribution at  $7.7 \times 10^{-4}$  seconds calculated by the first order solver of CMPS using HLLC Riemann solver.

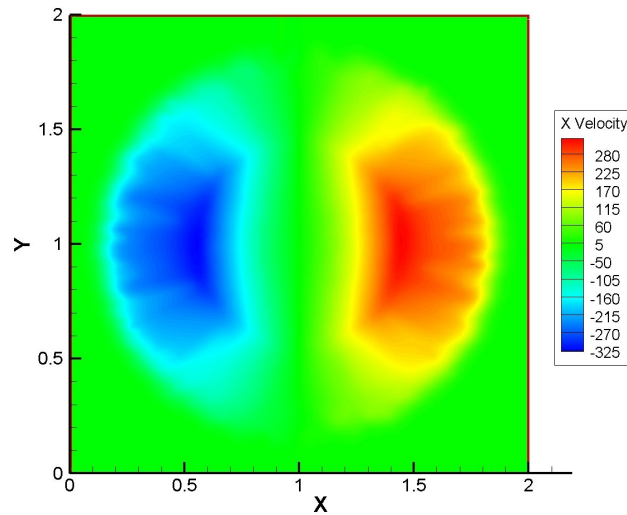


Figure 2.9: Cylindrical explosion in two-space dimensions.  $x$  velocity distribution at  $7.7 \times 10^{-4}$  seconds calculated by the first order solver of CMPS using HLLC Riemann solver.

The solution exhibits a circular shock wave traveling away from the center, a circular contact surface traveling in the same direction and a circular rarefaction traveling toward the origin.

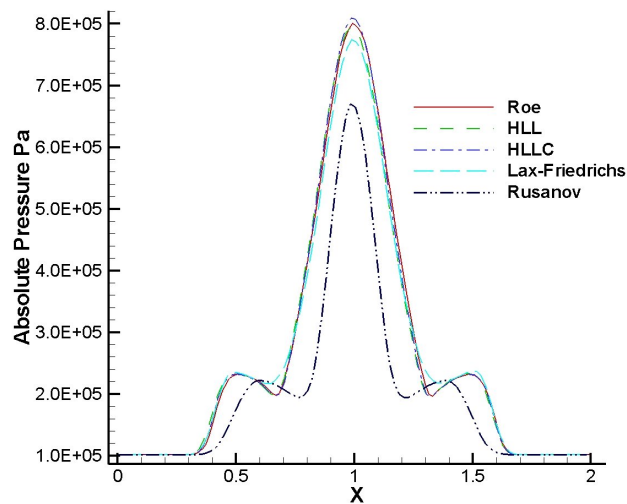


Figure 2.10: Cylindrical explosion in two-space dimensions. Pressure distributions at  $7.7 \times 10^{-4}$  seconds calculated by the first order solvers of CMPS using different flux functions. The solution with Roe solver is the result of FLUENT's first order explicit solver.

Fig. 2.10 shows a comparison between the solutions obtained with different flux

functions and also the result of FLUENT’s first order explicit Roe solver. The Roe and HLL and HLLC Riemann solvers gave similar results. Due to its high diffusive character of Lax-Friedrichs, its results are not sharp as the Roe, HLL and HLLC. Rusanov is too diffusive to be used for practical purposes.

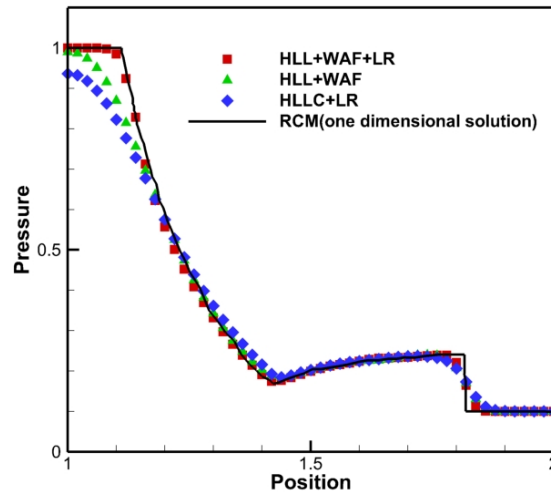


Figure 2.11: Cylindrical explosion in two-space dimensions.  $x$  pressure distribution at  $7.7 \times 10^{-4}$  seconds calculated by the high order solvers of CMPS.

The problem is also solved with high order methods. In CMPS, it is possible to use WAF and linear reconstruction (LR) methods at the same time which provides higher spatial resolution than using WAF or LR methods alone. Results are shown in Fig. 2.11.

### 2.12.2 Spherical Explosion In Three Space Dimensions

The three dimensional Euler equations are solved on a cube  $2.0 \times 2.0 \times 2.0$  in  $x - y - z$  space with first order solver of the CMPS code using HLLC Riemann solver. The domain consists of two zones with a spherical zone with radius  $R = 0.4$  at the center of the cube. Grid includes 406000 tetrahedral elements. The initial state values take constant values in each zone and are the same as those in section 2.12.1. The initial pressure distribution is shown in Fig. 2.12. Pressure, density and internal energy contours at time  $t = 7.7 \times 10^{-4}$  are shown in Figures 2.13, 2.14 and 2.15 respectively.

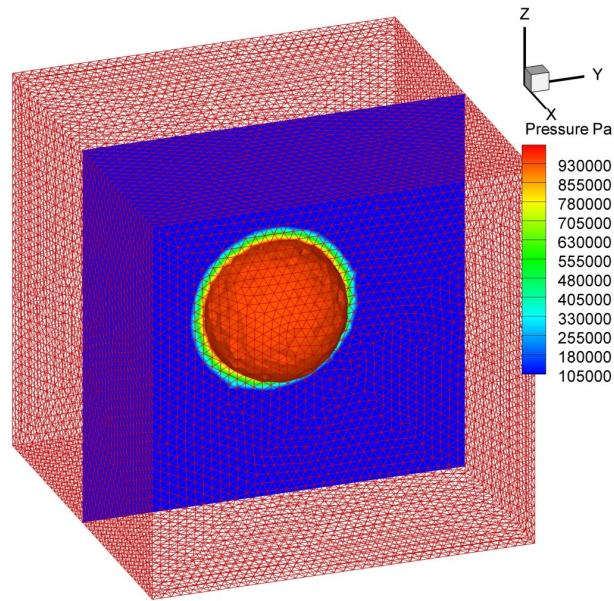


Figure 2.12: Spherical explosion in three space dimensions. Initial pressure distribution and grid structure. The spherical zone at the center is the initial high pressure region.

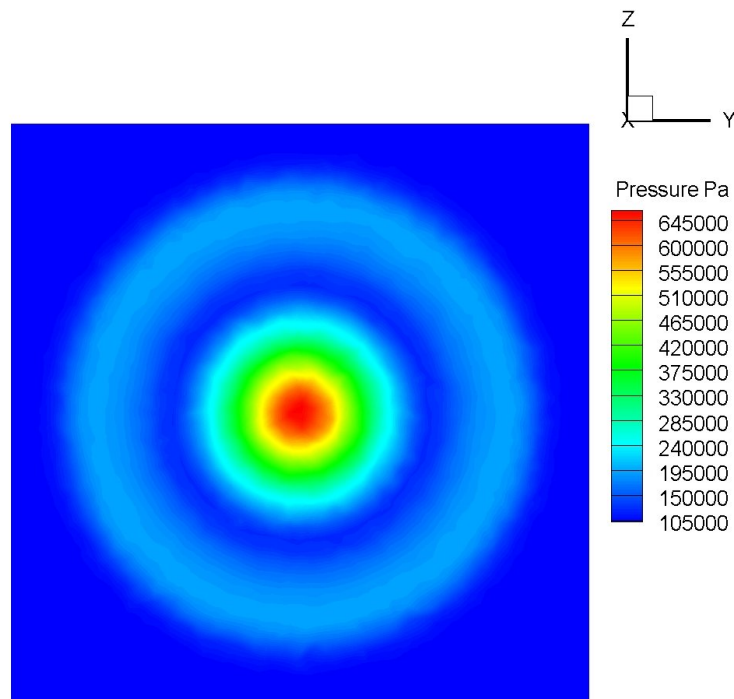


Figure 2.13: Spherical explosion in three space dimensions. Pressure distribution at time  $t = 4.7 \times 10^{-4}$  calculated with first order solver of CMPS using HLLC Riemann solver.

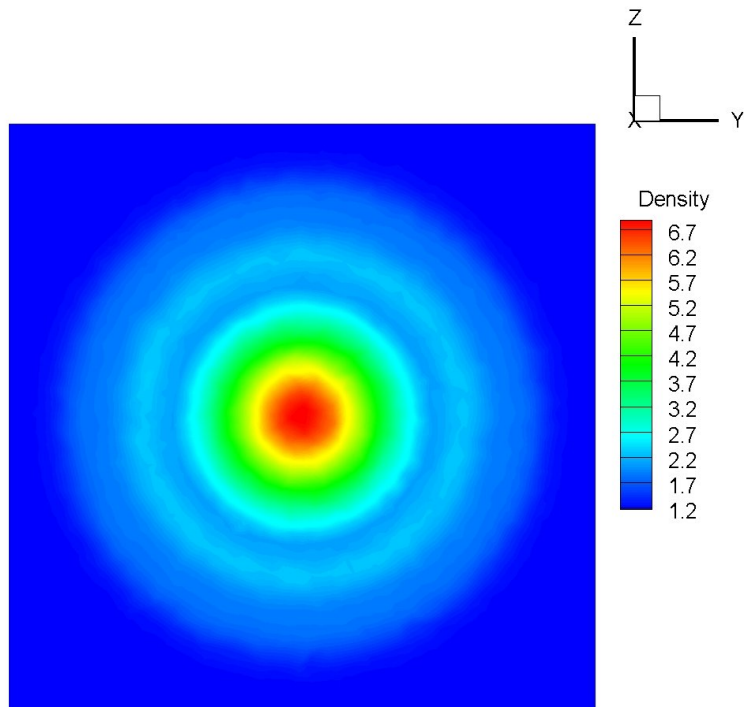


Figure 2.14: Spherical explosion in three space dimensions. Density distribution at time  $t = 4.7 \times 10^{-4}$  calculated with first order solver of CMPS using HLLC Riemann solver.

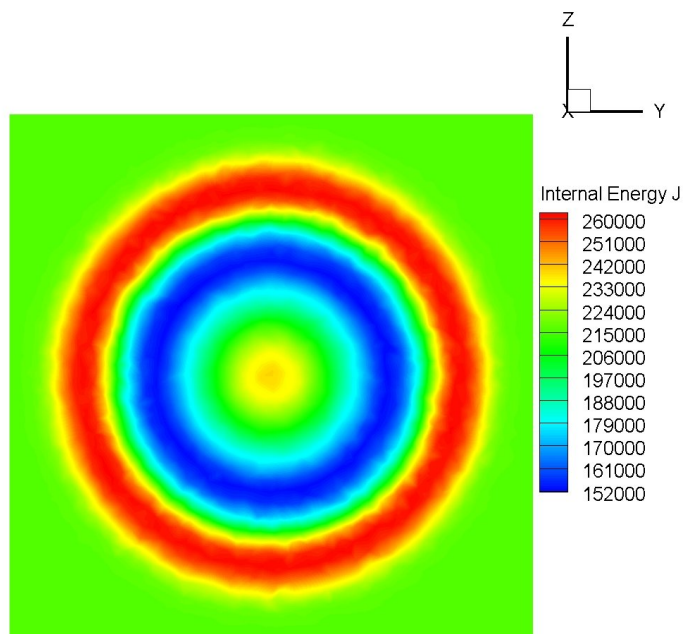


Figure 2.15: Spherical explosion in three space dimensions. Internal energy distribution at time  $t = 4.7 \times 10^{-4}$  calculated with first order solver of CMPS using HLLC Riemann solver.

The problem is also solved with high order methods. In CMPS, it is possible to use WAF and linear reconstruction (LR) methods at the same time which provides higher spatial resolution than using WAF or LR methods alone. Results are shown in Fig. 2.17. These solution are compared to a one dimensional solution in spherical coordinates obtained with Random Choice Method (RCM) of Chorin [10]. RCM method provides exact solution of Riemann problems in one dimension but not applicable to multidimensional problems.

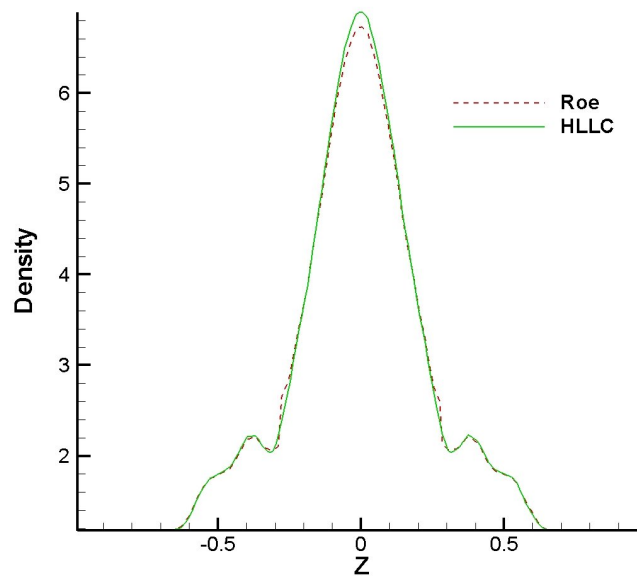


Figure 2.16: Spherical explosion in three space dimensions. Density distributions at time  $t = 4.7 \times 10^{-4}$  calculated with first order solver of CMPS using HLLC Riemann solver and first order solver of FLUENT using Roe.

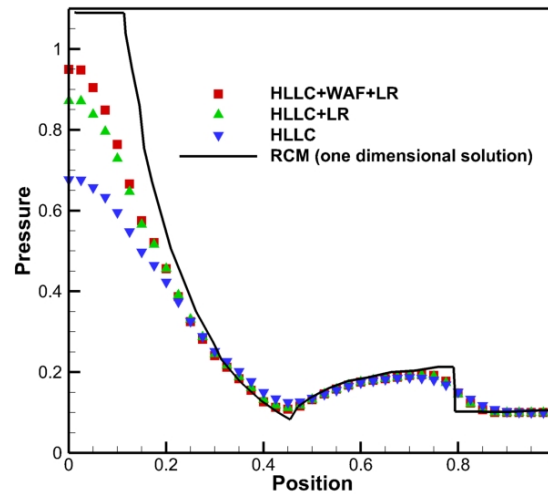


Figure 2.17: Cylindrical explosion in two-space dimensions.  $x$  pressure distribution at  $7.7 \times 10^{-4}$  seconds calculated by the high order solvers of CMPS.

### 2.12.3 Supersonic Flow Over a Circular Arc Bump

The solution of Euler equations for a supersonic flow over a circular bump is studied. The flow entering the channel is supersonic at 1.88 Mach. The Mach number contours calculated with first order HLLC Riemann solver of the CMPS code are shown in Fig. 2.18. A shock is generated as flow reaches the bump. This shock is reflected by the upper wall then crosses the another shock which issues from the end of the bump. The two shock meets again before exiting the supersonic channel. The calculations are repeated with Rusanov, Lax-Friedrich and HLL flux functions also with first order Roe solver of FLUENT for comparison. HLL and HLLC solvers of the CMPS code give indistinguishable results in good agreement with Roe solver of FLUENT. Lax-Friedrich solver of the CMPS code is more diffusive as expected. Rusanov was unsuccessful to provide a meaningful result for comparison. The Mach number and pressure profiles along the channel are shown in Figures 2.19 and 2.20 respectively.

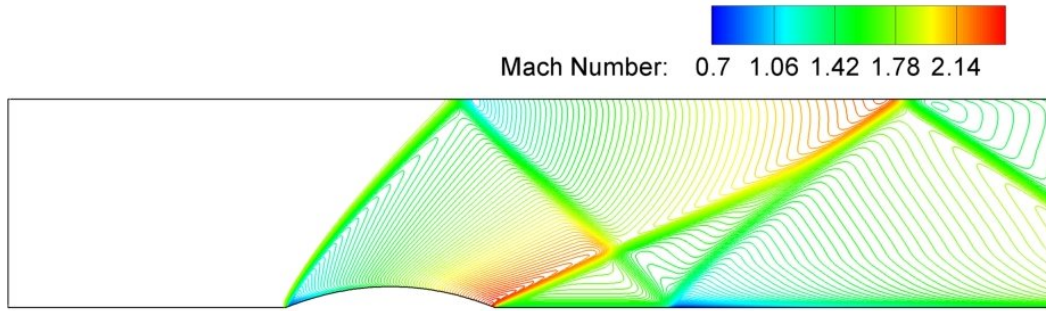


Figure 2.18: Mach number contours for supersonic flow over a circular bump calculated with first order HLLC Riemann solver of CMPS code.

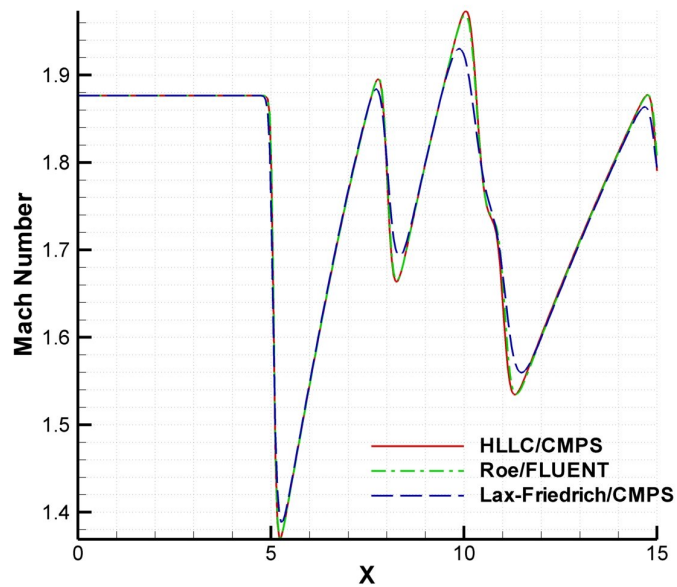


Figure 2.19: Mach number along the supersonic flow over a circular bump shown in Fig. 2.18.

#### 2.12.4 Transonic Flow Over Circular Bump

In this test case the solution of Euler equations is studied for a transonic flow over a circular bump. Air enters the channel at 0.67 Mach then becomes supersonic over the bump and a shock develops behind the bump. The Mach number contours are shown in Fig. 2.21. The line plot of Mach numbers through the channel calculated by CMPS and FLUENT are shown in Fig. 2.22.

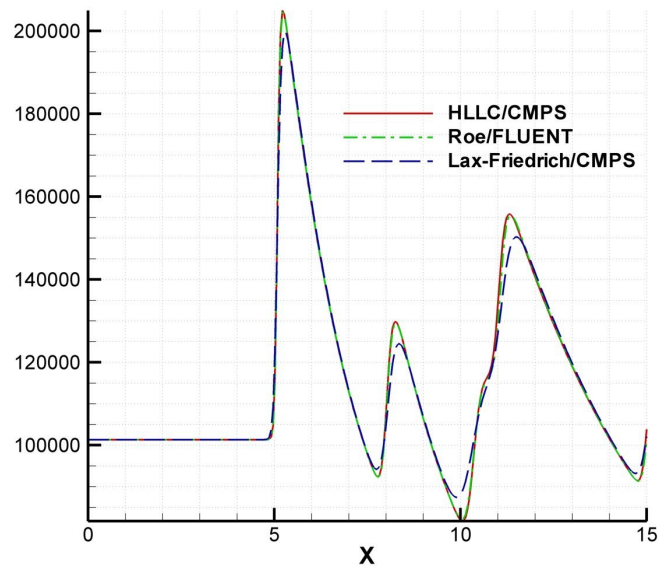


Figure 2.20: Pressure profile along the supersonic flow over a circular bump shown in Fig. 2.18

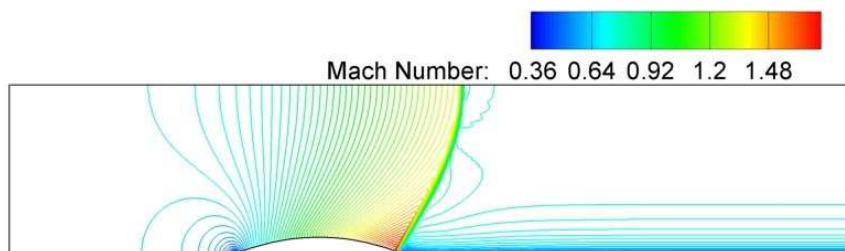


Figure 2.21: Mach number contours for transonic flow over a circular bump calculated with first order HLLC Riemann solver of CMPS code.

Properties			Initial conditions	
Mass specific energy ( <i>kJ/kg</i> )	Density ( <i>kg/m<sup>3</sup></i> )	Mass ( <i>kg</i> )	Pressure <i>Pa</i>	Temperature <i>K</i>
4870	1580	0.185	3077840000	6937

Table 2.1: Properties of plastic explosive and the calculated initial values for modeling the explosion.

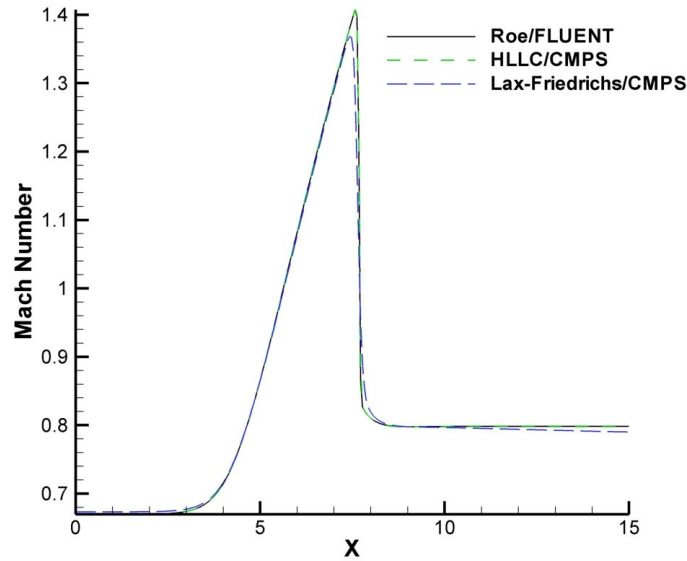


Figure 2.22: Mach number along the transonic flow over the bump shown in Fig. 2.21.

### 2.12.5 Blast Propagation In A Three Dimensional L-Shaped Tunnel

In this test case an air blast propagation was studied in the L-shaped tunnel. The geometry of the solution domain is shown in Fig. 2.23. During the solution pressure values are monitored in three points shown in Fig. 2.23. For this test case experimental results are available, in the original experiment a plastic explosive was used. This explosive is modeled as a spherical air volume with initial conditions calculated using ideal gas law. The properties of the plastic explosive and calculated initial conditions are given in Table 2.1. Some contour plots at times  $t = 0.30 \times 10^{-3}$  seconds and  $t = 0.43 \times 10^{-3}$  seconds are shown in Figures 2.23, 2.24, 2.26 and 2.27.

The experimental results and the results recorded at probe locations shown in figure

2.23 during simulation are compared in Figures 2.28, 2.29, 2.30. Although the simulation results are sufficiently in agreement with the experimental results, there are some differences especially at probe 2. The source of these differences may result from the physical assumptions made during the simulation. These assumptions are,

- The properties of the explosion gases were unknown, they were modeled as air.
- Air was modeled as ideal gas although it behaved as real gas.
- The walls of the test unit were assumed to be adiabatic. This assumption prevents the damping effect of the walls on the blast waves.

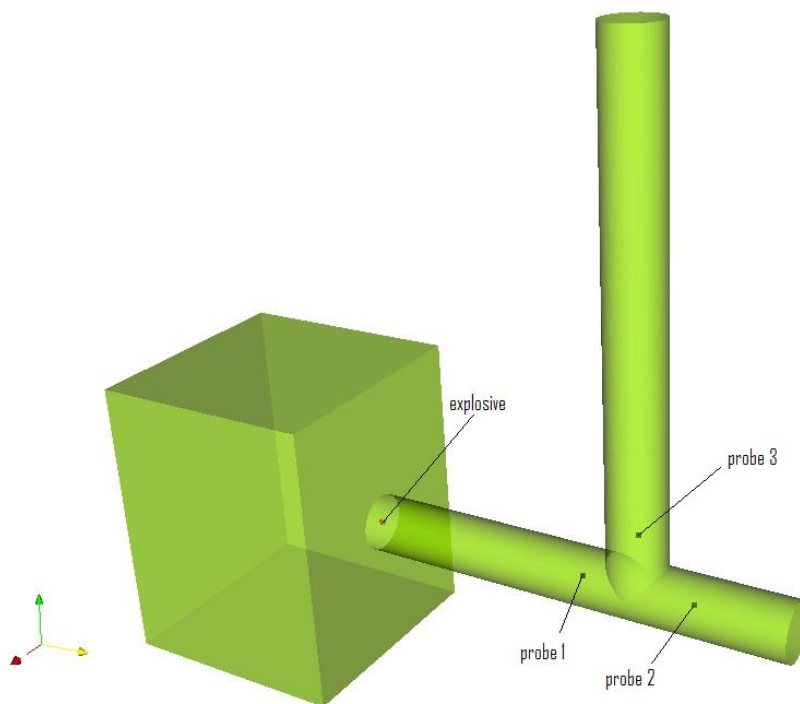


Figure 2.23: Geometry of the test case for blast wave propagation in L-Shaped tunnel.

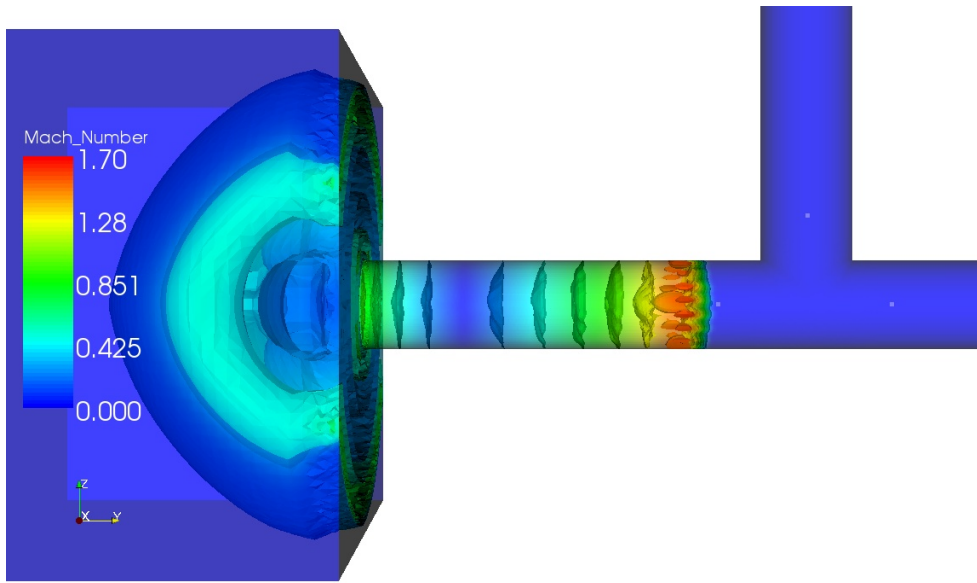


Figure 2.24: Mach number contours at time  $t = 0.30 \times 10^{-3}$  seconds.

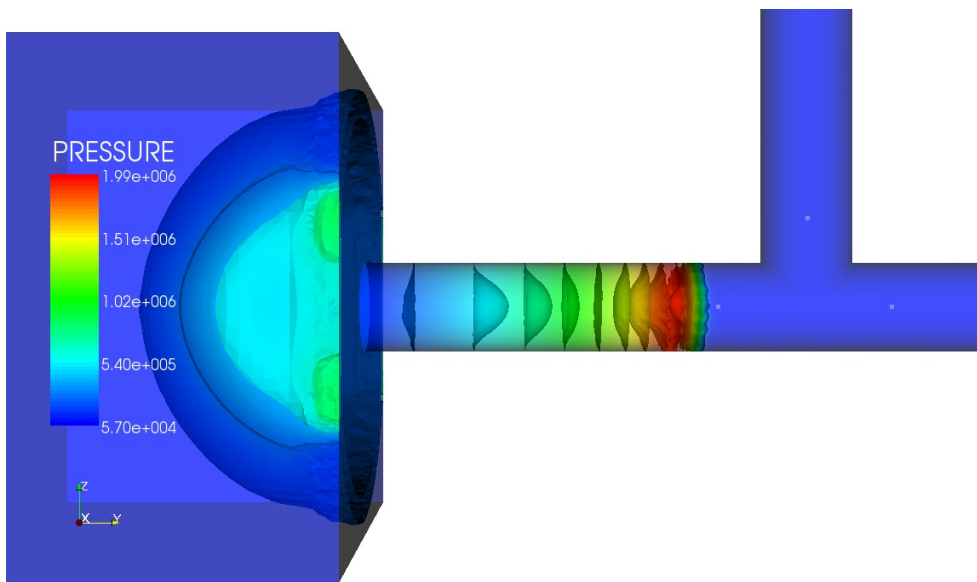


Figure 2.25: Absolute pressure contours at time  $t = 0.30 \times 10^{-3}$  seconds.

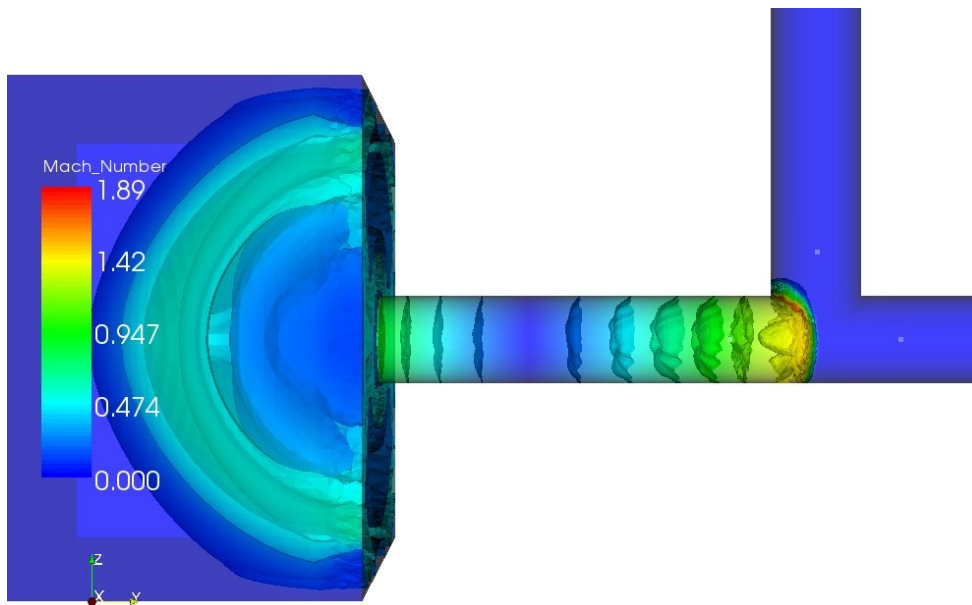


Figure 2.26: Mach number contours at time  $t = 0.43 \times 10^{-3}$  seconds

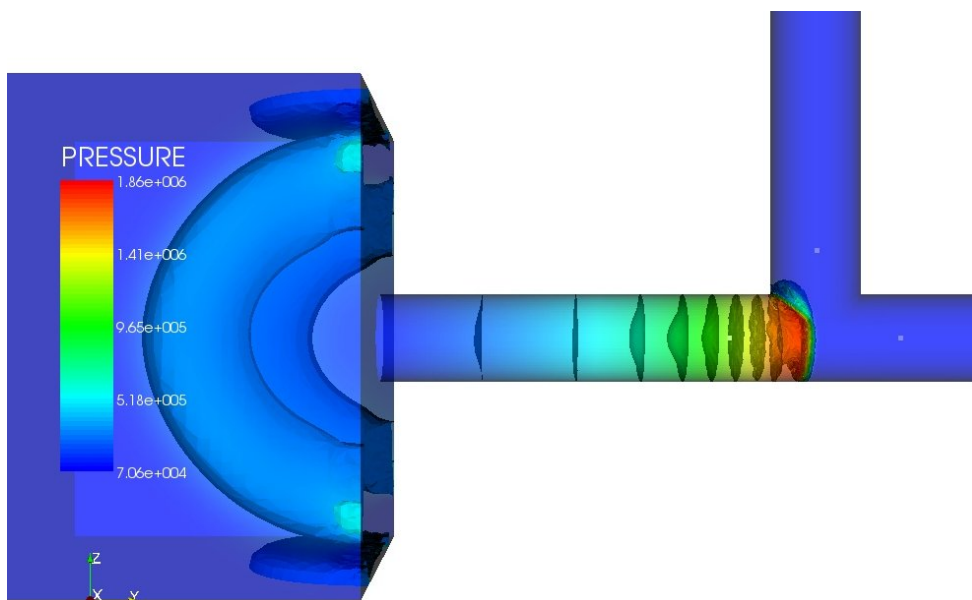


Figure 2.27: Absolute pressure contours at time  $t = 0.43 \times 10^{-3}$  seconds.

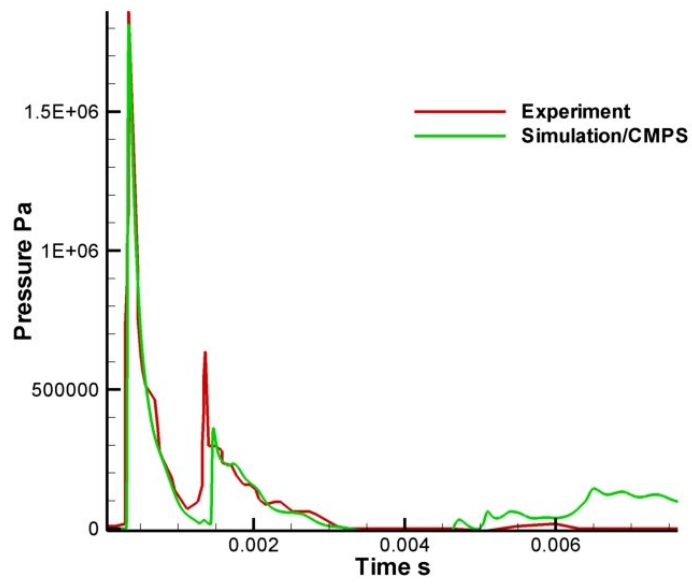


Figure 2.28: Pressure probe at probe 1.

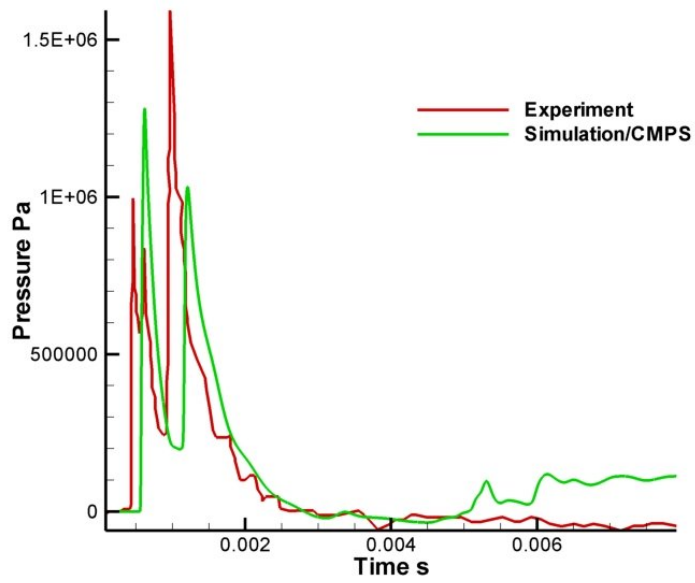


Figure 2.29: Pressure probe at probe 2.

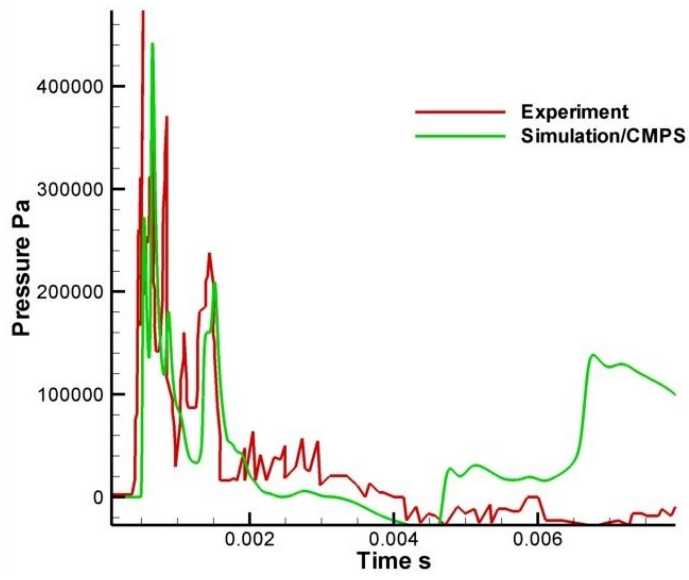


Figure 2.30: Pressure probe at probe 3.



## CHAPTER 3

### MULTIDIMENSIONAL MULTI-PHASE GODUNOV METHODS FOR COMPRESSIBLE MULTI-PHASE FLOWS

In this chapter, the method proposed by Saurel and Abgrall [42] is extended to multi dimensional unstructured grids and the solution procedure is explained. This Godunov scheme is based on the solution of an averaged system of equations similar to the equation system derived in [4]. This system of equations is given below in 3.1,

$$\begin{aligned}
 \frac{\partial \alpha_g}{\partial t} + V_I \frac{\partial \alpha_g}{\partial x} &= 0 \\
 \frac{\partial \alpha_g \rho_g}{\partial t} + \frac{\partial \alpha_g \rho_g u_g}{\partial x} &= \dot{m} \\
 \frac{\partial \alpha_g \rho_g u_g}{\partial t} + \frac{\partial (\alpha_g \rho_g u_g^2 + \alpha_g P_g)}{\partial x} &= P_I \frac{\partial \alpha_g}{\partial x} + \dot{m} V_I + F_d \\
 \frac{\partial \alpha_g \rho_g E_g}{\partial t} + \frac{\partial u_g (\alpha_g \rho_g E_g + \alpha_g P_g)}{\partial x} &= P_I V_I \frac{\partial \alpha_g}{\partial x} + \dot{m} E_I + F_d V_I + Q_I \\
 \frac{\partial \alpha_s \rho_s}{\partial t} + \frac{\partial \alpha_s \rho_s u_s}{\partial x} &= -\dot{m} \\
 \frac{\partial \alpha_s \rho_s u_s}{\partial t} + \frac{\partial (\alpha_s \rho_s u_s^2 + \alpha_s P_s)}{\partial x} &= -P_I \frac{\partial \alpha_g}{\partial x} - \dot{m} V_I - F_d \\
 \frac{\partial \alpha_s \rho_s E_s}{\partial t} + \frac{\partial u_s (\alpha_s \rho_s E_s + \alpha_s P_s)}{\partial x} &= -P_I V_I \frac{\partial \alpha_g}{\partial x} - \dot{m} E_I - F_d V_I - Q_I
 \end{aligned} \tag{3.1}$$

where,

$\alpha_k$  is volume fraction, and  $\alpha_g + \alpha_s = 1$ ,

$V_I$  is inter facial velocity,

$P_I$  is inter facial pressure,

$E_I$  is Total energy,  $E_k = e_k + \frac{1}{2}u^2$ ,

$F_I$  is the momentum transfer term between the phases.

The equation system (3.1) include non-conservative terms;  $-P_I \partial \alpha_g / \partial x$  and  $-P_I V_I \partial \alpha_g / \partial x$ . The pressure  $P_I$  and the velocity  $V_I$  represent averaged values of the inter facial pressure and velocity over the two-phase control volume.

Often, some closure models necessitate determination of characteristic size parameters of individual particles such as particle sizes. In these situations a new equation may be added to the existing ones to determine the particle sizes and inter facial areas, which may be in the form of inter facial area transport equation(IATE).

$$\frac{\partial a_I}{\partial t} + \nabla (a_I V_I) = \frac{2}{3} \left( \frac{a_I}{\alpha_s} \right) \left( \frac{\partial \alpha_s}{\partial t} + \nabla \alpha_s \vec{u}_s - \eta_{ph} \right) + \sum_j \phi_j + \phi_{ph} \quad (3.2)$$

where  $a_I$  is inter facial area concentration and the terms  $\phi_j$  and  $\phi_{ph}$  source terms. Particle sizes can be related to  $a_I$  and  $\alpha_s$  for spherical particles as

$$D_{sm} = \frac{6\alpha_s}{a_I} \quad (3.3)$$

Equations 3.2 and 3.3 can be solved uncoupled from the system Equations 3.1. So, they do not change its mathematical properties, nor its solution.

Inter facial velocity  $V_I$  can be modeled as mass averaged;

$$V_I = \frac{\sum \alpha_k \rho_k u_k}{\sum \alpha_k \rho_k} \quad (3.4)$$

Inter facial pressure  $P_I$  is modeled as mixture pressure,

$$P_i = \sum_k \alpha_k P_k \quad (3.5)$$

$P_k$  are given by appropriate equations of state (EOS) of the form  $P_k = P_k(e_k, \rho_k)$ . The most classical equation of states generally used are given below;

1. Ideal gas EOS:

$$P = e\rho(\gamma - 1) \quad (3.6)$$

where  $\gamma$  is the specific heat ratio  $\gamma = C_p/C_v$ . The speed of sound in an ideal gas is given by

$$a = \sqrt{\frac{\gamma P}{\rho}} \quad (3.7)$$

2. Stiffened gas EOS:

$$P = \rho(\gamma - 1)e - \gamma P_\infty \quad (3.8)$$

where  $P_\infty$  is a constant parameter. The speed of sound is

$$a = \sqrt{\frac{\gamma(P + P_\infty)}{\rho}} \quad (3.9)$$

### 3.1 Numerical Method

#### 3.1.1 Non-conservative Terms

The discretization of non-conservative terms  $-P_I \partial \alpha_g / \partial x$  and  $-P_I V_I \partial \alpha_g / \partial x$  need special methods. These methods can be developed according to Abgrall[1] criterion. It states that: "A two phase flow, uniform in pressure and velocity must remain uniform on the same variables during its temporal evolution". If  $u = u_g = u_s = V_I$  and as well as  $P = P_g = P_s = P_I$  at time  $t = 0$  then the velocities and the pressure will keep the same values [42]. Most spatial derivatives cancel and we get;

$$\begin{aligned} \frac{\partial \alpha_g}{\partial t} + u \frac{\partial \alpha_g}{\partial x} &= 0 \\ \frac{\partial \rho_g}{\partial t} + u \frac{\partial \rho_g}{\partial x} &= 0 \\ \frac{\partial u_g}{\partial t} &= 0 \end{aligned}$$

$$\begin{aligned}\frac{\partial P_g}{\partial t} &= 0 \\ \frac{\partial \rho_s}{\partial t} + u \frac{\partial \rho_s}{\partial x} &= 0 \\ \frac{\partial u_s}{\partial t} &= 0 \\ \frac{\partial P_s}{\partial t} &= 0\end{aligned}$$

For one dimensional cases, discretization of non-conservative terms can be found in reference [42]. Here two dimensional cases are considered.

### 3.1.1.1 Godunov-Rusanov Scheme

Here we consider only the volume fraction, gas continuity, gas momentum and gas energy equations in 3.1.

$$\frac{\partial \alpha}{\partial t} + V_I \nabla \alpha = 0 \quad (3.10)$$

$$\frac{\partial U}{\partial t} + \frac{\partial F(U)}{\partial x} + \frac{\partial G(U)}{\partial y} = H(U) \nabla \alpha \quad (3.11)$$

where  $U$  is the state vector,  $F(U)$ , and  $G(U)$  are flux vectors, and  $H$  is the coefficients of the non-conservative terms  $\nabla \alpha$ ;

$$U = \begin{bmatrix} \alpha \rho \\ \alpha \rho u \\ \alpha \rho v \\ \alpha \rho E \end{bmatrix}, \quad F = \begin{bmatrix} \alpha \rho u \\ \alpha \rho u^2 + \alpha P \\ \alpha \rho uv \\ \alpha u(\rho E + P) \end{bmatrix}, \quad G = \begin{bmatrix} \alpha \rho v \\ \alpha \rho uv \\ \alpha \rho v^2 + \alpha P \\ \alpha v(\rho E + P) \end{bmatrix}$$

$$H = \begin{bmatrix} 0 & 0 \\ P & 0 \\ 0 & P \\ Pu_I & Pv_I \end{bmatrix}, \quad \nabla \alpha = \begin{bmatrix} \frac{\partial \alpha}{\partial x} \\ \frac{\partial \alpha}{\partial y} \end{bmatrix} \quad (3.12)$$

The finite volume scheme for solving equation 3.11 can be written as,

$$U^{n+1} = U^n - \frac{\Delta t}{V} \sum_{s=0}^N A_s T_s^{-1} \hat{F}_s^n \quad (3.13)$$

In Eq. 3.13,  $s$  is the index of cell faces,  $A_s$  is the area of cell faces.  $T_s^{-1}$  is the inverse of the rotation matrix  $T$ ,

$$T = \begin{bmatrix} 1 & 0 & 0 & 0 \\ 0 & \cos(\theta_s) & \sin(\theta_s) & 0 \\ 0 & -\sin(\theta_s) & \cos(\theta_s) & 0 \\ 0 & 0 & 0 & 1 \end{bmatrix}, \quad T^{-1} = \begin{bmatrix} 1 & 0 & 0 & 0 \\ 0 & \cos(\theta_s) & -\sin(\theta_s) & 0 \\ 0 & \sin(\theta_s) & \cos(\theta_s) & 0 \\ 0 & 0 & 0 & 1 \end{bmatrix} \quad (3.14)$$

$\hat{F}_s$  is the flux at the face, which is the function of transformed state vectors  $\hat{F}_s = \hat{F}_s(\hat{U}_{s,c})$  defined as  $\hat{U}_{s,c} = T U_{s,c}$ . Index  $s$  refers to the faces of the cell.  $c$  is 0 for the host cell and 1 for the neighboring cell. For the Rusanov flux,  $\hat{F}_s^n$  is calculated as,

$$\hat{F}_s^n = \hat{F}_s^n(\hat{U}_{s,0}^n, \hat{U}_{s,1}^n) = \frac{1}{2} \left[ \hat{F}_{s,0}^n + \hat{F}_{s,1}^n - \hat{S}^n (\hat{U}_{s,1}^n - \hat{U}_{s,0}^n) \right] \quad (3.15)$$

where  $\hat{S} = \max \{ |\hat{u}_L - a_L|, |\hat{u}_R - a_R|, |\hat{u}_L + a_L|, |\hat{u}_R + a_R| \}$

### 3.1.1.2 Gradient of Gas Volume Fraction $\alpha$

Using the equation 3.13 and uniformity of velocity  $u^{n+1} = u^n$ ,  $v^{n+1} = v^n$  (Abgrall[1] criterion) following relations can be written for  $x$  velocity  $u$ ;

$$u U^{n+1}[1] = U^{n+1}[2] \quad (3.16)$$

$$v U^{n+1}[1] = U^{n+1}[3] \quad (3.17)$$

Solving the above equations, following formulas are found for  $\frac{\partial \alpha}{\partial x}$  and  $\frac{\partial \alpha}{\partial y}$ ;

$$\frac{\partial \alpha^n}{\partial x} = \frac{1}{2V} \sum_{s=0}^{N-1} A_s \cos(\theta_s) (\alpha_{s,0}^n + \alpha_{s,1}^n) = \frac{1}{2V} \sum_{s=0}^{N-1} \vec{A}_s[0] (\alpha_{s,0}^n + \alpha_{s,1}^n) \quad (3.18)$$

$$\frac{\partial \alpha^n}{\partial y} = \frac{1}{2V} \sum_{s=0}^{N-1} A_s \sin(\theta_s) (\alpha_{s,0}^n + \alpha_{s,1}^n) = \frac{1}{2V} \sum_{s=0}^{N-1} \vec{A}_s [1] (\alpha_{s,0}^n + \alpha_{s,1}^n) \quad (3.19)$$

where  $\vec{A}_s$  is the area normal vector of surface and  $A_s = \|\vec{A}_s\|$ . Above equations can be written in the following compact form,

$$\nabla \alpha = \frac{1}{2V} \sum_{s=0}^{N-1} \vec{A}_s (\alpha_{s,0}^n + \alpha_{s,1}^n) \quad (3.20)$$

### 3.1.1.3 Discretization of Volume Fraction Equation

Heuze[22] showed that nearly all equation of states can be written in the Mia-Gruneisen form

$$\rho e = \beta(\rho) P + \eta(\rho) \quad (3.21)$$

with  $\beta = 1/(\gamma - 1)$  and  $\eta = \gamma\pi(\gamma - 1)$ . Now replacing the terms  $\rho e$  in state and flux vectors with  $\beta P + \eta$  and using Eq.3.13, following formula can be written(see [42]),

$$\alpha^{n+1} \left[ (\beta P + \eta) + \rho^{n+1} \frac{1}{2} (u^2 + v^2) \right] = U^{n+1} [4] \quad (3.22)$$

Eq.3.22 can be rewritten in the form,

$$\alpha^{n+1} (\beta P + \eta) + U^{n+1} [1] \frac{1}{2} (u^2 + v^2) = U^{n+1} [4] \quad (3.23)$$

Solving Eq.3.23 for  $\alpha^{n+1}$ , following formula is found

$$\alpha^{n+1} = \alpha^n - \underbrace{\frac{\Delta t}{2V} \sum_{s=0}^{N-1} (\vec{A}_s \cdot \vec{V}_i^n) (\alpha_{s,0}^n + \alpha_{s,1}^n)}_{Convective Term} - \underbrace{\frac{\Delta t}{2V} \sum_{s=0}^{N-1} A_s \hat{S}_s^n (\alpha_{s,0}^n - \alpha_{s,1}^n)}_{Viscosity Term} \quad (3.24)$$

Equation 3.24 gives the numerical scheme that must be used to solve the non-conservative volume fraction equation in 3.1. The scheme is strictly related to the flux function used for conservative terms. The second term on the right hand side of the Eq. 3.24 is the classical discretized form of the convective term. Third term on the right hand side of the Eq. 3.24 represent a viscosity term, which is also a direct function of the flux functions written for the conservative terms.

The summary of Godunov-Rusanov scheme is below,

Conservation equation:

$$U^{n+1} = U^n - \frac{\Delta t}{V} \sum_{s=0}^N A_s T_s^{-1} \hat{F}_s^n \quad (3.25)$$

Flux function:

$$\hat{F}_s^n = \frac{1}{2} \left[ \hat{F}_{s,0}^n + \hat{F}_{s,1}^n - \hat{S}^n (\hat{U}_{s,1}^n - \hat{U}_{s,0}^n) \right] \quad (3.26)$$

Non-conservative source terms:

$$\nabla \alpha^n = \frac{1}{2V} \sum_{s=0}^{N-1} \vec{A}_s (\alpha_{s,0}^n + \alpha_{s,1}^n) \quad (3.27)$$

Volume-fraction equation:

$$\alpha^{n+1} = \alpha^n - \frac{\Delta t}{2V} \sum_{s=0}^{N-1} (\vec{A}_s \cdot \vec{V}_i^n) (\alpha_{s,0}^n + \alpha_{s,1}^n) - \frac{\Delta t}{2V} \sum_{s=0}^{N-1} A_s \hat{S}_s^n (\alpha_{s,0}^n - \alpha_{s,1}^n) \quad (3.28)$$

The equations 3.27 and 3.28 are multidimensional counterparts of one dimensional results in reference [42].

### 3.1.1.4 Godunov-HLL Scheme

The numerical flux of HLL approximate Riemann solver is

$$F_{HLL} = \frac{\hat{S}_{s,1} \hat{F}_{s,0} - \hat{S}_{s,0} \hat{F}_{s,1} + \hat{S}_{s,0} \hat{S}_{s,1} (\hat{U}_{s,1} - \hat{U}_{s,0})}{\hat{S}_{s,1} - \hat{S}_{s,0}} \quad (3.29)$$

where indexes 1 and 0 refers to right and left states respectively.

Following the same procedure of previous section the non-conservative terms are found as,

$$\frac{\partial \alpha}{\partial x} = \frac{1}{V} \sum_{s=0}^{N-1} A_s \cos(\theta_s) \frac{\hat{S}_{s,1} \alpha_{s,0} - \hat{S}_{s,0} \alpha_{s,1}}{\hat{S}_{s,1} - \hat{S}_{s,0}} \quad (3.30)$$

$$\frac{\partial \alpha}{\partial y} = \frac{1}{V} \sum_{s=0}^{N-1} A_s \sin(\theta_s) \frac{\hat{S}_{s,1} \alpha_{s,0} - \hat{S}_{s,0} \alpha_{s,1}}{\hat{S}_{s,1} - \hat{S}_{s,0}} \quad (3.31)$$

Above equations can be written in a more generic vector form (gradient of  $\alpha$ ) as,

$$\nabla \alpha = \frac{1}{V} \sum_{s=0}^{N-1} \vec{A}_s \frac{\hat{S}_{s,1} \alpha_{s,0} - \hat{S}_{s,0} \alpha_{s,1}}{\hat{S}_{s,1} - \hat{S}_{s,0}} \quad (3.32)$$

Equation 3.32 gives the scheme to discretize the non-conservative source terms for HLL flux function.

Similarly the solution method for volume fraction equation is found,

$$\alpha^{n+1} = \alpha^n - \frac{\Delta t}{V} \sum_{s=0}^{N-1} \vec{A}_s \cdot \vec{V}_i^n \frac{(\hat{S}_{s,1}^n \alpha_{s,0}^n - \hat{S}_{s,0}^n \alpha_{s,1}^n)}{\hat{S}_{s,1}^n - \hat{S}_{s,0}^n} - \frac{\Delta t}{V} \sum_{s=0}^{N-1} A_s \frac{(\alpha_{s,1}^n - \alpha_{s,0}^n) \hat{S}_{s,0}^n \hat{S}_{s,1}^n}{\hat{S}_{s,1}^n - \hat{S}_{s,0}^n} \quad (3.33)$$

Equation 3.33 gives the required scheme to solve the non-conservative volume fraction equation in 3.1 along with the HLL flux function. The second term at the right hand side of the Eq. 3.33 is the convective term. Third term at the right hand side is the viscosity term.

### 3.2 Velocity Relaxation Procedure For Interface Problems

The velocity relaxation terms for multi-phase mixtures are given in section 5.1 in terms drag forces between particles and the main phase. These drag force terms are written in the form given below;

$$F_d^j = \sum_{i=1}^N \lambda_{ij} (u_i - u_j) \quad (3.34)$$

where the velocity relaxation coefficient  $\lambda$  is a function of local flow variables and topology. This coefficient is usually a finite value characterizing the drag forces between a main phase and particle phases.

For a multi fluid problem including interfaces separating two pure fluids, an approach similar to the one for multi-phase mixtures is not possible. Physically the interface condition imposes velocity equality at the interface. An instantaneous velocity relaxation is required to satisfy this condition. For an instantaneous relaxation, the coefficient  $\lambda$  in equation 3.34 tends to infinity. Velocity relaxation procedure requires the solution of following ODE system when  $\lambda_{ji} \rightarrow \infty$  for all  $j = 1, \dots, N$  and  $i = 1, \dots, N$ .

$$\frac{\partial U_i}{\partial t} = \begin{pmatrix} 0 \\ 0 \\ \sum_{j=1}^N \lambda_{ij} (u_j - u_i) \\ \sum_{j=1}^N V_I \lambda_{ij} (u_j - u_i) \end{pmatrix} \quad (3.35)$$

For simplicity a one dimensional interface problem separating two different phases is considered. In this case the ODE in equation 3.35 is written as,

$$\frac{\partial \alpha_i}{\partial t} = 0 \quad (3.36)$$

$$\frac{\partial \alpha_i \rho_i}{\partial t} = 0 \quad (3.37)$$

$$\frac{\partial \alpha_i \rho_i u_i}{\partial t} = \lambda (u_j - u_i) \quad (3.38)$$

$$\frac{\partial \alpha_i \rho_i E_i}{\partial t} = \lambda V_I (u_j - u_i) \quad (3.39)$$

$$\frac{\partial \alpha_j \rho_j}{\partial t} = 0 \quad (3.40)$$

$$\frac{\partial \alpha_j \rho_j u_j}{\partial t} = \lambda (u_i - u_j) \quad (3.41)$$

$$\frac{\partial \alpha_j \rho_j E_j}{\partial t} = \lambda V_I (u_i - u_j) \quad (3.42)$$

The procedure for the solution of above ODE system for  $\lambda \rightarrow \infty$  is given in references [42, 29]. The value  $\alpha\rho$  is constant during relaxation, which can be seen from equations (3.37) and (3.40). The value  $\alpha\rho$  is constant during relaxation, which can be seen from equations (3.37) and (3.40). Using equations 3.37, 3.38, 3.40 and 3.41,

$$\frac{\partial u_i}{\partial t} = \frac{\lambda}{\alpha_i \rho_i} (u_j - u_i) \quad (3.43)$$

$$\frac{\partial u_j}{\partial t} = \frac{\lambda}{\alpha_j \rho_j} (u_i - u_j) \quad (3.44)$$

Subtracting equation 3.43 from equation 3.44 and integrating results

$$u_j - u_i = (u_{j0} - u_{i0}) \exp \left[ -\lambda \left( \frac{1}{\alpha_i \rho_i} + \frac{1}{\alpha_j \rho_j} \right) \right] \quad (3.45)$$

where  $u_{j0}$  and  $u_{i0}$  are initial values before velocity relaxation process. When  $\lambda$  tends to infinity, equation 3.45 becomes

$$u_j - u_i = 0 \quad (3.46)$$

Summing equations 3.43 and 3.44 gives

$$\alpha_i \rho_i \frac{\partial u_i}{\partial t} + \alpha_j \rho_j \frac{\partial u_j}{\partial t} = 0 \quad (3.47)$$

Integration of equation 3.46 gives

$$\alpha_i \rho_i (u_i - u_{i0}) + \alpha_j \rho_j (u_j - u_{j0}) = 0 \quad (3.48)$$

Using equations 3.45 and 3.46

$$u_i = u_j = \frac{\alpha_i \rho_i u_{i0} + \alpha_j \rho_j u_{j0}}{\alpha_i \rho_i + \alpha_j \rho_j} \quad (3.49)$$

This result can be generalized for  $N$  phases for  $N \geq 2$ ,

$$u = u_1 = \dots = u_N = \frac{\sum_{k=1}^N \alpha_k \rho_k u_{k0}}{\sum_{k=1}^N \alpha_k \rho_k} \quad (3.50)$$

Above equation shows that all the relaxed velocities at the interface are equal to the interface velocity given in equation 3.4. This result justifies the choice of inter-facial velocity formulation.

### 3.3 Pressure Relaxation

When the fluids in a multi fluid system are in a non-equilibrium pressure state (such as after a wave propagation) ( $P_j \neq P_i$  for  $j \neq i$ ), a pressure relaxation process develops and the pressure tends to equilibrium, ( $P_I = P_1 = P_2 = \dots = P_N$ ) [42]. For most interface problems, the time scale for the pressure relaxation process is very small compared to other processes such as the velocity drag and thermal relaxation processes [29, 30, 42]. Pressure relaxation process leads to pressure equilibrium at the phasic interface almost instantaneously for most compressible multi-fluid systems. For a system with instantaneous velocity relaxation, an instantaneous pressure relaxation leading to pressure equilibrium is very natural and necessary [29, 30].

The ODE system describing the pressure relaxation process is defined as;

$$\frac{\partial \alpha_j}{\partial t} = \sum_l^N \mu_{jl} (P_j - P_l) \quad (3.51)$$

$$\frac{\partial \alpha_j \rho_j}{\partial t} = 0 \quad (3.52)$$

$$\frac{\partial \alpha_j \rho_j u_j}{\partial t} = 0 \quad (3.53)$$

$$\frac{\partial \alpha_j \rho_j E_j}{\partial t} = -P_I \sum_l^N \mu_{jl} (P_j - P_l) \quad (3.54)$$

Above equations can also be written in a form consistent with equation 3.11 and 3.12 as given below,

$$\frac{\partial U_j}{\partial t} = \begin{pmatrix} \sum_l^N \mu_{jl} (P_j - P_l) \\ 0 \\ 0 \\ -P_l \sum_l^N \mu_{jl} (P_j - P_l) \end{pmatrix}, \quad \text{for all } j = 1, \dots, N \quad (3.55)$$

The homogenization parameter (dynamic compaction viscosity)  $\mu_{ji}$  controls the rate at which pressure tends to equilibrium [4]. For instantaneous pressure relaxation the homogenization parameter  $\mu_{ji}$  tends to infinity.

Both partial density  $\alpha\rho_j$  and velocity  $u_j$  remain constant during pressure relaxation process. This can be deduced from equations 3.52 and 3.53. Equation 3.53 is expanded to see that,

$$\alpha_j \rho_j \frac{\partial u_j}{\partial t} + u_j \frac{\partial \alpha_j \rho_j}{\partial t} = 0 \quad (3.56)$$

Using equation 3.52 we deduce  $\frac{\partial u_j}{\partial t} = 0$ . This result is physical because pressure relaxation is a result of internal pressure forces which can not lead to a net momentum change. Using equations 3.51 and 3.54, following can be written,

$$\frac{\partial \alpha_j \rho_j E_j}{\partial t} = -P_l \frac{\alpha_j}{\partial t} \quad (3.57)$$

Denoting the initial and final times of the pressure relaxation process by  $t^0$  and  $t^*$  respectively, the assumption below can be safely made.

$$t^* - t^0 \ll \Delta t \quad (3.58)$$

where  $\Delta t$  is the time step size used for the solution of the transport part of the multi-fluid system.

Again using equations 3.52 and 3.53, the equation 3.57 is rewritten as

$$\alpha_j \rho_j \frac{\partial e}{\partial t} = -P_I \frac{\partial \alpha_j}{\partial t} \quad (3.59)$$

It was shown above that the value  $\alpha_j \rho_j$  is constant during pressure relaxation. Integrating equation 3.59,

$$\alpha_j \rho_j (e^* - e^0) = - \int_{t^0}^{t^*} P_I \frac{\partial \alpha_j}{\partial t} dt \quad \text{for all } j = 1, \dots, N \quad (3.60)$$

By using the change of variables  $d\alpha_j = \frac{\partial \alpha_j}{\partial t} dt$ ,

$$\alpha_j \rho_j (e^* - e^0) = - \int_{\alpha_j^0}^{\alpha_j^*} P_I d\alpha_j \quad \text{for all } j = 1, \dots, N \quad (3.61)$$

Equation 3.61 can be rewritten in differential form as [29];

$$\alpha_j \rho_j = -P_I d\alpha_j \quad \text{for all } j = 1, \dots, N \quad (3.62)$$

The differential terms  $de_j$  and  $d\alpha_j$  can be written in different forms. Since  $\alpha_j \rho_j$  is constant during process,

$$d\alpha_j = d\left(\frac{\alpha_j \rho_j}{\rho_j}\right) = -\frac{\alpha_j \rho_j}{\rho_j^2} d\rho_j \quad \text{for all } j = 1, \dots, N \quad (3.63)$$

then

$$de_j = -\frac{P_I}{\alpha_j \rho_j} = \frac{P_I}{\rho_j^2} d\rho_j \quad \text{for all } j = 1, \dots, N \quad (3.64)$$

$de_j$  can also be written using equation of state of the form  $e_j = e_j(\rho_j, P_j)$

$$de_j = \left. \frac{\partial e_j}{\partial \rho_j} \right|_{P_j} d\rho_j + \left. \frac{\partial e_j}{\partial P_j} \right|_{\rho_j} dP_j \quad \text{for all } j = 1, \dots, N \quad (3.65)$$

Again using the fact that  $\alpha_j \rho_j$  is constant during pressure relaxation,

$$d\rho_j = d\left(\frac{\alpha_j \rho_j}{\alpha_j}\right) = -\frac{\alpha_j \rho_j}{\alpha_j^2} d\alpha_j \quad \text{for all } j = 1, \dots, N \quad (3.66)$$

Then

$$de_j = -\frac{\alpha_j \rho_j}{\alpha_j^2} \left. \frac{\partial e_j}{\partial \rho_j} \right|_{P_j} d\alpha_j + \left. \frac{\partial e_j}{\partial P_j} \right|_{\rho_j} dP_j \quad \text{for all } j = 1, \dots, N \quad (3.67)$$

Using the definition of  $j$ th phase interfacial speed of sound  $c_{I,j}^2 = \frac{\left. \frac{P_j - \frac{\partial e_j}{\partial \rho_j} \right|_{P_j}}{\rho_j^2}}{\left. \frac{\partial e_j}{\partial P_j} \right|_{\rho_j}}$  and equations 3.66, 3.67

$$dP_j = -\frac{\alpha_j \rho_j}{\alpha_j^2} c_{I,j}^2 d\alpha_j \quad \text{for all } j = 1, \dots, N \quad (3.68)$$

Integration of equation 3.68 leads to an equation equivalent to 3.61,

$$P_j^* - P_j^0 = - \int_{\alpha_j^0}^{\alpha_j^*} \frac{\alpha_j \rho_j c_{I,j}^2}{\alpha_j^2} d\alpha_j \quad \text{for all } j = 1, \dots, N \quad (3.69)$$

where  $P_j^*$  is the final pressure after relaxation process and  $P_j^0$  is the initial pressure before pressure relaxation process.

Equations 3.61 and 3.69 can be integrated to give final values  $e_j^*$  or  $P_j^*$ . Some other different efficient procedures and this one is explained in references [29, 30].

### 3.3.1 Solution Procedure

The details of the procedure can be found in reference [29]. The integral of the right hand side of equation 3.69 can be approximated as

$$P_j^* - P_j^0 = - \left( \frac{\alpha_j \rho_j c_{I,j}^2}{\alpha_j^2} \right)^0 \Delta \alpha_j^* \quad \text{for all } j = 1, \dots, N \quad (3.70)$$

If relaxation is reached, the following should hold

$$P_l^* = P_j^* = P_m^* \quad \text{for all } j, m = 1, \dots, N \quad (3.71)$$

or

$$P_l^* = P_j^* = P_1^* \quad \text{for all } j = 2, \dots, N \quad (3.72)$$

Using 3.70

$$P_j^0 - a_j^0 \Delta \alpha_j^* = P_1^0 - a_1^0 \Delta \alpha_1^* \quad (3.73)$$

where  $a_j = \frac{\alpha_j \rho c_{L,j}}{\alpha_j^2}$

Using the saturation condition  $\sum_{j=1}^N \Delta \alpha_j^* = 0$

$$\Delta \alpha_1^* = - \sum_{j=2}^N \Delta \alpha_j^* \quad (3.74)$$

From equations 3.73 and 3.74

$$\Delta \alpha_1^* = \frac{\sum_{j=2}^N \frac{(P_1^0 - P_j^0)}{a_j}}{\sum_{j=1}^N \frac{a_1}{a_j}} \quad (3.75)$$

Using equations 3.73 and 3.75 all volume fractions after relaxation can be calculated. However admissibility of these values should be verified. Volume fractions are admissible if  $0 \leq \alpha_j^* \leq 1$  for all  $j = 1, \dots, N$ . This condition can also be written as,

$$- \alpha_1^0 \leq \Delta \alpha_j^* \leq 1 - \alpha_j^0 \quad (3.76)$$

Using equation 3.73

$$- \alpha_1^0 \leq \frac{P_j^0 - P_1^0 + a_1^0 \Delta \alpha_1^*}{a_j^0} \leq 1 - \alpha_j^0 \quad (3.77)$$

or in a more useful form [29]

$$\max_j \left\{ -\frac{P_j^0 - P_1^0 + a_j^0 \alpha_j^0}{a_1^0} \right\} \leq \Delta \alpha_1^* \leq \min_j \left\{ -\frac{P_j^0 - P_1^0 + a_j^0 (1 - \alpha_j^0)}{a_1^0} \right\} \quad (3.78)$$

## CHAPTER 4

### DISCRETE APPROACH FOR COMPRESSIBLE MULTI-PHASE FLOWS

In Chapter 3, the method given in reference [42] was extended to unstructured grids. This method with proper handling of non-conservative terms and relaxation procedures was able to solve equations 3.1. However, although the missing data problem due to missing waves across the material interfaces was overcome by relaxation procedures, the method is not robust in some conditions. This issue can be explained by considering the method's approach for the wave structure at a material interface. In this method the only way to define an interface is to use very small volume fractions of the different phases at each side of the interface. The information across the interface is carried between the same phases then the information is propagated to the other phases by relaxation procedures. In this way the missing waves are recovered. However because the phase with a very small volume fraction such as  $10^{-6}$  is first to get the whole information, the method is very prone to numerical difficulties related to the limits of EOS formulations used for this phase. This problem becomes important for shock waves across the material interfaces.

In fact the problem with this method originates from the equation system solved. This equation system is a pure Eulerian multi-phase model describing each phase as a continuum without a material discontinuity such as a phasic interface. In principle the difficulty can be overcome by approaching the problem at a more basic level. Discrete equations can be produced at material interfaces to supply a Godunov method with required numerical fluxes averaged over the cell faces. Abgrall and Saurell [2] used this approach to overcome the problems existing in their previous study [42]. With

Discrete Equations Method they were also able to solve non-conservative products that appear in seven equations model studied in chapter 3. In this chapter I propose a similar but more simple and effective approach for constructing a Godunov scheme by adapting HLLC flux for phasic interfaces. The proposed method can be applied to both multi-fluid and multi-phase mixtures without any modification.

#### 4.1 Wave Patterns in a multi-phase Mixture

In a multi-phase mixture approach, an interface separating two pure materials is not defined. The averaged equations define such a mixture. However, it is still possible to define material interfaces by defining mixtures containing negligible amounts of the other phases on each side [42]. For example to define a pure liquid phase the volume fraction of the liquid can be initialized as  $\alpha_l = 1 - \epsilon$ , where  $\epsilon$  is equal to a very small value such as  $10^{-8}$ . A typical wave configuration of a Riemann problem solution for such a mixture defined by an averaged equation system is shown schematically in Fig. 4.1. In fact the configuration in Fig.4.1 depicts the states before the velocity and pressure relaxation procedures. Since the solution of the Riemann problem is realized after velocity and pressure relaxations, the possible number of wave configurations is equal to that of single phase problems. This property furnishes one to utilize single phase Riemann solvers for the problem.

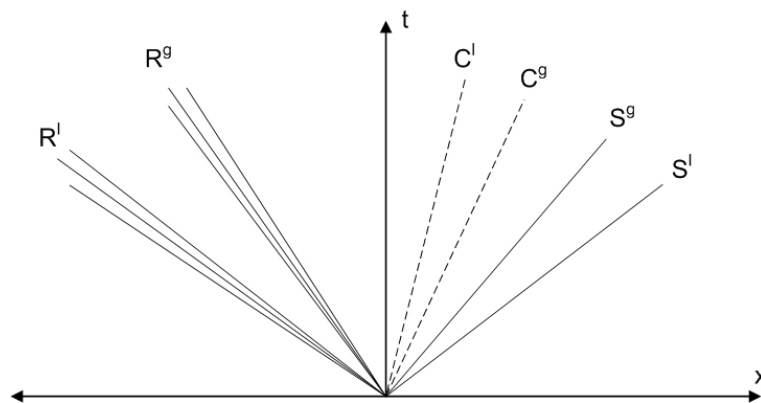


Figure 4.1: Rarefaction (R), contact (C) and shock (S) wave pattern in a compressible two phase mixture. Superscripts l and g denote liquid and gas phases respectively.

## 4.2 Wave Patterns at an Interface Separating Two Pure Fluids

A possible Riemann problem solution for an interface initially separating two pure fluids is depicted in Fig. 4.2. It is evident from the figure that the two fluids remain on two sides of the contact wave which corresponds to the interface moving to the right. The possible wave configurations are again the same as those of the single phase problem. Therefore, these type problems can be solved by utilizing any explicit method in conjunction with an interface tracking method. HLLC type Riemann solvers are especially advantageous in these type of problems due to exact resolution of the contact waves.

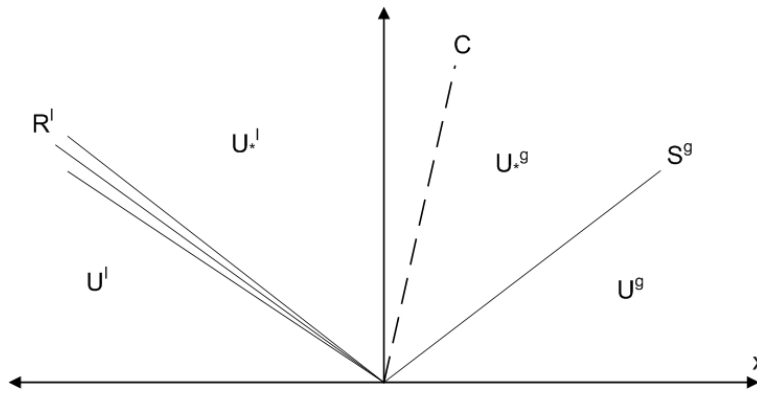


Figure 4.2: Rarefaction (R), contact (C) and shock (S) wave pattern at an interface. Superscripts l and g denote liquid and gas phases respectively.

## 4.3 Definitions and Assumptions

The numerical scheme is a finite volume method and hence the computational domain consists of discretized control volumes (cells)  $\Omega_c$ . Each pure fluid in a discrete control volume is governed by the Euler equations. For each pure fluid  $\Sigma_i$ , the flow states and associated fluxes are given as below:

$$U^i = \begin{bmatrix} \rho^i \\ \rho^i u^i \\ \rho^i v^i \\ \rho^i E^i \end{bmatrix}, \quad F^i = \begin{bmatrix} \rho^i u^i \\ \rho^i u^{i2} + P^i \\ \rho^i u^i v^i \\ u^i(\rho^i E^i + P^i) \end{bmatrix}, \quad G^i = \begin{bmatrix} \rho^i v^i \\ \rho^i u^i v^i \\ \rho^i v^{i2} + P^i \\ v^i(\rho^i E^i + P^i) \end{bmatrix} \quad (4.1)$$

For a Godunov type finite volume method one needs to represent cell averaged fluid states for each control volume. This can be done by an averaging procedure as in [13] and [2]. A characteristic function  $X^i$  is introduced for this purpose.  $X^i$  is defined as  $X^i(\vec{x}, t) = 1$  if  $\vec{x}$  lies in fluid  $\Sigma_i$ , otherwise 0. An average state  $W_c^i$  for phase  $\Sigma_i$  is defined as,

$$W_c^i = \frac{1}{V_{\Omega_c}} \int_{\Omega_c} X^i U^i d\vec{x} \quad (4.2)$$

where  $V_{\Omega_c}$  is the volume of the solution cell. The result of this averaging procedure can be written in terms of volume fractions  $\alpha_i$  as,

$$W_c^i = \begin{bmatrix} \alpha^i \rho^i \\ \alpha^i \rho^i u^i \\ \alpha^i \rho^i v^i \\ \alpha^i \rho^i E^i \end{bmatrix}, \quad (4.3)$$

For a multi-phase mixture and multi-fluid problem with definite interfaces the velocities  $u^i$  and  $v^i$  and pressures  $P^i$  of each phase become equal after relaxation procedures as defined in Section 3.2. When one or more phases are in the form of particles, phase velocities may be different. In this case, the right side of the Eq. (3.35) is usually written in the form of momentum transfer terms.

There may be interfaces in the cells. The total interfacial area in a cell volume is not known nor correlated to volume fractions except particulate phases. Thus, interface is tracked by a diffuse interface approach.

Interfacial areas of phases at cell faces are correlated to volume fractions and this

feature will be used to calculate Godunov fluxes across the cell faces for each phase  $\Sigma_i$ . There may be many interface configurations at the cell faces, and therefore, it is assumed that phase interfaces are randomly positioned at a cell face. This situation is illustrated in Fig. 4.3.

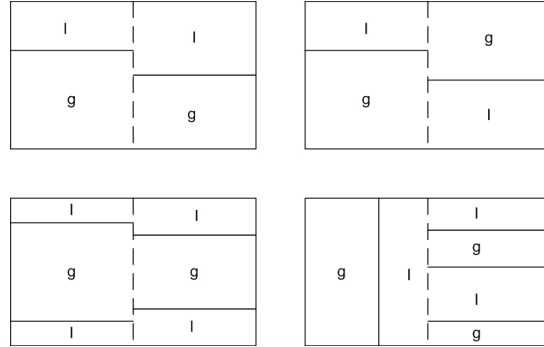


Figure 4.3: Some of possible phase interface configurations at cell face.

### 4.3.1 Riemann Problem at a Cell Face

The Riemann problem for a cell face with multiple phase interfaces can be defined with initial condition at  $t = 0$  as described by

$$U^i = \begin{cases} U_L^i & \text{if } x \leq 0 \\ U_R^i & \text{if } x \geq 0 \end{cases} \quad (4.4)$$

$$P_L^i = P_L^1, \quad u_L^i = u_L^1, \quad i = 2, \dots, N$$

$$P_R^i = P_R^1, \quad u_R^i = u_R^1, \quad i = 2, \dots, N$$

The equilibrium states of phase pressures  $P^i$  and phase velocities  $u^i$  defined in Eq. 4.4 is justified by assuming micro scale relaxation processes are completed before time  $t = 0$ . A possible way of solving this shock tube type problem is to temporarily ignore relaxation processes for a sufficiently short time after  $t = 0$ . This situation is illustrated for a possible interface configuration in Fig. 4.4. Actually, rather than ignoring the relaxation processes for a short time, one can suggest to use a well known method "time splitting". Time splitting is more generally used in explicit methods

for updating source terms. However, micro scale pressure and velocity relaxation processes on a phase interface are completed almost infinitely fast compared to other processes. This is in contrast to source terms such as momentum and heat transfer which are time dependent processes.

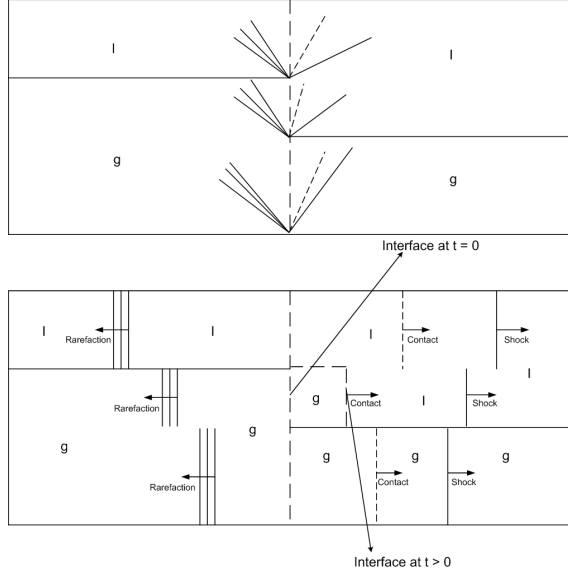


Figure 4.4: Wave and phase patterns ignoring relaxation processes at a short time after  $t = 0$ .

#### 4.4 Solution of Riemann Problem By Utilizing HLLC Solver

For a Godunov type solution for phase  $\Sigma_i$ , one needs to calculate fluxes for all possible interface and wave configurations. It is assumed that all the  $N$  phases present on each side of the cell face and phasic interfaces may have all possible random configurations at the cell face. Defining  $(\Sigma_i, \Sigma_j)$  as one type of possible interfaces which separates the phase  $\Sigma_i$  on left and the phase  $\Sigma_j$  on right, we can calculate the number for all possible interface configurations including phase  $\Sigma_i$ . This number for phasic interfaces turns out to be  $2N - 1$ . These possible interfaces for phase  $\Sigma_i$  is categorized in three general groups:

1.  $(\Sigma_i, \Sigma_i)$
2.  $(\Sigma_i, \Sigma_j), \quad i \neq j$

3.  $(\Sigma_j, \Sigma_i)$ ,  $j \neq i$

In the following sections, Godunov fluxes are calculated for each possible interface configuration with each possible wave pattern for phase  $\Sigma_i$ . It is assumed that the fluxes are calculated for the left cell  $\Omega_L$  which is on the negative side of the  $\hat{x}$  axis on the local, rotated coordinate system (coordinate rotation methods for non-Cartesian domains was reviewed in [48]).

#### 4.4.1 $(\Sigma_i, \Sigma_i)$ Interface

Since this interface defines a single phase problem, the flux  $F^i(\Sigma_i, \Sigma_i)$  across this interface can be calculated with the HLLC solver without any modification. In the following equations  $(i, j)$  is used in superscripts instead of  $(\Sigma_i, \Sigma_j)$ .

$$F^i(U_L^i, U_R^i) = \begin{cases} F_L^i & \text{if } 0 \leq S_L^{(i,i)} \\ F_L^i + S_L^{(i,i)}(U_{*L}^{(i,i)} - U_L^i) & \text{if } S_L^{(i,i)} \leq 0 \leq S_*^{(i,i)}, \\ F_R^i + S_R^{(i,i)}(U_{*R}^{(i,i)} - U_R^i) & \text{if } S_*^{(i,i)} \leq 0 \leq S_R^{(i,i)}, \\ F_R^i & \text{if } 0 \geq S_R^{(i,i)} \end{cases} \quad (4.5)$$

Where  $S_L$  are  $S_R$  are left and right wave velocities respectively.  $S_*$  is the contact wave velocity which is also the advection velocity of the phase interface information. The subscript  $*L$  denotes the region between left wave and contact wave. Similarly the subscript  $*R$  denotes the region between the right wave and the contact wave. The volume fraction  $\alpha^i$  of the phase  $\Sigma_i$  is not affected by the processes on the interface  $(\Sigma_i, \Sigma_i)$  before any relaxation processes in the cell. Therefore, the flux  $F_{\alpha^i}^{(i,i)}$  carrying information for volume fraction of phase  $\alpha^i$  is zero across any single phase interface.

#### 4.4.2 $(\Sigma_i, \Sigma_j)$ , $i \neq j$ Interface

For this type interface there are two different situations according to the direction of the contact wave which carries the interface position. For a right going contact wave, the HLLC formulation is still valid for phase  $\Sigma_i$ . However, for a left going contact

wave there is no information carried by convective terms for phase  $\Sigma_i$ . This flux can be simply defined, in two dimensions, as

$$F^{(i,j),i \neq j}(U_L^i, U_R^j) = \begin{bmatrix} 0 \\ P_*^{(i,j)} \\ 0 \\ u_*^{(i,j)} P_*^{(i,j)} \end{bmatrix} \quad \text{if } S_*^{(i,j)} \leq 0 \quad (4.6)$$

One can also reach this result (Eq.(4.6)) by using the HLLC Riemann solver. The flux on the right of the contact wave can be written, using the HLLC solution of the Riemann problem [48], as

$$F_{*R}^{(i,j)} = F_{*L}^{(i,j)} + S_*^{(i,j)} (U_{*R}^{(i,j)} - U_{*L}^{(i,j)}) \quad (4.7)$$

Subtracting the convective part  $S_*^{(i,j)} U_{*R}^{(i,j)}$  from  $F_{*R}^{(i,j)}$ , we find

$$F^{(i,j),i \neq j}(U_L^i, U_R^j) = F_{*L}^{(i,j)} - S_*^{(i,j)} U_{*L}^{(i,j)}, \quad \text{if } S_*^{(i,j)} \leq 0 \quad (4.8)$$

This result is consistent with the formulation used in [2]. The HLLC flux for the interface  $(\Sigma_i, \Sigma_j)$ ,  $i \neq j$  is written as

$$F^{(i,j),i \neq j}(U_L^i, U_R^j) = \begin{cases} F_L^i & \text{if } 0 \leq S_L^{(i,j)} \\ F_L^i + S_L^{(i,j)} (U_{*L}^{(i,j)} - U_L^i) & \text{if } S_L^{(i,j)} \leq 0 \leq S_*^{(i,j)} \\ F_{*L}^{(i,j)} - S_*^{(i,j)} U_{*L}^{(i,j)} & \text{if } S_*^{(i,j)} \leq 0 \end{cases} \quad (4.9)$$

A similar formulation can be written for volume fraction  $\alpha^i$ ,

$$F_{\alpha^i}^{(i,j),i \neq j} = \begin{cases} 0 & \text{if } S_*^{(i,j)} \geq 0 \\ -S_*^{(i,j)} & \text{if } S_*^{(i,j)} \leq 0 \end{cases} \quad (4.10)$$

#### 4.4.3 $(\Sigma_j, \Sigma_i), j \neq i$ Interface

In this case for a right going contact wave  $S_*^{(j,i)} \geq 0$ , and the flux  $F^i(U_L^i, U_R^j)$  is zero. For  $S_*^{(j,i)} \leq 0$  and  $S^{(j,i)} \geq 0$ , only convective flux of the  $*R$  region exists, which is  $S_*^{(j,i)} U_{*R}^{(j,i)}$ . For the supersonic case  $S_R^{(j,i)} \geq 0$ , again the HLLC solution can be used to find the flux for  $\Sigma_i$  on left of the interface. By subtracting the flux  $F_{*R}^{(j,i)}$  in the  $*R$  region from  $F_R^i$  and adding the convective part of the  $*R$  region, we find the net flux for phase  $\Sigma_i$  at the left cell. The HLLC solver for this interface is then written as,

$$F^{(j,i),j \neq i}(U_L^j, U_R^i) = \begin{cases} 0 & \text{if } 0 \leq S_*^{(j,i)} \\ S_*^{(j,i)} U_{*R}^{(j,i)} & \text{if } S_*^{(j,i)} \leq 0 \leq S_R^{(j,i)} \\ F_R^{(j,i)} - F_{*R}^{(j,i)} + S_*^{(j,i)} U_{*R}^{(j,i)} & \text{if } S_R^{(j,i)} \leq 0 \end{cases} \quad (4.11)$$

The flux for volume fraction  $\alpha^i$  for this interface is written as,

$$F_{\alpha^i}^{(j,i),j \neq i} = \begin{cases} 0 & \text{if } S_*^{(j,i)} \geq 0 \\ S_*^{(j,i)} & \text{if } S_*^{(j,i)} \leq 0 \end{cases} \quad (4.12)$$

#### 4.4.4 Fluxes For Godunov Method

The HLLC fluxes defined above can be used for an interface tracking method. However we use these for constructing a Godunov method with diffuse interfaces. Since the method allows the interface to be in a computational cell, velocity and pressure relaxation processes are required after updating all conserved variables. Defining  $P(\Sigma_i, \Sigma_j)$  as the probability of this interface taking place at the cell face  $\zeta_f$ .

$$P(\Sigma_i, \Sigma_j) = \frac{1}{A_{\zeta_f}} \int_{\zeta_f} X_L^i X_R^j dS = \alpha_i \alpha_j \quad (4.13)$$

Then, the Godunov flux for phase  $\Sigma_i$  is found to be,

$$F^i = \alpha_i \alpha_i F^i(U_L^i, U_R^i) + \alpha_i \alpha_j F^{(i,j),i \neq j}(U_L^i, U_R^j) + \alpha_j \alpha_i F^{(j,i),j \neq i}(U_L^j, U_R^i) \quad (4.14)$$

$$F_{\alpha}^i = \alpha^i \alpha^j F_{\alpha^i}^{(i,j),i \neq j} + \alpha^j \alpha^i F_{\alpha^i}^{(j,i),j \neq i} \quad (4.15)$$

## 4.5 Multifluid Test Cases

### 4.5.1 Water/Air Shock Tube Problem

This test problem is defined in reference [29] to test different pressure relaxation methods. A 1 m shock tube is considered, filled by high pressure liquid water at the left  $x < 0.7$  and by low pressure air at the right  $x > 0.7$ . Liquid water is modeled with a stiffened EOS, and air is ideal gas. The initial data for shock tube problem are;  $\rho^l = 10^3 \text{ kg/m}^3$ ,  $P^l = 10^9 \text{ Pa}$ ,  $u^l = 0 \text{ m/s}$ ,  $\gamma^l = 4.4$ ,  $P_{l,\infty} = 6 \times 10^8$ ,  $\alpha_L^l = 1 - 10^{-8}$  for  $x < 0.7$  and  $\rho^g = 50 \text{ kg/m}^3$ ,  $P^g = 10^5$ ,  $u^g = 0 \text{ m/s}$ ,  $\gamma^g = 1.4$ ,  $\alpha^g = 1 - 10^{-8}$  for  $x > 0.7$ .

For this test case both discrete method defined in Chapter 4 and the Godunov method described in Chapter 3 are used. Velocity and pressure relaxation methods given in Sections 3.2 and 3.3 are also applied. The solutions at time  $t = 229 \times 10^{-6}$  are given in Figures 4.5 and 4.6. These solutions are obtained with 1000 computational cells. The discrete approach provides more physical results for pressure solution and is less diffusive for volume fraction. Another problem with the continuous method is the stiffness of the solution near material interfaces especially when a powerful shock wave interacts with the interface. Due this problem CFL number should be decreased very small values in the initial times of the simulation. This numerical scheme is never stable even with CFL number of 0.5. On the other hand discrete algorithm is stable with CFL number of 2.0 when used with a four stage Runge-Kutta time advancing scheme.

### 4.5.2 Under Water Explosion

A two dimensional underwater explosion problem is considered. This problem is similar to the one previously simulated in references [26],[19] and [46]. An underwater cylindrical bubble of gaseous explosive products expands and drives the air-water interface. The details of the test problem is given in section 6.5.2. Some results can be

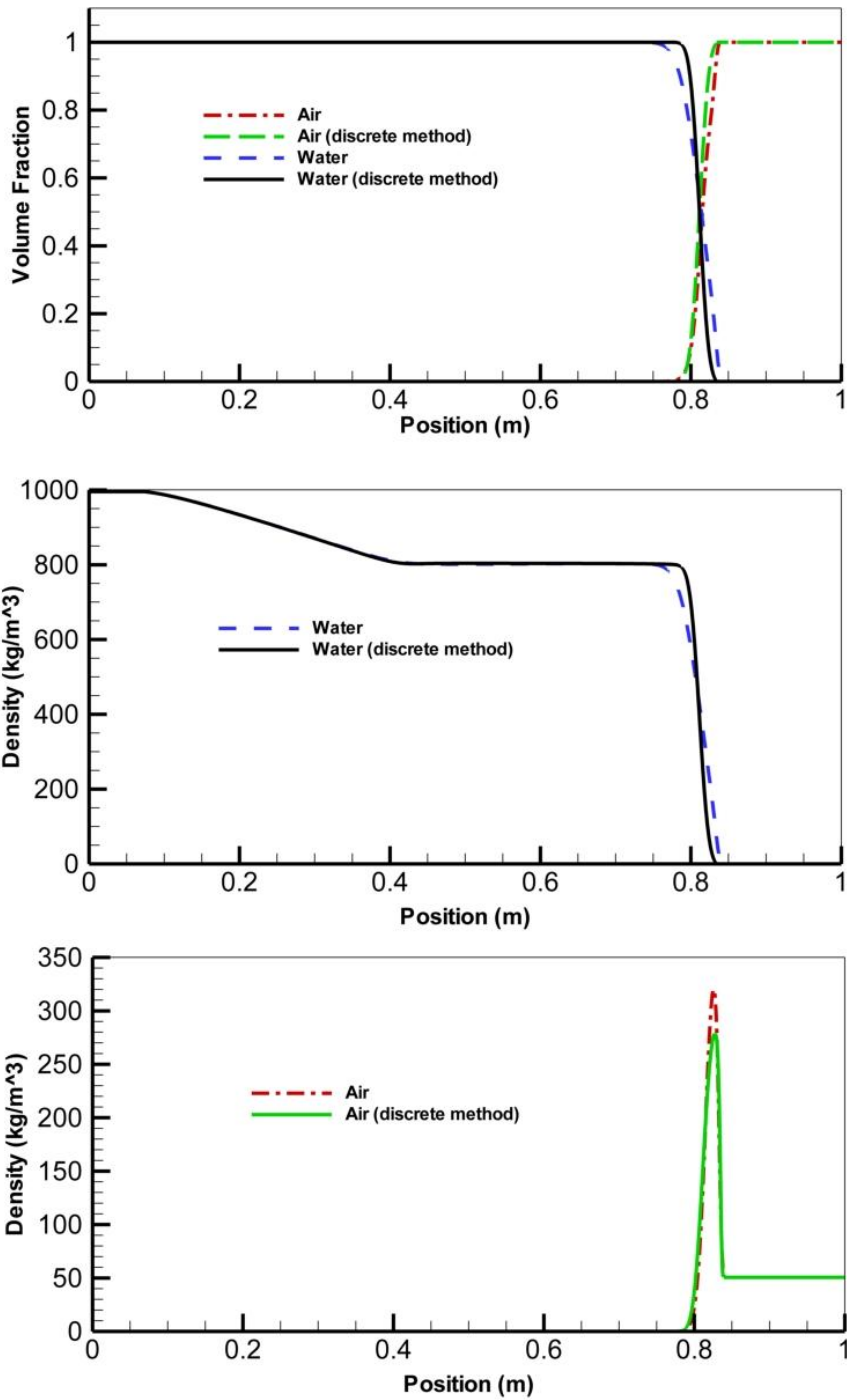


Figure 4.5: Solutions for water/air shock tube test problem at  $t = 229 \times 10^{-6}$  s.

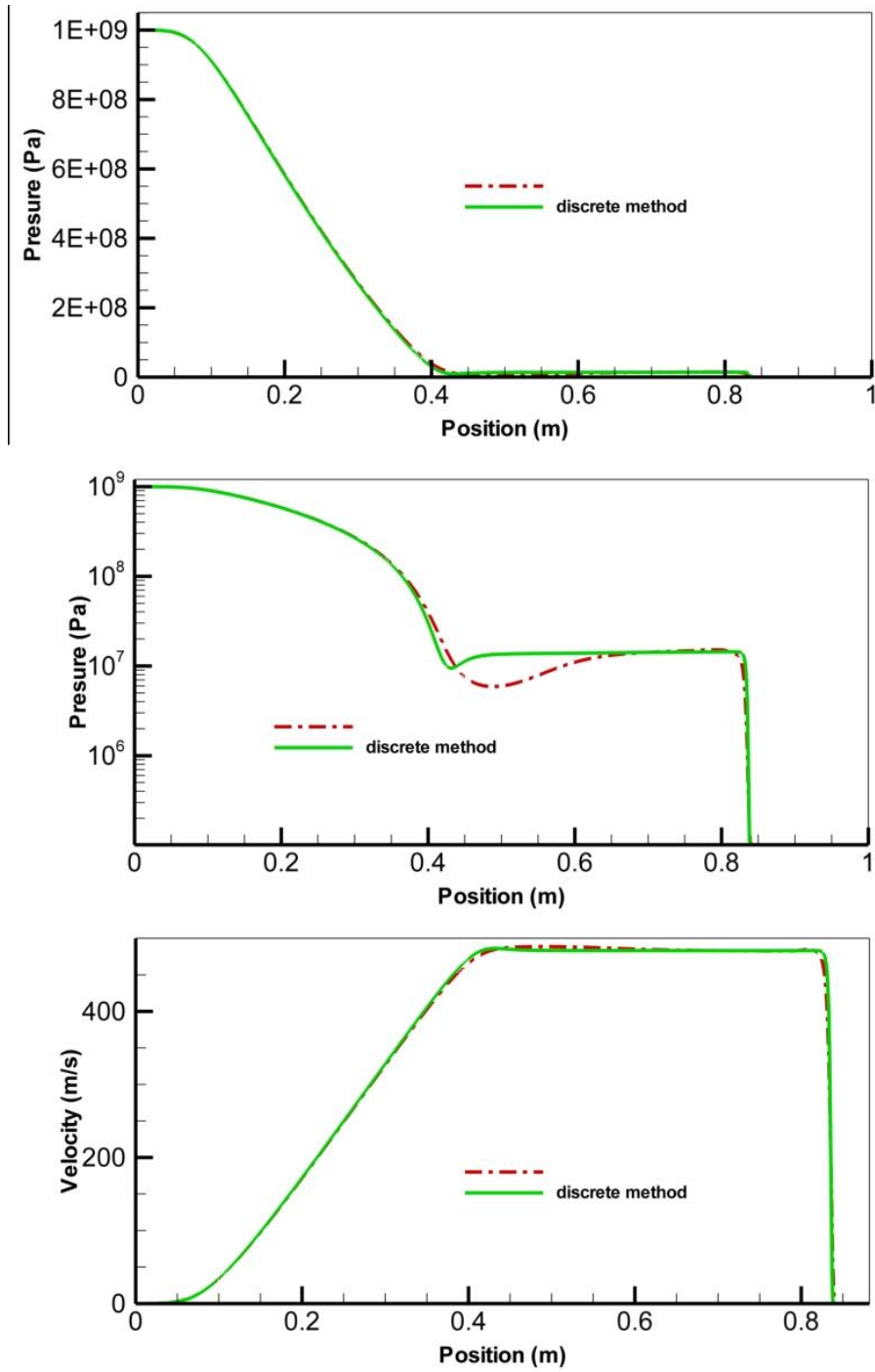


Figure 4.6: Solutions for water/air shock tube test problem at  $t = 229 \times 10^{-6}$  s.

seen in Figures 4.7, 4.8 and 4.9. As can be seen in the previous one dimensional test case in this two dimensional test case, phase interfaces are lost due to high numerical diffusion in the solution of volume fractions. Due to this diffusion, interfaces evolves to a artificial mixture region. This diffusion problem is addressed in Chapter 6.

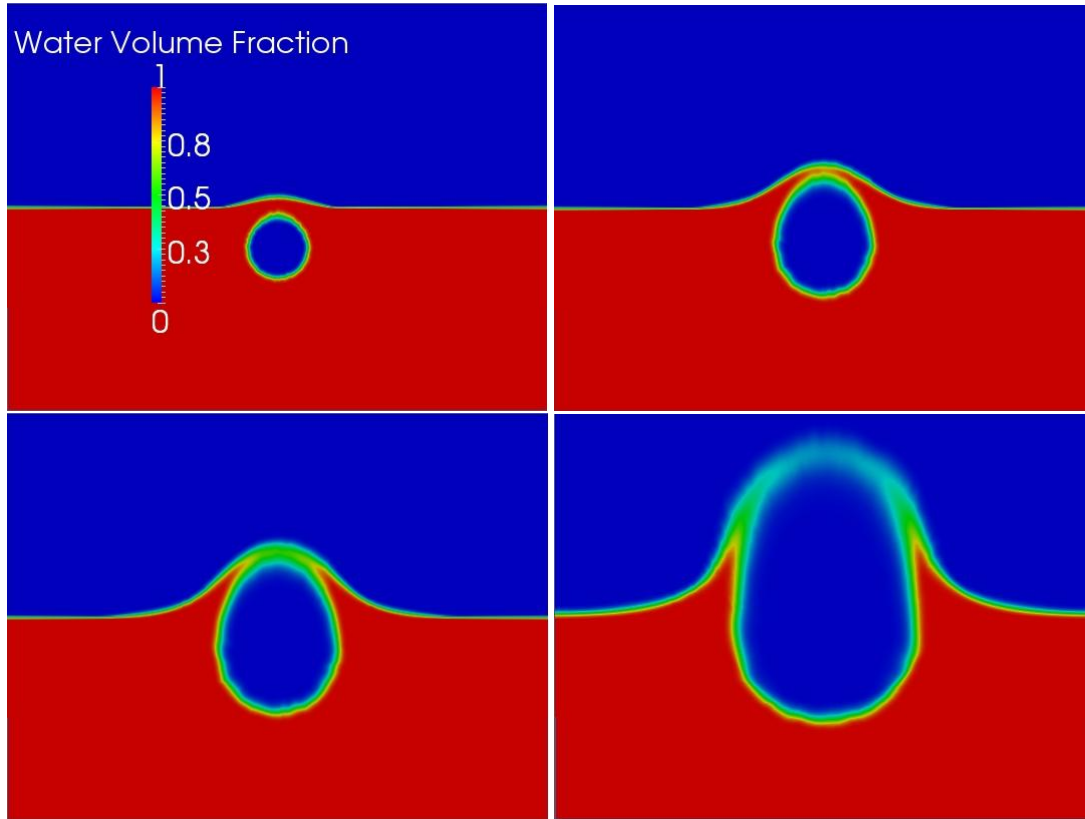


Figure 4.7: Volume fractions of water at times  $t = 100 \times 10^{-6}$ ,  $t = 240 \times 10^{-6}$ ,  $t = 340 \times 10^{-6}$  and  $t = 680 \times 10^{-6}$  seconds.

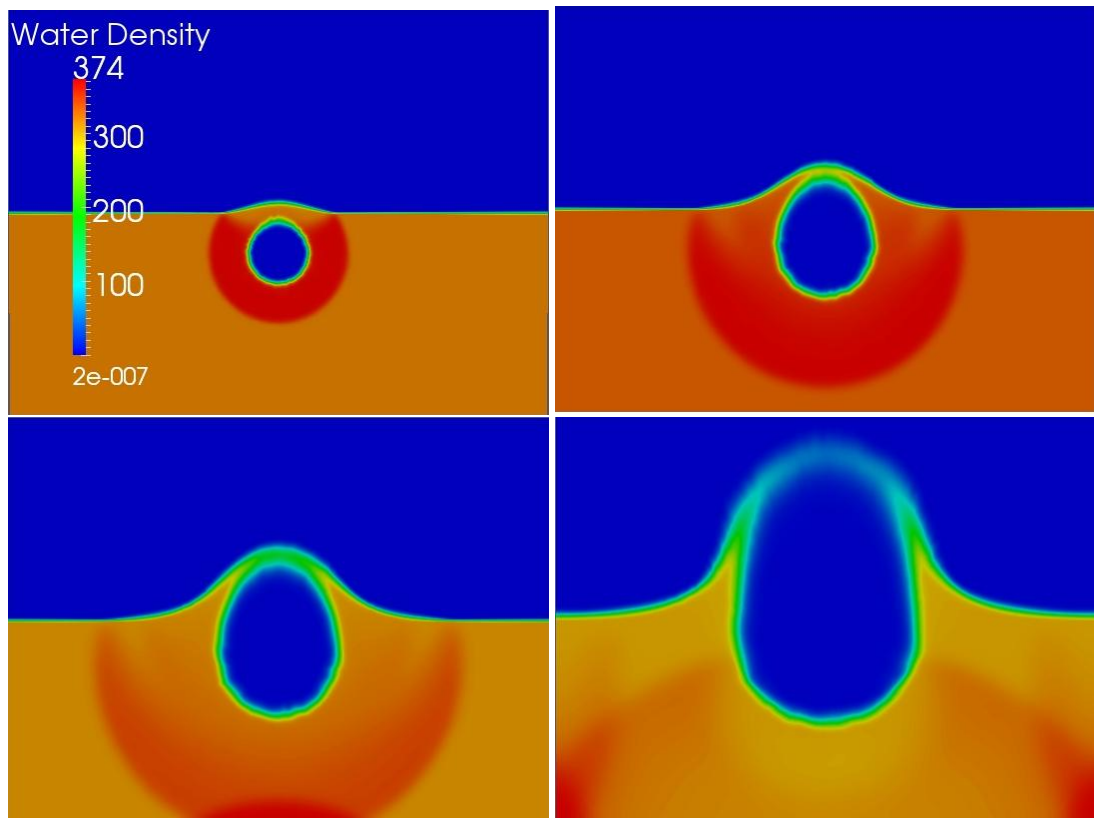


Figure 4.8: Water mixture densities at times  $t = 100 \times 10^{-6}$ ,  $t = 240 \times 10^{-6}$ ,  $t = 340 \times 10^{-6}$  and  $t = 680 \times 10^{-6}$  seconds

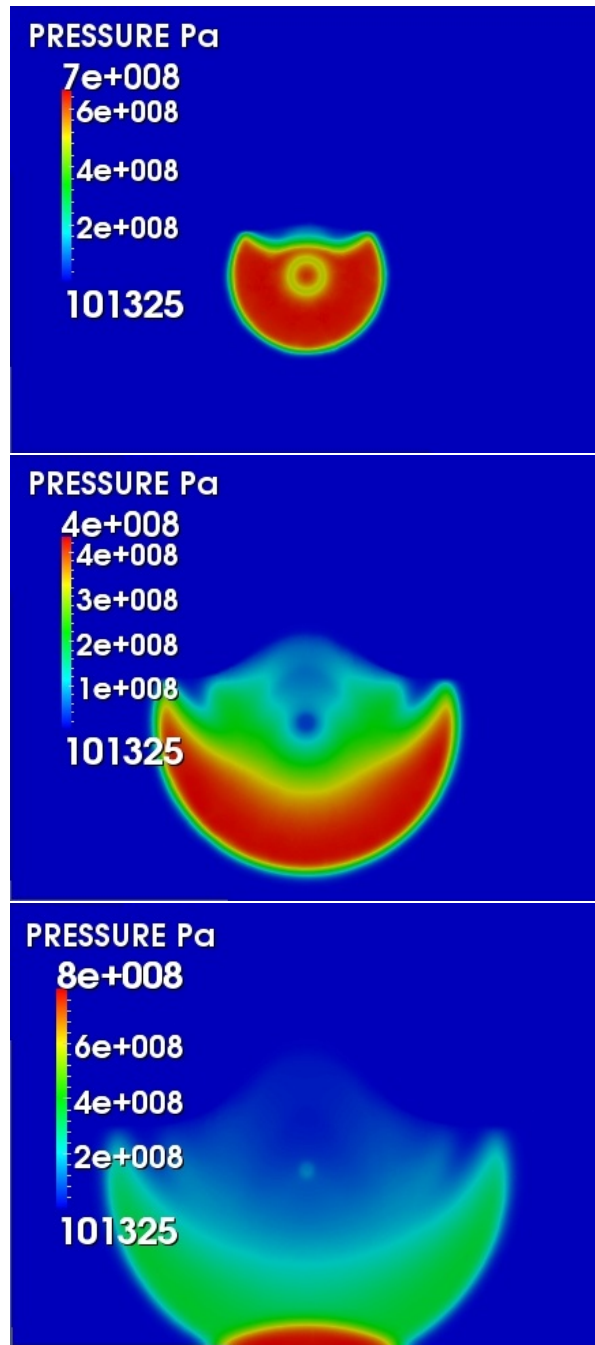


Figure 4.9: Mixture pressures at times  $t = 100 \times 10^{-6}$ ,  $t = 240 \times 10^{-6}$  and  $t = 340 \times 10^{-6}$  seconds

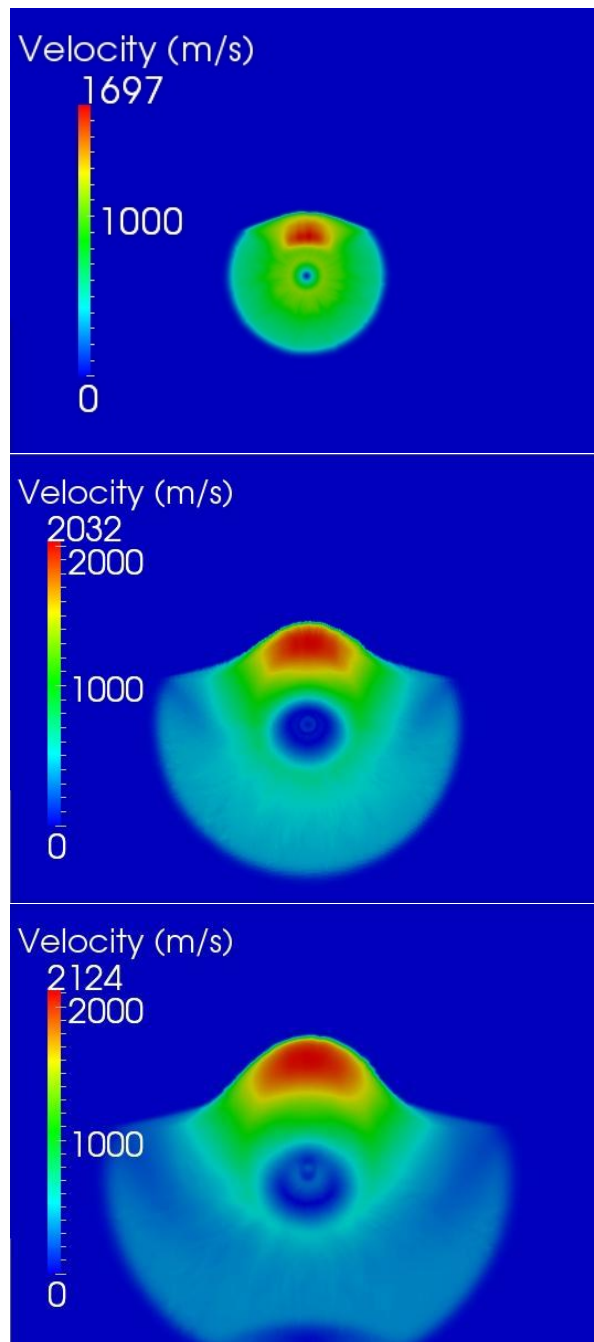


Figure 4.10: Mixture velocities at times  $t = 100 \times 10^{-6}$ ,  $t = 240 \times 10^{-6}$  and  $t = 340 \times 10^{-6}$  seconds

## CHAPTER 5

### METHODS FOR HIGHLY DILUTED MULTI-PHASE FLOWS

The methods developed in Chapters 3 and 4 provides robust solution methods for multi-phase mixture and interface problems. However these methods are based on the solution of volume fractions for each phase along with pressure and velocity relaxation procedures. In some multi-phase flows, several phases may be present with very small volume fractions but with high influence on overall flow field. Examples to these phases may include liquid or solid particles suspended in a primary gas phase. Due to very low volume fraction and low compressibility of these phases, pressure and velocity relaxation procedures may not be valid. Pressure relaxation procedure may be completely ignored while heat transfer mechanisms may become important. Similarly, velocity equality assumption on phase interfaces is not valid for small particles, instead a slip velocity approach is required for momentum transfer terms between the particles and the primary phase. In this chapter, methods for compressible multi-phase flows with highly diluted secondary phases are discussed. The results of this Chapter will also be used for testing the applicability of the discretization methods developed in Chapter 6 for dilute particles in a primary gas phase.

In a dilute mixture, the volume occupied by the dilute phase may be ignored. The dilute approximation leads to another assumption which assumes there is no interaction between dilute particles. With these assumptions, volume fraction and pressure terms are dropped from Equations 3.1.

$$\frac{\partial \rho_g}{\partial t} + \frac{\partial \rho_g u_g}{\partial x} = \dot{m} \quad (5.1)$$

$$\frac{\partial \rho_g u_g}{\partial t} + \frac{\partial (\rho_g u_g^2 + P)}{\partial x} = \dot{m} u_p + F_d \quad (5.2)$$

$$\frac{\partial \rho_g E_g}{\partial t} + \frac{\partial u_g (\rho_g E_g + P)}{\partial x} = \dot{m} E_i + F_d u_p + Q_i \quad (5.3)$$

$$\frac{\partial \rho_p}{\partial t} + \frac{\partial \rho_p u_p}{\partial x} = -\dot{m} \quad (5.4)$$

$$\frac{\partial \rho_p u_p}{\partial t} + \frac{\partial \rho_p u_p^2}{\partial x} = -\dot{m} u_p - F_d \quad (5.5)$$

$$\frac{\partial \rho_p E_p}{\partial t} + \frac{\partial u_p \rho_p E_p}{\partial x} = -\dot{m} E_i - F_d u_p - Q_i \quad (5.6)$$

where,

$$E_p = e_p + \frac{1}{2} |u|^2, \quad e_p = T_p C_p \quad (5.7)$$

The two equation systems are coupled only via phase interaction terms due to lack of volume fractions. The equation system for gas phase is the same with classical single phase gas equations except the momentum source term. However equation system for the dilute phase without volume fraction and pressure terms is a degenerate hyperbolic system mainly due to lack of particle interaction terms. As a result of ignoring particle interaction and volume fraction of particles, the particle trajectories may cross which is not true for classical gas dynamics.

While the equation system for gas phase admits three different real eigenvalues  $\lambda_1 = u_g - a, \lambda_2 = u_g, \lambda_3 = u_g + a$  with three different eigen vectors, the second system of equations for particle phase admits only one characteristic speed  $\lambda_{4,5,6} = u_p$  with two linearly independent Eigen vectors instead of three. The degeneracy of the system is due to this missing eigenvector associated with the eigenvalue  $\lambda_6 = u_p$ . In fact the

main implications of this degeneracy are the known physical assumptions. Due to lack of pressure terms in particle equations particle vacuums can exist and particle trajectories may cross [43]. When the two particle groups cross, a new family of particles is formed due to average representation in particle equations which results in loss of particle history information.

The solution of the particle phase equations is based on a particle phase Riemann solver similar to the explained in [43].

$$F_s^p = \begin{cases} S_L U_L & \text{if } S_L \geq 0 \quad \& \quad S_R \geq 0 \\ S_R U_R & \text{if } S_L \leq 0 \quad \& \quad S_R \leq 0 \\ 0 & \text{if } S_L \leq 0 \leq S_R \\ (U_L + U_R) \left( \frac{\rho_L S_L + \rho_R S_R}{\rho_L + \rho_R} \right) & \text{if } S_R < 0 < S_L \end{cases} \quad (5.8)$$

## 5.1 Interface Drag

The drag force exerted by a single particle on the continuous phase is calculated by

$$\vec{F}_{d,s} = \frac{1}{2} C_D \rho_g A_p \left| \vec{U}_p - \vec{U}_g \right| \left( \vec{U}_p - \vec{U}_g \right) \quad (5.9)$$

where  $C_D$  and  $A_p$  are the drag coefficient and surface area of a single particle projected in the flow direction. In Equation 5.9, subscripts  $g$  and  $p$  refer to continuous fluid phase and the secondary particle phases respectively. For the computational purposes, the number of particles in the cell  $c$  with volume  $V_c$  may be calculated as,

$$n_c = \frac{6V_c \rho_p}{\rho_s \pi d_p^3} \quad (5.10)$$

where  $\rho_s$  is the density of the particle phase material and  $d_p$  is the diameter of the particles.

Using Equations 5.9 and 5.10 the volumetric momentum source term due to particle drag is calculated as,

$$\vec{F}_d = \frac{3\rho_p C_D \rho_g}{4\rho_s d_p} |\vec{U}_p - \vec{U}_g| (\vec{U}_p - \vec{U}_g) \quad (5.11)$$

## 5.2 Drag Models

Using the model of Schiller and Naumann [45] model, drag coefficient  $C_D$  can be calculated as,

$$C_D = \max \left\{ \frac{24}{Re_p} (1 + 0.15 Re_p^{0.687}); 0.445 \right\} \quad (5.12)$$

where Reynolds number  $Re_p$  is defined as

$$Re_p = \frac{\rho_g d_p |\vec{U}_g - \vec{U}_p|}{\mu} \quad (5.13)$$

Schiller Naumann drag model is applicable to sparsely distributed spherical solid particles where both viscous and inertial are important.

At low particle Reynolds numbers ( $Re \ll 1$ ), the drag force for small particles may be calculated analytically [8] by Stoke's law.

$$\vec{F}_d = \frac{\rho_p (\vec{U}_p - \vec{U}_g)}{\tau_d} \quad (5.14)$$

where  $\tau_d$  is dynamic relaxation time of the particle defined as,

$$\tau_d = \frac{\rho_s d_p^2}{18\mu} \quad (5.15)$$

Stoke's law finds use in the motion of colloidal particles under the influence of an electric field, in the theory of sedimentation, and in the study of movement of aerosol particles. It is valid up to a Reynolds number of about 0.1.

### 5.3 Inter-phase Heat Transfer

The heat transfer between dilute particles and the fluid phase occurs due to thermal non-equilibrium across phase interfaces. Heat transfer rate per unit volume is proportional to the temperature difference as,

$$Q_i = ha_p(T_p - T_g) \quad (5.16)$$

where  $h$  is the heat transfer coefficient between particle and fluid phases and  $a_p$  is the inter-facial area per unit volume which is calculated for spherical particles as

$$a_p = \frac{6\rho_p}{d_p\rho_s} \quad (5.17)$$

Heat transfer rate is rewritten as,

$$Q_i = \frac{6k_g\rho_p Nu_p}{d_p^2\rho_s} (T_p - T_g) \quad (5.18)$$

Here  $k_g$  is the thermal conductivity of the fluid phase. The particle Nusselt number  $Nu_p$  is determined from a proper correlation. The default one used is the correlation of Ranz and Marshall [39, 38] which is the most well tested correlation for flow past a spherical particle,

$$Nu_p = 2.0 + 0.6Re_p^{1/2}Pr^{1/3} \quad (5.19)$$

where  $Pr$  is the Prandtl number of the fluid phase:

$$Pr = \frac{C_{p_g}\mu_g}{k_g} \quad (5.20)$$

This model is applicable in the ranges  $0 \leq Re < 200$  and  $0 \leq Pr < 250$ .

For low Reynolds, Nusselt number is given by  $Nu = 2$ , which can be derived analytically [8] for a sphere in a stagnant fluid. This is also the limiting value of Eq. 5.19 for

low Reynolds numbers. This result finds application in many processes that involve sprays of bubbles or droplets.

## **5.4 Particle Phase Boundary Conditions**

As pointed earlier in this section, the system of equations for particle phase admits only one characteristic speed. This simplifies the almost all boundary conditions with the exception of reflection boundary condition [43].

### **5.4.1 Inlet Conditions**

The following combinations of inlet conditions may be imposed at the boundaries:  $\dot{m}_p$  and  $\rho_p$ , or  $\vec{u}_p$  and  $\rho_p$ , or  $\dot{m}_p$  and  $\vec{u}_p$ .

### **5.4.2 Outlet Conditions**

The absorption conditions for particles are suitable which are similar to the transmissive conditions for gas phase. At an absorption boundary, the state in a phantom boundary cell is taken equal to the one in the neighboring boundary cell.

## **5.5 Test Cases of Dilute Particle Phase Model**

### **5.5.1 Attenuation and Dispersion of Acoustic Waves by Particulate-relaxation Processes [27]**

In this test case, attenuation and dispersion of acoustic waves by particulate-relaxation processes is studied.<sup>1</sup> The temperature and velocity of a particle suspended in an acoustic field are subject to fluctuations that may lag behind those of the surrounding fluid [47]. This test case is based on the theory of Temkin and Dobbins [47]. In their original paper, a theory for acoustic attenuation and dispersion in an aerosol

---

<sup>1</sup> This test case is done as a part of NATO-RTO AVT T-005 SUPPORT PROJECT between ROKETSAN (Turkey) and ONERA (France).

based on particulate relaxation processes is given. The particulate-relaxation theory predicts attenuation and dispersion by small, heavy particles, in close agreement with more detailed theories, for values of  $\omega\tau_d$  ( $\omega$  is the circular acoustic frequency,  $\tau_d$  is the dynamic relaxation time of the particle) smaller than and including unity [47]. Comparison with existing experimental data of attenuation and dispersion shows good agreement with their theory [47].

### 5.5.1.1 Main Hypothesis

Theoretical development of this test case is based on the following assumptions [47];

- The gas is thermally and calorically perfect.
- The density of the particles is much greater than the density of the surrounding
- Mass transfer between particles and gas is absent.
- The total heat and momentum transfer rate between particulate phase and gas phase is the sum of the effects due to each particle. This implies that the particle diameter is assumed to be much smaller than the distance between the particles.
- The heat transfer between gas and particles and the resistance force to the motion of the particles are given by expression applicable in the limit of zero Reynolds number.
- The fluctuations of pressure, density, and temperature produced by the acoustic wave are assumed to be so small as compared with their mean values that their squares of their cross products can be neglected. Similarly, the fluid velocity is much smaller than the speed of sound.
- Gas dissipation terms are assumed to be small with respect to two-phase dissipation terms [1].
  - Gas viscous stress and inside heat conduction are neglected.
- The particles are rigid (no surface tension effects), spherical and uniform temperature and size.
  - No heat conduction inside the dispersed phase.

### 5.5.1.2 Theoretical Development of The Test Case

The general one dimensional equation for two-phase flow consisting of gas and particle phases is given below. Equations for the gas phase are;

$$\frac{\partial \bar{\rho}}{\partial t} + \frac{\partial \bar{\rho}u}{\partial x} = 0$$

$$\bar{\rho} \left[ \frac{\partial u}{\partial t} + u \left( \frac{\partial u}{\partial x} \right) \right] + \frac{\partial \bar{p}}{\partial x} = \bar{n}F_p \quad (5.21)$$

$$\bar{\rho}C_v \left[ \frac{\partial \bar{T}}{\partial t} + u \left( \frac{\partial \bar{T}}{\partial x} \right) \right] + \bar{P} \left( \frac{\partial u}{\partial x} \right) = \bar{n}Q_p + \bar{n}F_v (u - u_p)$$

Equations for the particulate phase are;

$$\frac{\partial \bar{\rho}_p}{\partial t} + \frac{\partial \bar{\rho}_p u_p}{\partial x} = 0$$

$$\bar{\rho}_p \left[ \frac{\partial u_p}{\partial t} + u_p \left( \frac{\partial u_p}{\partial x} \right) \right] = -\bar{n}F_p \quad (5.22)$$

$$\bar{\rho}_p C'_p \left[ \frac{\partial \bar{T}_p}{\partial t} + u_p \left( \frac{\partial \bar{T}_p}{\partial x} \right) \right] = -\bar{n}Q_p$$

The perfect gas law is

$$\bar{p} = \bar{R}\bar{\rho}\bar{T} \quad (5.23)$$

The governing equations above are linearized by substituting perturbed values of variables. Since perturbations of variables are small quantities their squares and cross products can be neglected. The conservation equations for the gas phase reduce to;

$$\frac{\partial \rho}{\partial t} + \rho_0 \left( \frac{\partial u}{\partial x} \right) = 0$$

$$\rho_0 \left( \frac{\partial u}{\partial x} \right) + \frac{\partial p}{\partial x} = n_0 F_p \quad (5.24)$$

$$\rho_0 \left[ \frac{\partial T}{\partial t} \right] + P_0 \left( \frac{\partial u}{\partial x} \right) = n_0 Q_p$$

The conservation equations for the particulate phase are given by

$$\frac{\partial \rho_p}{\partial t} + n m' \frac{\partial u_p}{\partial x} = 0$$

$$m' \left( \frac{\partial u_p}{\partial t} \right) = -F_p \quad (5.25)$$

$$m' C_p' \left( \frac{\partial T_p}{\partial t} \right) = -Q_p$$

The linearized perfect-gas law takes the form

$$P = \bar{R} (\rho T_0 + \rho_0 T) \quad (5.26)$$

If the drag force and heat transfer are specified, equations 5.24- 5.26 represent seven simultaneous partial differential equations in seven unknowns. It is assumed that the drag is given by Stoke's law for motion of a sphere in a viscous fluid. Similarly the heat transfer coefficient  $h$  is assumed equal to  $k/R$ . Also applicable for low-Reynolds-number flows. With these assumptions,  $F_p$  and  $Q_p$  are given by

$$F_p = 6\pi R (u_p - u) \quad (5.27)$$

and

$$Q_p = 4\pi R k (T_p - T) \quad (5.28)$$

When considering a droplet oscillating in an acoustic field, two parameters having dimensions of time appear. One of these is the dynamic relaxation time of the droplet defined

$$\tau_d = \frac{2R^2 \rho'}{9\mu} \quad (5.29)$$

The other is the thermal relaxation time of the particle and is denoted by

$$\tau_t = \frac{\text{Pr } C_p' R^2 \rho'}{3\mu C_p} = \frac{3}{2} \frac{C_p'}{C_p} \text{Pr } \tau_d \quad (5.30)$$

Assuming that all the unknown quantities depend on  $x$  and  $t$  through a factor

$$\varphi(x, t) = A_\varphi e^{i(Kx - \omega t)} \quad (5.31)$$

where

$$K = k + ik_2 \quad (5.32)$$

The result is a system of four homogeneous, algebraic equations. The system has a solution only if the determinant vanishes. Equating the resulting determinate to zero, it is found that  $K$  should satisfy the following equation:

$$\left(\frac{Ka_0}{\omega}\right)^2 \left(1 + \frac{C_m C'_p / C_p}{1 - i\omega\tau_t}\right) = \left(1 + \frac{C_m}{1 - i\omega\tau_d}\right) \left(1 + \frac{\gamma C_m C'_p / C_p}{1 - i\omega\tau_t}\right) \quad (5.33)$$

Equation 5.33 can be solved in favor of  $k_1$  and  $k_2$ , which in turn are connected with the speed of sound and attenuation coefficients by

$$a = \frac{\omega}{k_1} \quad (5.34)$$

and

$$\alpha = 2k_2 \quad (5.35)$$

The attenuation coefficient  $\alpha$  gives the energy dissipated per unit length.

Another important coefficient is related to dispersion of acoustic energy;

$$\beta = k_1^2 - \left(\frac{\omega}{a_0}\right)^2 \quad (5.36)$$

The physical interpretation of attenuation coefficient and dispersion coefficient can be inferred from the Figure 5.1.  $\alpha$  is the coefficient of decreasing exponential and

$\beta$  characterizes the velocity of the wave in the two-phase medium compared to the sound velocity in the pure gas.

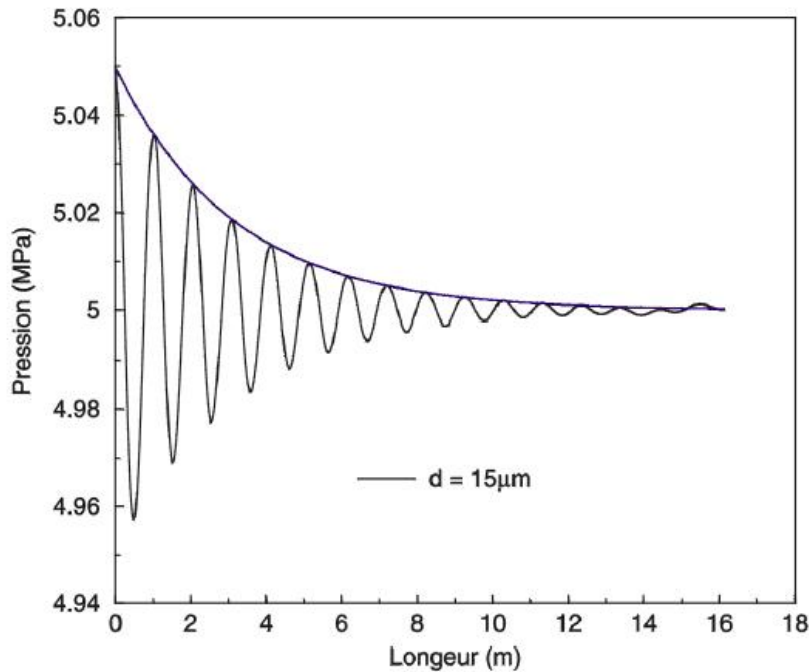


Figure 5.1: Attenuation of sound waves due to  $15\mu m$  diameter particles [14].

### 5.5.1.3 Attenuation and Dispersion Due to Numerical Diffusion

All practical numerical schemes for solving fluid flow contain a finite amount of numerical diffusion. The amount of numerical diffusion is inversely related to the mesh resolution. It is always advantageous to use high order schemes to reduce numerical diffusion. In Figure 5.2, the results of numerical simulation with different flux solvers of CMPS code are shown. In these simulations 16 cells per wave length are used. The HLL-WAF+MUSCLE scheme results in the lowest numerical diffusion.

### 5.5.1.4 Numerical Test Case

The aim of this test case is to reproduce the results of the analysis explained in Section 5.5.1.2 by numerical simulation. The propagation of sound waves in a channel including suspended particles is simulated. The attenuation and dispersion characteristics

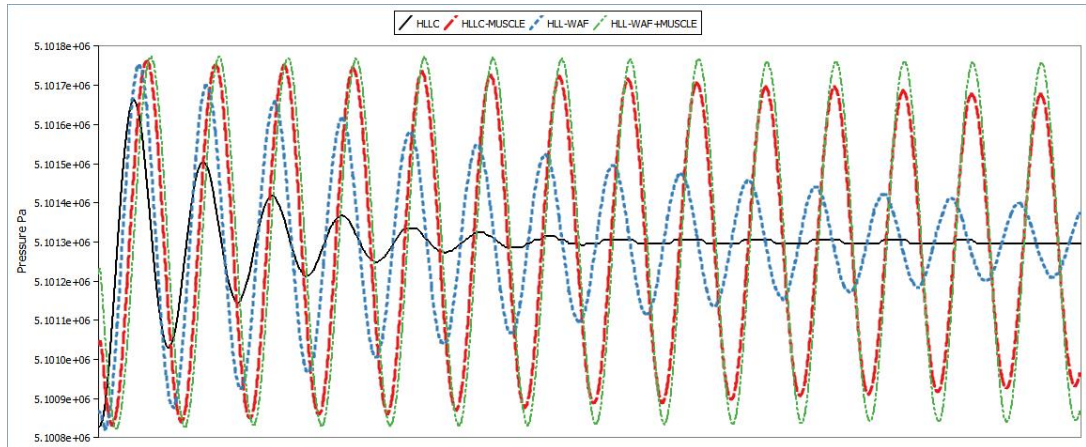


Figure 5.2: Attenuation of sound waves due to numerical diffusion with different numerical schemes.

of particles of different sizes are studied.

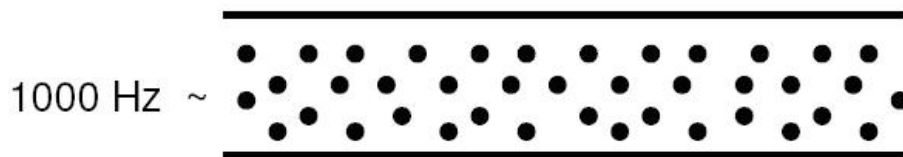


Figure 5.3: Schematic representation of the test case for propagation of sound waves in a channel including suspended particles.

The frequency of the sound waves entering the channel is  $1000\text{Hz}$  with relative amplitude of  $0.01\%$  about  $P_0 = 50\text{bar}$ . Parametric study is done on the sizes of particles between  $5 - 120\mu\text{m}$ . In the simulations 20 cells per wave length were used which provides sufficient resolution for negligible numerical diffusion with HLL-WAF+MUSCLE scheme.

The gas and particle properties are given below;

For momentum and heat transfer terms Stokes law (Equations 5.27 and 5.28) were used. The momentum transfer was formulated as;

	Gas	Particle
Density	Ideal gas.	1550kg/m <sup>3</sup>
$C_p$	2440J/kg.K	1176J/kg.K
Thermal conductivity k	0.5551W/m.K	202.4W/m.K
Molecular weight	27.7469kg/moles	-
Viscosity	$9.1 \times 10^{-3}$ Pa.s	-

Table5.1: Gas and particle properties.

$$F_p = \frac{\rho' (u_p - u)}{\tau_d} \quad (5.37)$$

The heat transfer term was formulated as;

$$Q_p = \frac{6k\rho'Nu_p}{R^2\rho_s} (T_p - T) \quad (5.38)$$

For low Reynolds numbers, Nusselt number is given by  $Nu = 2$  which is used for this test case.

The acoustic wave introduced to the computation domain by subsonic pressure inlet boundary condition available in CMPS code. In this boundary condition, the out going Riemann invariant is used to determine the speed of sound. Then other quantities like temperature, pressure, density or the absolute velocity at the boundary are evaluated. For the outlet boundary pressure outlet condition available in CMPS was used. This condition is based on the AUSM scheme [33] (see Section 2.11.3).

### 5.5.1.5 Results

The simulations were repeated for particles with diameters of  $R = 5, 8, 10, 12, 15, 18, 20, 30, 40, 80$  and  $120 \mu m$ . The stiff source terms due to small particles did not lead to numerical difficulties with multi stage time stepping with source splitting.

The solutions of equation 5.33 for particles of different sizes (that is for  $\omega\tau_d$  values) give attenuation and dispersion of the acoustic energy which are written in a non-dimensional form as;

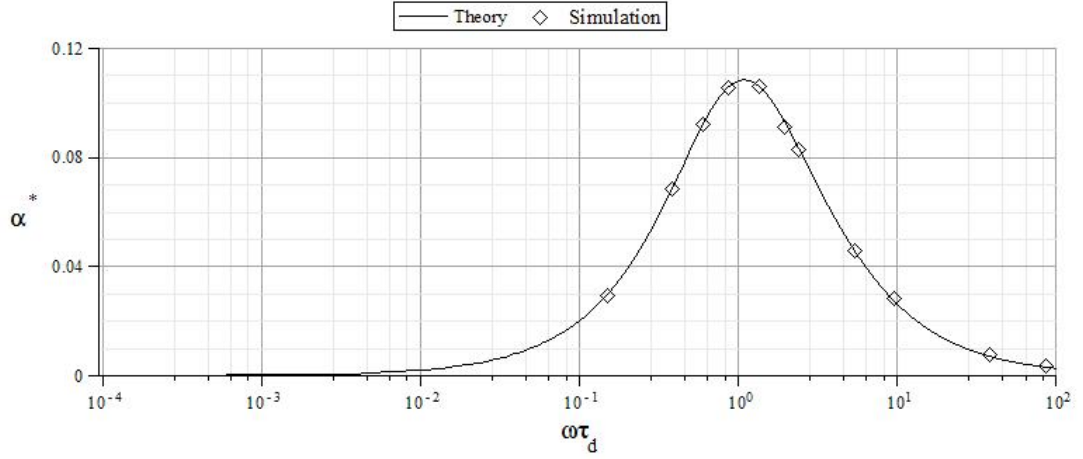


Figure 5.4: Attenuation by particles of different diameters.

$$\alpha^* = \left(\frac{a_0}{\omega}\right)\alpha \quad (5.39)$$

$$\beta^* = \left(\frac{a_0}{\omega}\right)^2\beta \quad (5.40)$$

and

$$\omega\tau_d = \frac{2\pi f\rho_0 R^2}{18\mu} \quad (5.41)$$

In Figure 5.4 and Figure 5.5, the results of CMPS simulations and theory are compared. The theory and simulation results show good agreement. As expected there is an attenuation peak at  $\omega\tau_d \approx 1$ . Although this test case shows the potential use of these numerical methods for analyzing the acoustic phenomena such as acoustic instabilities in complex rocket motor geometries, high computational cost of such transient calculations for complex geometries should be considered well.

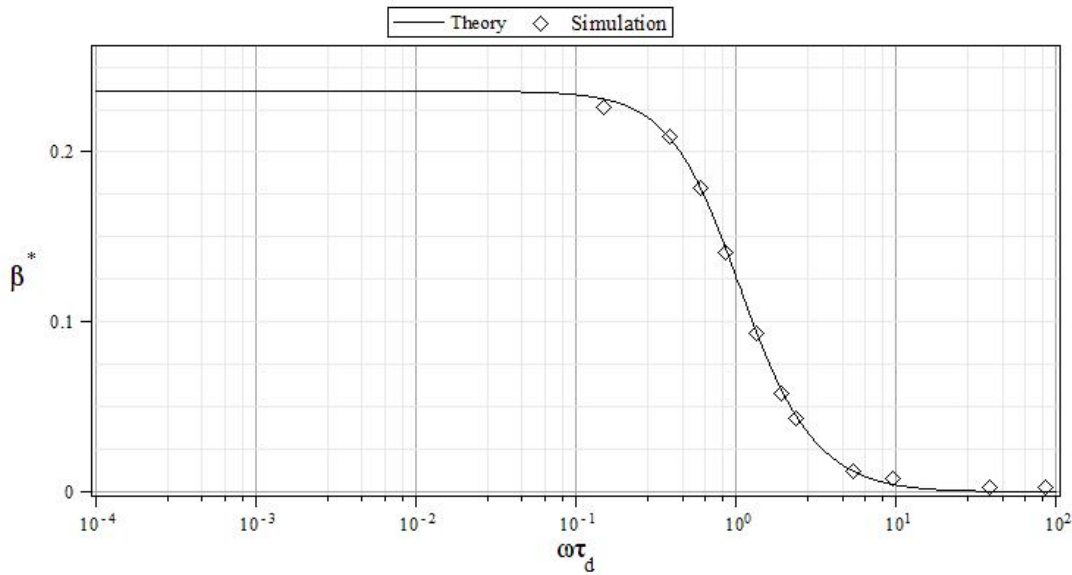


Figure 5.5: Dispersion by particles of different diameters.

### 5.5.2 Simulation of Two Phase Inert Tep [27]

In this test case<sup>2</sup>, a representative model for solid propellant motor geometries is studied. Test is based on code-to-code comparison. The code SIERRA (ONERA, France) is well tested software for these types of simple systems. This test case is proposed and defined by ONERA in the scope of an NATO RTO project between ONERA and ROKETSAN (Turkey) who supported the dilute phase solver of the CMPS code. In this section the results of the test problem belong to this project and will be named as ONERA (SIERRA) or ROKETSAN (CMPS) results.

#### 5.5.2.1 Geometry and Grid

Geometry consists of a single domain with 99x16 grid points shown in Figure 5.6. Due to numerical methods used in CMPS code, this domain can also be defined as a 98x15 grid cells. Problem is axisymmetric two-dimensional. Grid is given by ONERA.

<sup>2</sup> This test case is done as a part of NATO-RTO AVT T-005 SUPPORT PROJECT between ROKETSAN (Turkey) and ONERA (France). The dilute phase solver of the CMPS is validated for solid rocket motors.

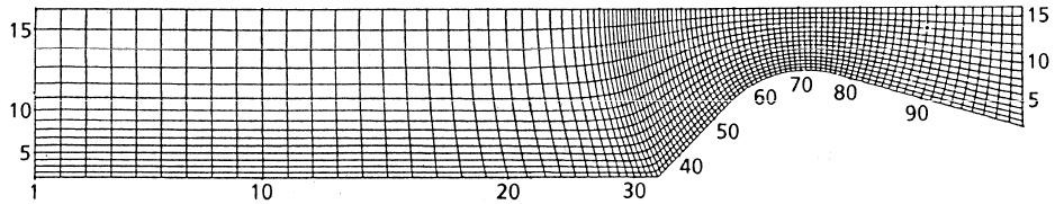


Figure 5.6: Grid structure given by ONERA[14]

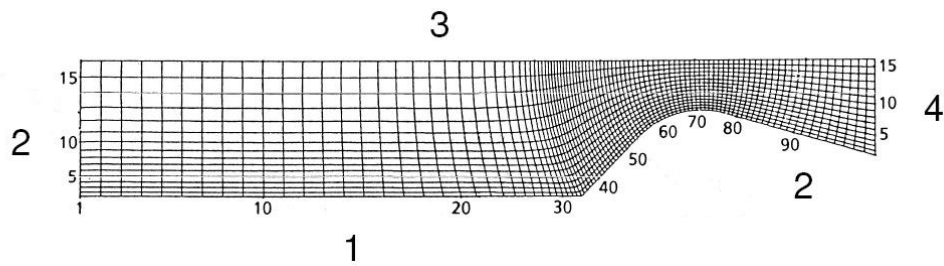


Figure 5.7: Boundary zones[14]

### 5.5.2.2 Boundary Conditions

Boundary conditions are applied as shown in Figure 5.7. Injection wall is used until point 34 in Figure 5.7 (see Section 2.11.1). Injection is normal to the face. For gas phase, mass flow inlet boundary available in CMPS code is used. In this boundary condition, static temperature and mass flow rate are given by user. If the flow is subsonic, static pressure is extrapolated from the domain; otherwise total pressure is also given by the user. This information is used to construct a second order equation for density, which is solved to calculate velocity components. For the particle phase, mass flow rate, velocity and temperature are given by the user. Particles and gas are not in dynamic or thermal equilibrium. For wall surfaces, slip boundary is used for both gas and particle phases. Walls are adiabatic for both phases. The x-axis in 2D coordinate system is used as a symmetry axis. For out flow boundary, all variables are first order extrapolated in SIERRA code. In CMPS, pressure outlet boundary based on AUSM scheme [33] (see Section 2.11.2. scheme was used. Because the flow in this zone is supersonic, the two boundary conditions lead to the same calculational results.

	Gas	Particle
1. Propellant Surface	0.44893kg/s 3387K -	0.098546kg/s 2600K 0.01m/s
4. Outflow	AUSM	All variables are extrapolated.

Table5.2: Boundary conditions.

	Gas	Particle
Density	Ideal gas	1803kg/m <sup>3</sup>
$C_p$	2437J/kg.K	1177J/kg.K
Thermal conductivity k	0.45618W/m.K	202.4W/m.K
Molecular Weight	27.78	-
Viscosity	$9.06 \times 10^{-5} Pa.s$	-
Diameter	-	30 $\mu$ m

Table5.3: Material Properties.

### 5.5.2.3 Material Properties

Material properties of gas and particle phases are given in table 5.3.

### 5.5.2.4 Heat and Momentum Transfer Terms

See the sections 5.1 and 5.3 for more details about the implementations of the equations given below in CMPS. The heat transfer between phases is calculated as;

$$Q_p = \frac{6k\rho'Nu_p}{R^2\rho_s} (T_p - T) \quad (5.42)$$

where

$$Nu_p = 2.0 + 0.6Re_p^{1/2} Pr^{1/3} \quad (5.43)$$

$$Pr = \frac{C_p\mu}{k} \quad (5.44)$$

The momentum transfer term is calculated between gas and particle phases are calculated as;

$$F_p = \frac{3\rho' C_D \rho}{4\rho_p R} |u_p - u| (u_p - u) \quad (5.45)$$

Drag coefficient  $C_D$  is defined as

$$C_D = \max \left\{ \frac{24}{\text{Re}} (1 + 0.15\text{Re}^{0.687}); 0.445 \right\} \quad (5.46)$$

where

$$\text{Re} = \frac{\rho R |u_p - u|}{\mu} \quad (5.47)$$

#### 5.5.2.5 Results

The results of the CMPS (ROKETSAN) and SIERRA (ONERA) are compared on two selected planes. These planes are shown in Figure 5.8

#### 5.5.2.6 Comparison of Data on Plane i=10

The comparison of results from CMPS (ROKETSAN) and SIERRA (ONERA) codes are shown in Figures 5.9-5.17. The lines labeled as ONERA (L) are results of Lagrangian solver in SIERRA code.

#### 5.5.2.7 Comparison of Data on Plane i=98

The comparison of results from CMPS (ROKETSAN) and SIERRA (ONERA) codes on the plane i=98 are shown in Figures 5.18-5.26 below. The lines labeled as ONERA (L) are results of Lagrangian solver in SIERRA code.

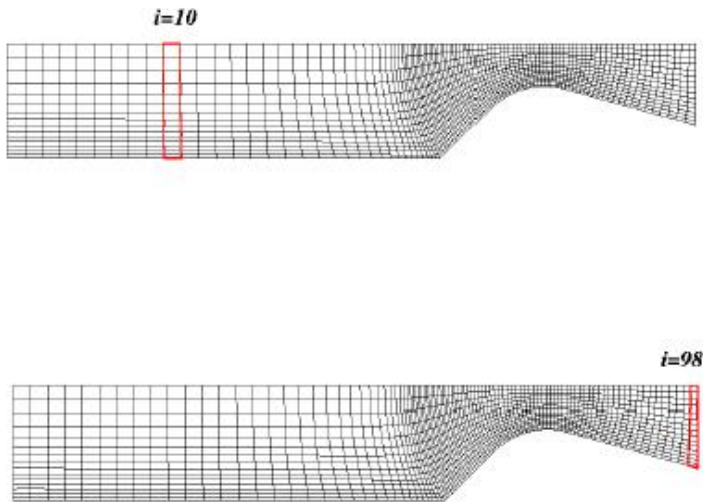


Figure 5.8: Grid points for comparison of results[14]

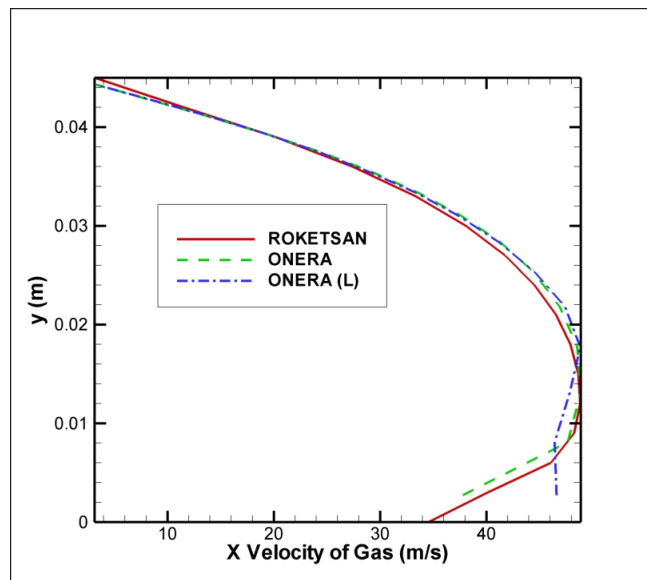


Figure 5.9: Axial velocities over line i=10 [27]

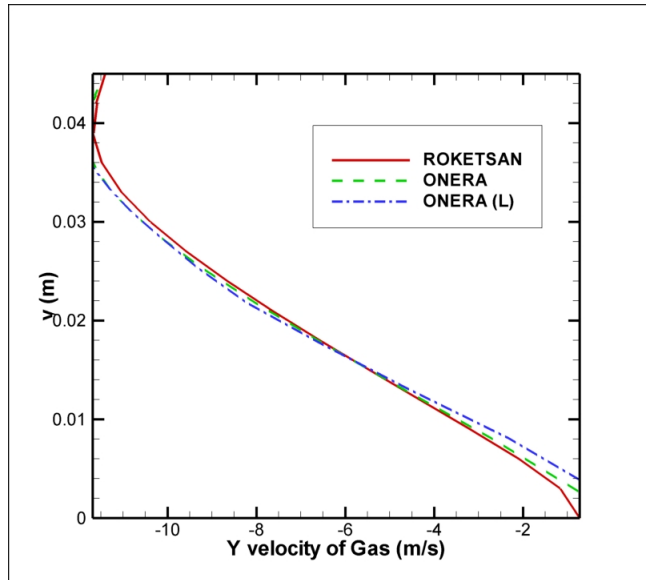


Figure 5.10: Radial velocities over line i=10 [27]

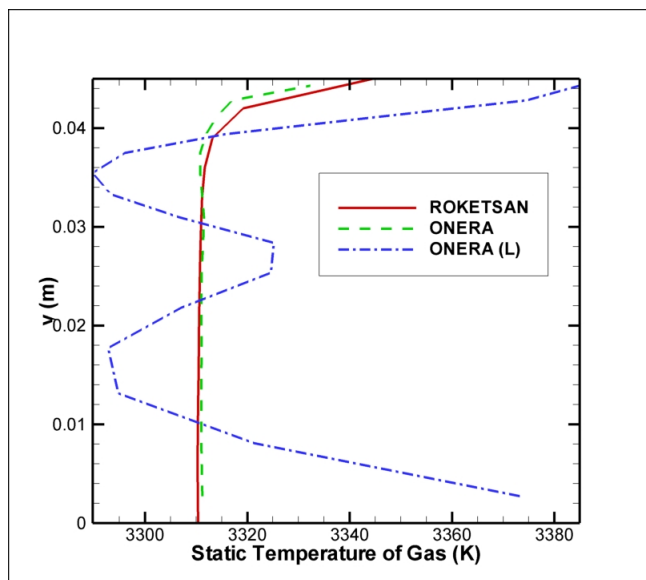


Figure 5.11: Gas temperatures over line i=10 [27]

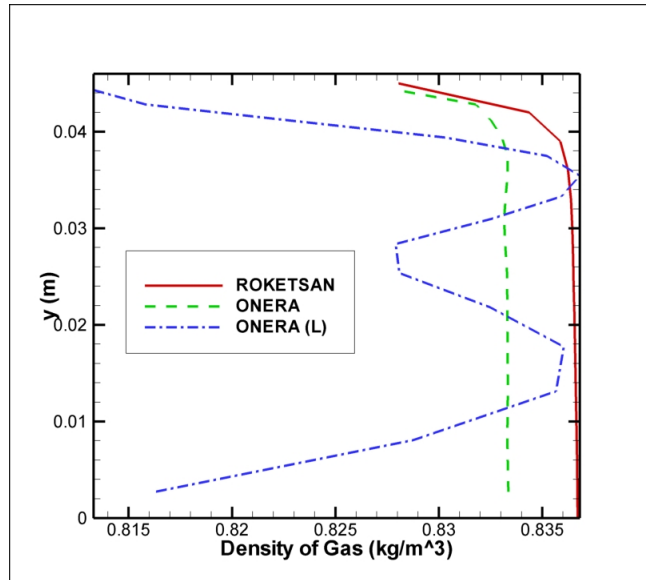


Figure 5.12: Gas densities over line i=10 [27]

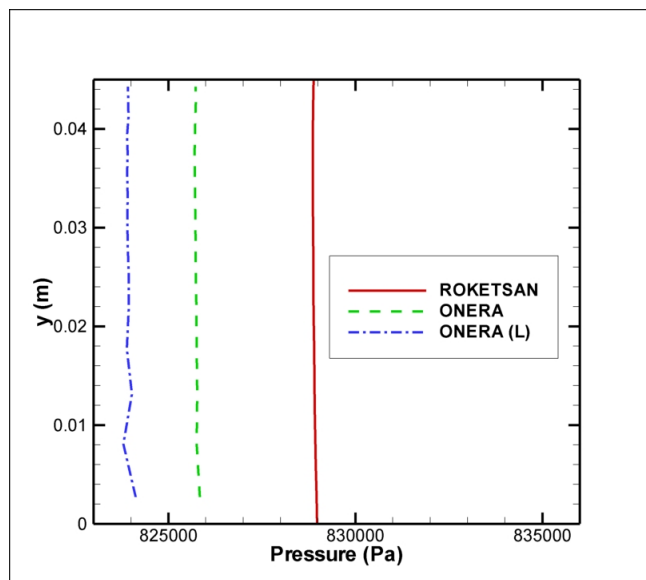


Figure 5.13: Static pressure over line i=10 [27]

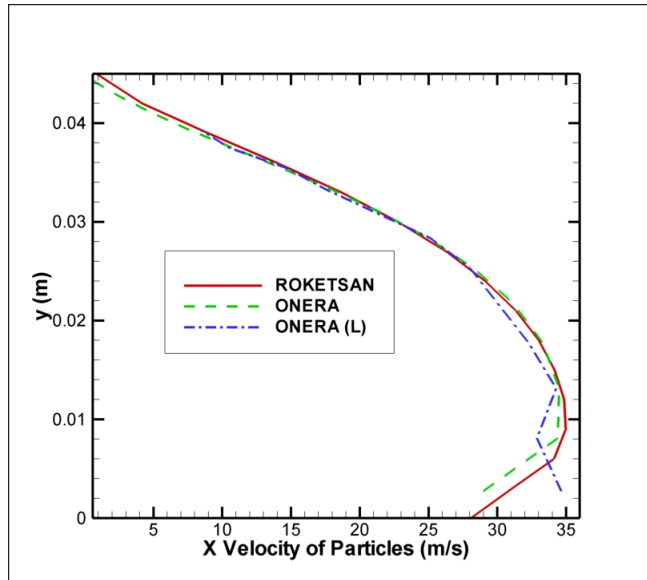


Figure 5.14: Axial particle velocities over line i=10 [27]

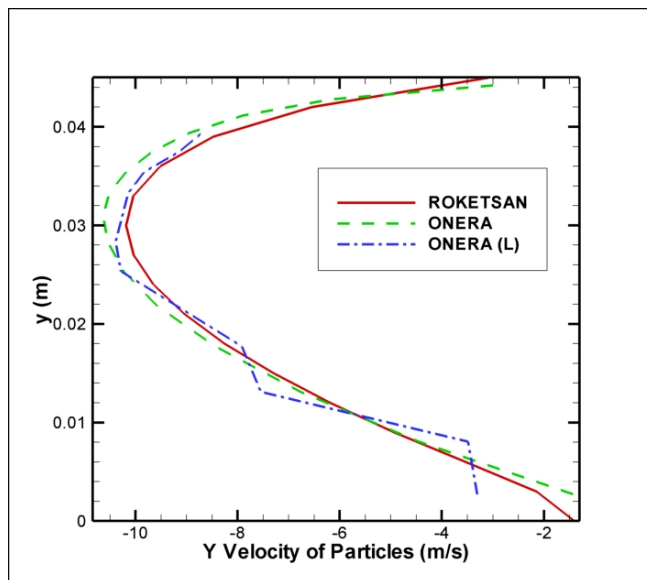


Figure 5.15: Radial particle velocities over line i=10 [27]

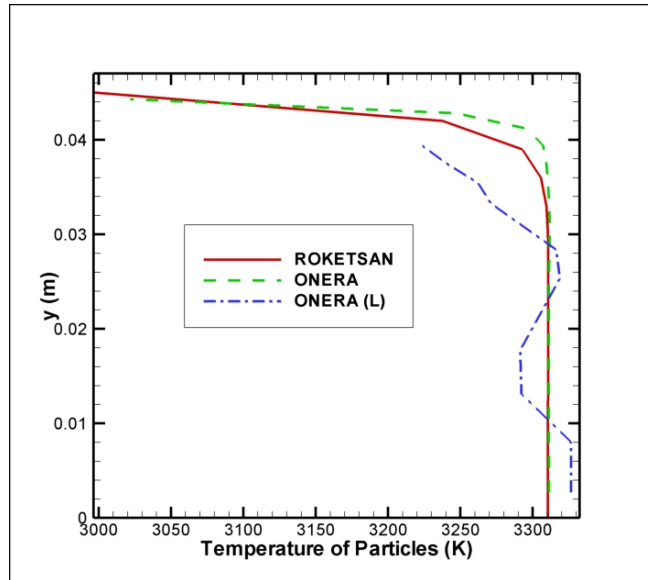


Figure 5.16: Particle temperatures over line i=10 [27]

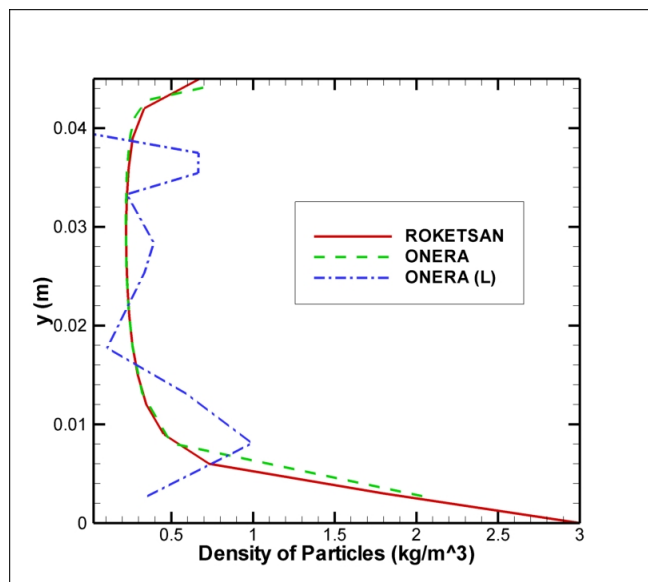


Figure 5.17: Particle densities over line i=10 [27]

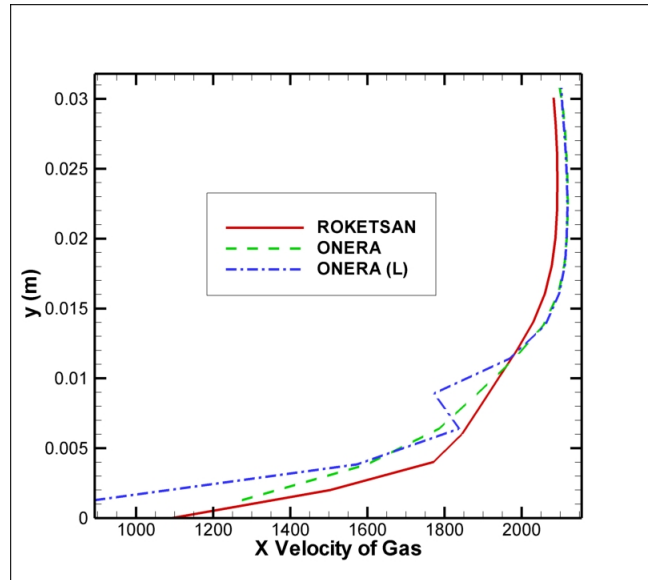


Figure 5.18: Axial gas velocities over line i=98 [27]

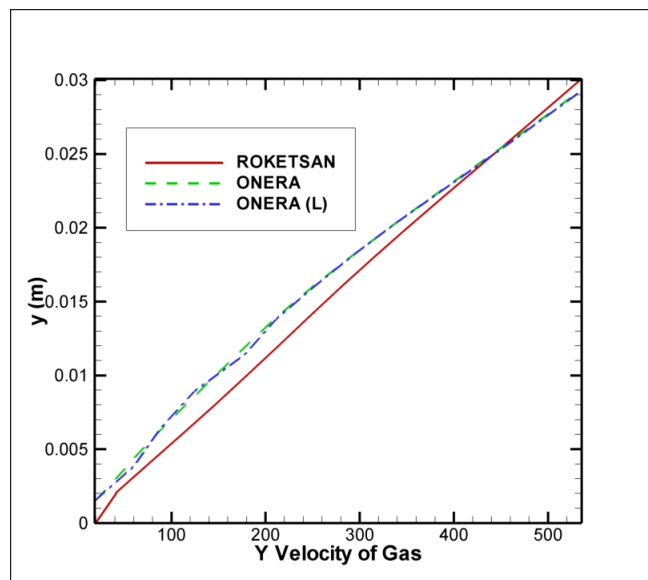


Figure 5.19: Radial gas velocities over line i=98 [27]

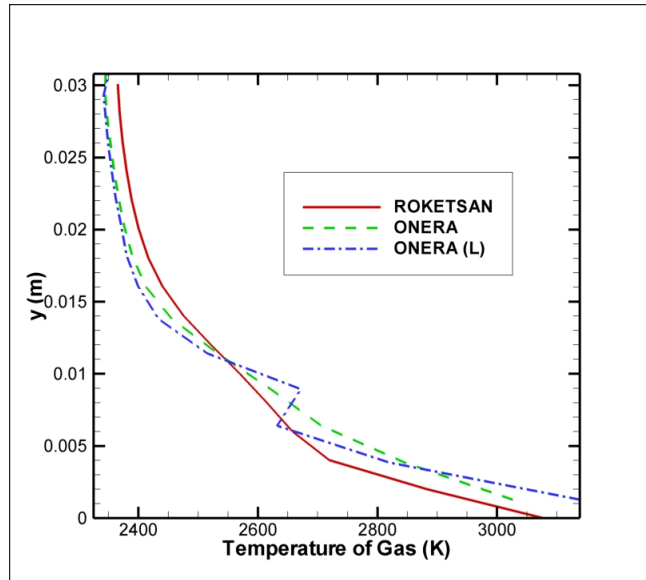


Figure 5.20: Gas temperature over line i=98 [27]

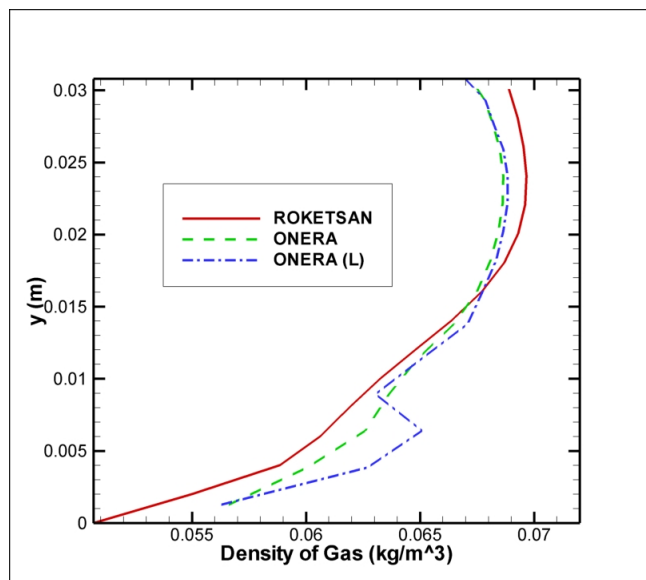


Figure 5.21: Gas densities over line i=98 [27]

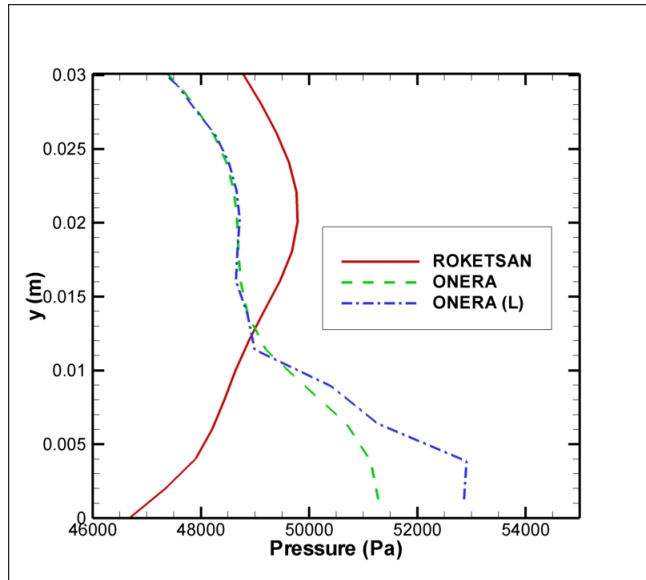


Figure 5.22: Gas pressure over line i=98 [27]

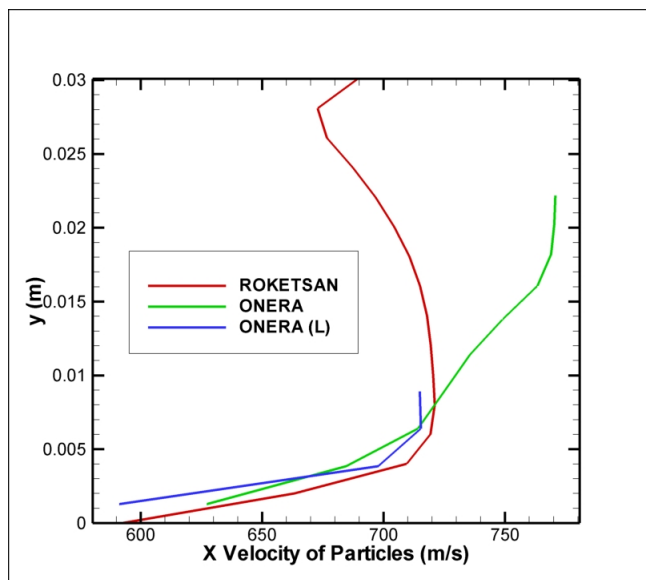


Figure 5.23: Particle axial velocities over line i=98 [27]

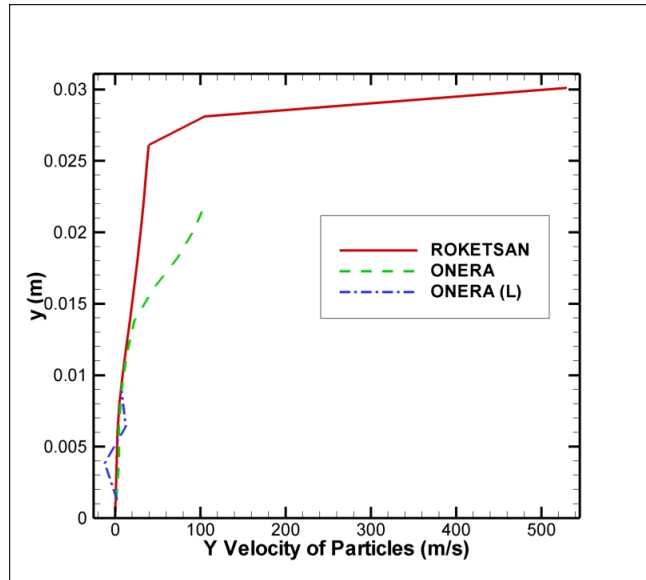


Figure 5.24: Particle radial velocities over line  $i=98$  [27]

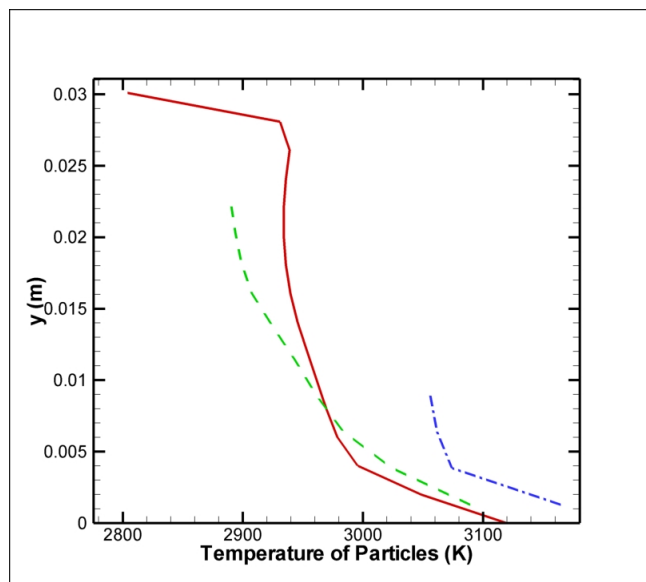


Figure 5.25: Particle temperatures over line  $i=98$  [27]

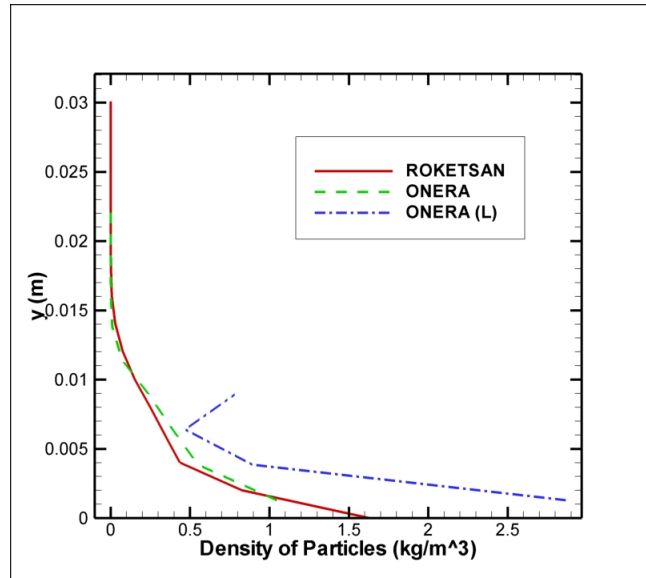


Figure 5.26: Particle densities over line i=98 [27]

### 5.5.2.8 Discussion of TEP Test Case Results

In this test case, a representative model for solid propellant motor geometries was studied. The dilute phase model was used for particle phases. For solving particle phase equations the flux solver based on the method defined in Eq. 5.8 was used. Existence of a single direction for the propagation of information for the system of equations governing the motion of the dispersed phase generated difficulties for treatment of certain boundary conditions especially on the axis line. These problems results in non-physical accumulation of particles especially at end of the motor on the axis. This problem is handled by limiting the particle concentrations on the solution domain.

The non-physical particles shocks and vacuums which was defined as problem of such systems is handled well by the schemes used in CMPS.

This study showed that the results of CMPS code and ONERA's SIERRA code are in good agreement for this test case. The only small difference was in the pressure in motor region. This difference very small and this is due to the preconditioning used

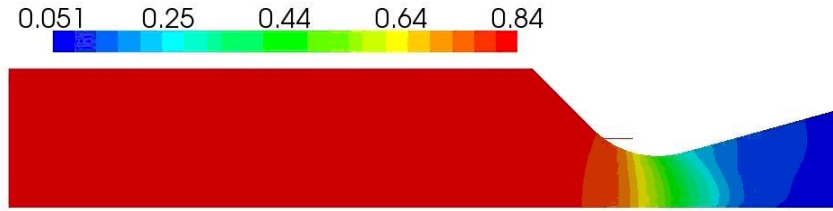


Figure 5.27: Contours of gas density  $kg/m^3$ .

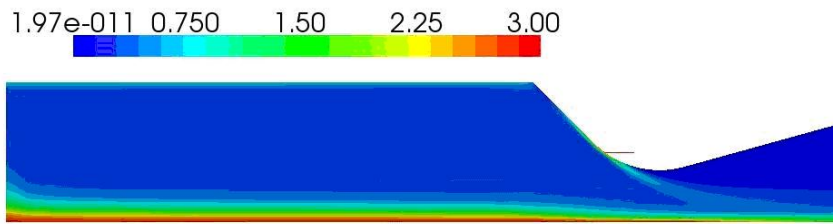


Figure 5.28: Contours of particle density  $kg/m^3$ .

by CMPS solver for handling low Mach number flow in the motor chamber. The other differences were observed with particle values on the nozzle exit line. This difference exists on a part of the line where particle vacuum problem resulted in difficulties for ONERA's solver.

Some contour plots of data from results of the solver CMPS for the TEP test case are shown in Figures 5.27-5.36. The difference between particle and gas velocity are high especially in the nozzle region where the velocity of gas phase is increasing with expansion. This difference leads to high momentum transfer rates especially near axis line where the particle concentrations are high. The difference between particle and gas phase temperature are also high in the nozzle region. In the nozzle region the temperature of the gas phase decreases due to expansion and also cools the particles with a higher heat transfer rates than the rates in the chamber region. The momentum and thermal coupling of the phases are very apparent in nozzle region.

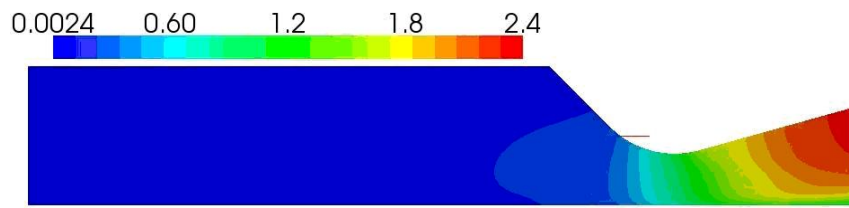


Figure 5.29: Contours of Mach number.

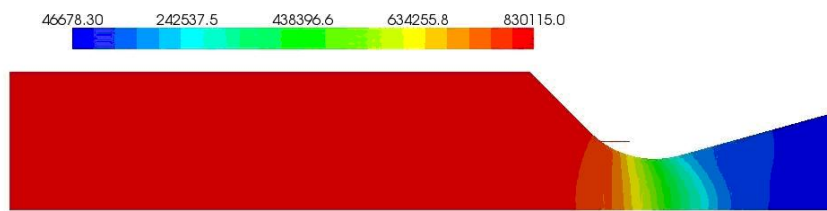


Figure 5.30: Contour of pressure  $Pa$ .

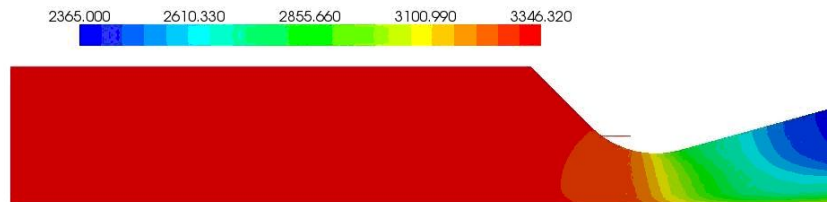


Figure 5.31: Contours of gas temperature  $K$ .

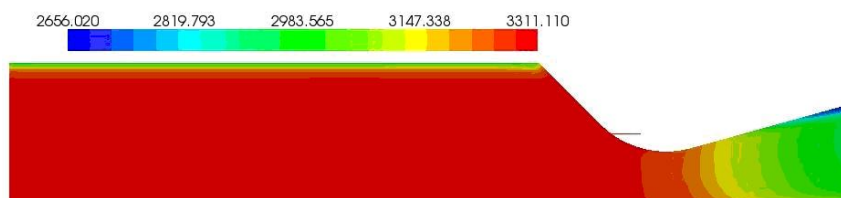


Figure 5.32: Contours of particle temperature  $K$ .

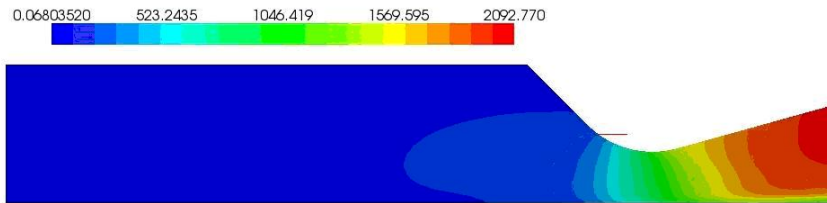


Figure 5.33: Contours of gas axial velocity  $m/s$ .

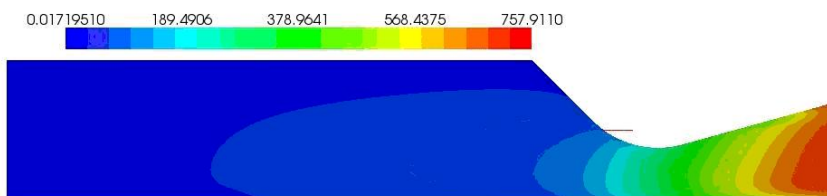


Figure 5.34: Contours of particle axial velocity  $m/s$ .

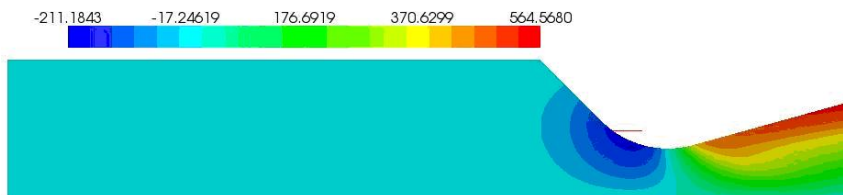


Figure 5.35: Contours of gas radial velocity  $m/s$ .

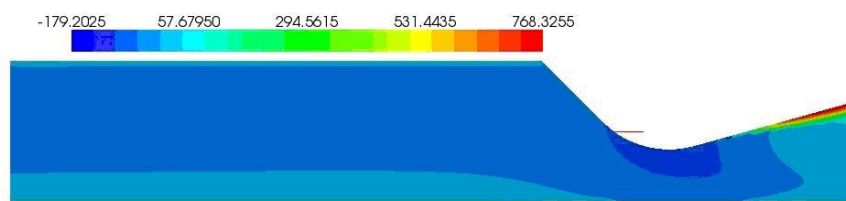


Figure 5.36: Contours of particle radial velocity  $m/s$ .

## CHAPTER 6

### HIGH RESOLUTION INTERFACE CAPTURING

#### 6.1 Discretization of Volume Fraction

The discretization method of volume fraction is crucial for successful implementation of the interface capturing scheme which should enable capturing of interfaces in a sharp form. The usual differencing schemes for incompressible flows have some problems and limitations with Godunov methods which are applied to compressible flows. First of all, for a Godunov type method described in Section 4.3, two volume fraction values are needed on either side of a cell face to support state discontinuity. This situation is not compatible with upwinding methods employed in usual high resolution volume fraction differencing schemes. Furthermore, the usual boundedness and availability criteria cannot be used with the current method. The differencing scheme of volume fraction used in this study is similar to the high resolution schemes of Leonard [32] and Ubbink [50] based on Normalized Variable Diagram (NVD) [32].

##### 6.1.1 Definitions

A schematic representation of a one dimensional control volume for the CHRIC scheme is given in Fig. 6.1. The center cell  $D$  is the donor cell, the cell  $A$  is the acceptor cell, and the cell  $U$  is the upwind cell. The flow direction is from the upwind cell to the acceptor cell. As aforementioned, two values of volume fractions are needed on a face, one for the right state and one for the left state. These values can be differentiated according to the flow velocity direction on the face. Below, the calculation procedure for the face volume fraction of an outgoing fluid  $\alpha_{fA}$  (volume fraction

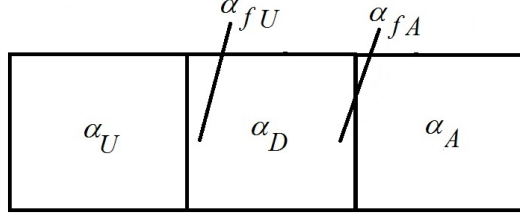


Figure 6.1: Cell representation for CHRIC scheme.

on the left side of the cell face between the donor and acceptor cells) is explained first. Then, the procedure for an incoming fluid volume fraction  $\alpha_{fU}$  (volume fraction on the right side of the cell face between the upwind and donor cells) is explained.

To differentiate from incompressible schemes, the scheme given in the next sections is named Compressible High Resolution Interface Capturing (CHRIC) scheme which is a non-linear blend of upwind and controlled downwind differencing [28]. Downwinding implies that the donor cell is to donate the same fluid as presently contained in the acceptor cell, thus the procedure ignores the presence of the other fluids in the donor cell [50]. This means that the donor cell will first donate all the available fluid required by the acceptor cell and then start to donate the other fluid. The amount of the fluid donated by donor cell is limited with the available fluid in donor cell. This is called the availability criteria. Another basic criteria about values of volume fractions is the boundedness criteria which states that in the absence of sources the value of a flow property in the flow domain cannot take values higher or lower than those prescribed on the boundaries of the flow domain [53]. For example, volume fraction cannot take values below zero and above one. Another criteria is local boundedness which states that a volume fraction value must be bounded with that of its nearest neighbors. This criteria is employed to limit the slopes of volume fractions used to reconstruct the face values.

Mathematically the availability criteria states that,

$$\alpha_{fA}^i u_f^i \rho_f^i A_f \Delta t \leq \alpha_D^i \rho_D^i V_D \quad (6.1)$$

where  $V_D$  is the volume of the donor cell. This equation can be written as

$$\alpha_{fA}^i \leq \frac{\alpha_D^i}{c_{fc}^i} \quad (6.2)$$

where  $c_{fc}^i$  is face Courant number based on convective speed on the face and is defined as

$$c_{fc}^i = \frac{u_f^i \rho_f^i A_f \Delta t}{\rho_D^i V_D} \quad (6.3)$$

The availability criteria puts a limit on volume fraction reconstruction inversely related to the value  $\Delta t$  which is also limited according to the Courant-Friedrichs-Lewy (CFL) condition.

Since the availability criteria puts limits only to the convected scalar data, this criteria alone is not sufficient for physically limited reconstruction of volume fraction for compressible flows. This can be explained using Fig. 4.4. Before any mechanical relaxation in a solution cell (velocity and pressure relaxation in this study), all the propagating information (wave fronts) should be limited to single phase volume in the cell as shown in Fig. 4.4. In other words, waves should not cross any phase interface in the solution cell. For a simple one dimensional configuration this constraint can be written as,

$$\alpha_{fA}^i S_{max} \Delta t A_f < \alpha_D^i V_D \quad (6.4)$$

where  $S_{max}$  is the maximum speed of the waves propagating into the donor cell. Eq. (6.4) can be rewritten in terms of a new face Courant number  $c_{fw}$ ,

$$\alpha_{fA}^i \leq \frac{\alpha_D^i}{c_{fw}} \quad (6.5)$$

where  $c_{fw}$  is defined as

$$c_{fw} = \frac{S_{max} \Delta t A_f}{V_D} \quad (6.6)$$

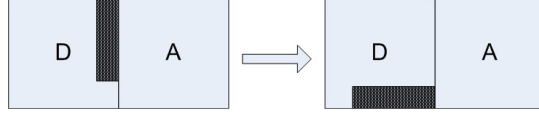


Figure 6.2: Reconfiguration of phase topology on a face according to face Courant number  $c_{fw}$ .

The boundedness criteria based on wave propagation defined by Eq. (6.5) can be achieved by choosing  $\Delta t$  according to phasic configuration on the cell face between the donor and acceptor cells. However, this may result in very small values for  $\Delta t$  when one of the phase volume fractions is very low. Another way to satisfy Eq. (6.5) is to reconfigure the phase topology on the face according to a given face Courant number  $c_{fw}$  so that sonic waves do not cross a phasic interface in the cell. This is explained in Fig. 6.2. According to the procedure depicted in this figure, as the face Courant number gets smaller the resolution of the volume fraction gets higher but  $\Delta t$  also gets smaller. This situation will get clearer in the following sections.

### 6.1.2 Compressible High Resolution Interface Capturing (CHRIC) Scheme

As aforementioned we follow the similar steps as schemes of Leonard [32] and Ubbink [50] based on Normalized Variable Diagram (NVD) [32]. The normalized cell  $\tilde{\alpha}_D$  and face values  $\tilde{\alpha}_f$  of volume fraction [32] are defined as

$$\tilde{\alpha}_D^i = \frac{\alpha_D^i - \alpha_U^i}{\alpha_A^i - \alpha_U^i} \quad (6.7)$$

$$\tilde{\alpha}_f^i = \frac{\alpha_f^i - \alpha_U^i}{\alpha_A^i - \alpha_U^i} \quad (6.8)$$

Gaskell and Lau [18] presented a Convection Boundedness Criteria (CBC) for one dimensional implicit flow calculations, and Leonard [32] adapted the CBC for explicit flow calculations. The CBC for explicit flow calculations reads,

$$\tilde{\alpha}_f^i = \tilde{\alpha}_D^i \quad \text{for } \tilde{\alpha}_D^i < 0 \text{ or } \tilde{\alpha}_D^i > 1 \quad (6.9)$$

$$\tilde{\alpha}_D^i \leq \tilde{\alpha}_f^i \leq \min \left\{ 1, \frac{\tilde{\alpha}_D^i}{c_f} \right\} \quad \text{for } 0 \leq \tilde{\alpha}_D^i \leq 1$$

where  $c_f$  is the maximum of the face courant numbers  $c_{fc}$  and  $c_{fw}$  which were defined in the previous section. Using the donor-acceptor formulation given by Eq.(6.2) and the CBC the normalized face value of volume fraction is calculated as

$$\tilde{\alpha}_{fCBC}^i = \begin{cases} \min \left\{ 1, \frac{\tilde{\alpha}_D^i}{c_f} \right\} & \text{for } 0 \leq \tilde{\alpha}_D^i \leq 1 \\ \tilde{\alpha}_D^i & \text{for } \tilde{\alpha}_D^i < 0, \tilde{\alpha}_D^i > 1 \end{cases} \quad (6.10)$$

Directly using this value  $\tilde{\alpha}_f$  does not preserve the shape of the interface which lies tangentially to the flow direction. To prevent this a correction is made to  $\tilde{\alpha}_f$  using the Ultimate-QUICKEST scheme [32], which is defined as,

$$\tilde{\alpha}_{fUQ}^i = \begin{cases} \min \left\{ \frac{8c_f\tilde{\alpha}_D^i + (1-c_f)(6\tilde{\alpha}_D^i + 3)}{8}, \tilde{\alpha}_{fCBC}^i \right\} & \text{for } 0 \leq \tilde{\alpha}_D^i \leq 1 \\ \tilde{\alpha}_D^i & \text{for } \tilde{\alpha}_D^i < 0, \tilde{\alpha}_D^i > 1 \end{cases} \quad (6.11)$$

Corrected normalized face value  $\tilde{\alpha}_f^{i*}$  is calculated from

$$\tilde{\alpha}_f^{i*} = \tilde{\alpha}_f^i \sqrt{\cos \theta} + \tilde{\alpha}_{fUQ}^i (1 - \sqrt{\cos \theta}) \quad (6.12)$$

where  $\theta$  is the angle between the interface and face normal vectors, and  $\cos \theta$  is calculated from

$$\cos \theta = \frac{\nabla \alpha^i \cdot \vec{n}_f}{|\nabla \alpha^i| |\vec{n}_f|} \quad (6.13)$$

where  $\vec{n}_f$  is the face normal vector. Face volume fraction  $\alpha_{fA}$  is calculated using normalized values as,

$$\alpha_{fA}^i = \tilde{\alpha}_f^{i*} (\alpha_A^i - \alpha_U^i) + \alpha_U^i \quad (6.14)$$

### 6.1.3 Calculation of Downwind Face Volume Fraction $\alpha_{fU}$

Since the Godunov scheme given in Sections 4.3 and 4.4 requires two volume fractions on either sides of a cell face, a downwind face volume fraction is also needed. This value is shown in Fig. 6.1 as  $\alpha_{fU}$ . According to numerical experimentation we have conducted, different procedures for calculation of  $\alpha_{fU}$  do not have any important effect on the volume fraction resolution. However, the boundedness criteria based on wave propagation defined in Sec. 6.1.1 is valid and should be applied as a limiting value for  $\alpha_{fU}$ . The volume fraction reconfiguration procedure explained in previous sections is still applicable to calculation of  $\alpha_{fU}$ .

One simple way of calculating  $\alpha_{fU}$  could be using the values directly on the downwind side of the face. Another yet more physical method is to assign the values calculated for the upwind side of the face. In doing this the total amount of a phase in the cell must be taken into account, and volume fraction configurations on the faces must be configured in such a way that mass conservation limitation is satisfied. A one simple way of doing this will explained later for multi-dimensional version of the method.

The most robust way of calculating  $\alpha_{fU}$  is to accept  $\alpha_{fU} = \alpha_{fA}$ . Although this assumption does not represent the real expected phasic configuration at the downwind side of the cell face, the missing information by the other phases are propagated by the mechanical relaxation (pressure and velocity relaxation) processes in the cell. These relaxation processes are discussed in Sections 3.2 and 3.3. The advantage of this approach is the elimination of non-conservative throttling terms which will appear for any spatial discretization of volume fraction higher than first order. The elimination of these terms may be the main reason for robustness of this approach. These throttling terms were shown as source terms in the form of volume fraction gradients in Eq. system (3.1).

### 6.1.4 Calculation of Face Courant Number

Proper calculation of the face Courant number  $c_f$  is essential for stability of the solution process.  $c_f$  is calculated for all possible interfaces for all phases  $\Sigma_i$ . The required solution variables  $u_f^i$  and  $\rho_f^i$  are calculated with an HLLC formulation.

$$u_f^{(i,j)} = \begin{cases} u_D^i & \text{if } 0 \leq S_D^{(i,j)} \\ S_*^{(i,j)} & \text{if } S_D^{(i,j)} \leq 0 \leq S_*^{(i,j)} \end{cases} \quad \text{for } j = 1, \dots, N. \quad (6.15)$$

$$\rho_f^{(i,j)} = \begin{cases} \rho_D^i & \text{if } 0 \leq S_D^{(i,j)} \\ \frac{S_*^{(i,j)} \rho_D^i (S_D^{(i,j)} - u_D^i)}{S_D^{(i,j)} - S_*^{(i,j)}} & \text{if } S_D^{(i,j)} \leq 0 \leq S_*^{(i,j)} \end{cases} \quad \text{for } j = 1, \dots, N. \quad (6.16)$$

$c_{fc}$  is taken as the maximum of those for all possible phase interfaces,

$$c_{fc} = \max \left( \frac{u_f^{(i,j)} \rho_f^{(i,j)} A_f}{\rho_D^i V_D}, 0 \right) \quad \text{for all } (\Sigma_i, \Sigma_j), \quad i = 1, \dots, N, \quad j = 1, \dots, N. \quad (6.17)$$

The maximum wave speed  $S_{max}$  required to calculate wave speed based Courant number  $c_{fw}$  is given by

$$S_{max} = \left| \min(S^{(i,j)}, 0) \right| \quad \text{for all } (\Sigma_i, \Sigma_j), \quad i = 1, \dots, N, \quad j = 1, \dots, N. \quad (6.18)$$

$c_{fw}$  is calculated as in Eq. (6.6). The face Courant number  $c_f$  is the maximum of  $c_{fw}$  and  $c_{fc}$ .

$$c_f = \max(c_{fw}, c_{fc}) \quad (6.19)$$

## 6.2 Volume Fraction Discretization On Multi-dimensional Unstructured Grids

The discretization scheme described in Section 6.1 can be extended to multi-dimensional unstructured grids. Since upwind (donor) and downwind (acceptor) cells may not be

readily available in unstructured grids, volume fractions should be extrapolated from the solution data. Another complexity arises on unstructured grids in calculation of the face Courant number.

### 6.2.1 Calculation of Upwind And Downwind Volume Fractions

Since volume fraction is a convected scalar, the local flow direction should be used in the calculation of the upwind and downwind values. In our approach we construct the one upwind and one downwind values for each cell. Hence, all the faces of a cell use the same upwind and downwind values. This differs from the classical approach employed for incompressible flows in which these values are calculated for each face with a simple reconstruction procedure. This approach results in more robust and sharp interface tracking, while it is also more physical. The upwind (donor) and downwind (acceptor) values are reconstructed for the  $x$ - and  $y$ -directions separately, as follows

$$\begin{aligned}
 \alpha_{Ax} &= \alpha_D + \text{sign}(u) (\nabla \alpha_D)_x \Delta S_x \\
 \alpha_{Ay} &= \alpha_D + \text{sign}(v) (\nabla \alpha_D)_y \Delta S_y \\
 \alpha_{Ux} &= \alpha_D - \text{sign}(u) (\nabla \alpha_D)_x \Delta S_x \\
 \alpha_{Uy} &= \alpha_D - \text{sign}(v) (\nabla \alpha_D)_y \Delta S_y
 \end{aligned} \tag{6.20}$$

where  $u$  and  $v$  are the velocity components in the  $x$ - and  $y$ -directions, respectively, and  $\nabla \alpha_D$  is volume fraction gradient in the donor cell.  $\Delta S_x$  and  $\Delta S_y$  are the projections of the donor cell volume on the  $x$ - and  $y$ - axes, respectively.  $\alpha_U$  and  $\alpha_A$  are calculated as,

$$\alpha_A = \frac{|u| \alpha_{Ax} + |v| \alpha_{Ay}}{|u| + |v|}, \quad \alpha_U = \frac{|u| \alpha_{Ux} + |v| \alpha_{Uy}}{|u| + |v|} \tag{6.21}$$

The approximation of the upwind and downwind values by the above approach does, however, not guarantee their boundedness. Our numerical experimentation have shown

that the volume fraction gradient  $\nabla\alpha_D$  should not be limited by a limiter. Otherwise use of any slope limiter results in a more diffusive interface solution. Instead, the calculated values are limited following the procedure given above. The limiting bounds  $\alpha_{min}$  and  $\alpha_{max}$  are derived from the donor cell's nearest neighbors which is given below,

$$\alpha_A = \min \{ \max(\alpha_A, \alpha_{min}), \alpha_{max} \} \quad (6.22)$$

$$\alpha_U = \min \{ \max(\alpha_U, \alpha_{min}), \alpha_{max} \}$$

### 6.2.2 Calculation of Face Courant Number

For multi-dimensional solution grids, face Courant numbers cannot be predicted in isolation of other faces. The convective and acoustic information should be shared between other faces. One simple method is to relate the face Courant numbers  $c_f$  to the cell Courant number  $c_D$ . An effective way of doing this on unstructured grids is given in [54]. The boundedness criteria based on wave propagation can be written as,

$$\alpha_f^i \Delta t (S_{max}^x \Delta S_y + S_{max}^y \Delta S_x) \leq \alpha_D V_D \quad (6.23)$$

where  $S_{max}^x$  and  $S_{max}^y$  are defined as,

$$S_{max}^x = |u| + a, \quad S_{max}^y = |v| + a, \quad (6.24)$$

in which  $a$  is the speed of sound in donor cell. From Eq. (6.23), the face courant number  $c_{fw}$  is written as,

$$c_{fw} = \frac{\Delta t (S_{max}^x \Delta S_y + S_{max}^y \Delta S_x)}{V_D} \quad (6.25)$$

This value is the minimum limit for boundedness and equal to the cell courant number,  $c_D$ . This is an interesting but obvious result for compressible multi-phase flows with

interfaces; for higher resolution of volume fraction one should choose a smaller value for  $c_D$  than the maximum of  $c_D$  which is also equal to the minimum value of  $c_{fw}$ .

### 6.3 Considerations for Dilute Particulate Phases

In most multi-phase flows, dilution of some phases may take place where the volume occupied by one of the phases becomes too small to consider that phase as a continuum. Existence of solid particles in a primary fluid phase is an example of highly diluted phase. In addition to existence of dilution in a fluid, such phases may also be introduced to the flow through boundaries of the domain. Solid propellant rocket motors and ramjet combustion chambers are examples of this kind.

There may be some complications in numerical and mathematical modeling of dilute phases. These difficulties are

- Pressure interaction terms tend to zero for dilute phases due to small volume fractions. This can be seen from Eq. 4.14. Lack of particle interaction terms results in a degenerate hyperbolic system admitting only one characteristic wave for which the speed is the particle speed  $u_p$ .
- Infinitely fast relaxation processes may not be valid for dilute phases. Particulate phases may move at different velocities than the fluid phase. Pressure relaxation may be ignored at dilute regions. However, heat transfer between phases becomes an important phenomena which is usually ignored for multi-fluid applications. Interaction of dilute and primary phases should be reduced to finite rate momentum drag and heat transfer mechanisms.

One way of handling dilute phases is to ignore diluted material volume fraction below a cutoff value. However, most liquid and solid particles may have strong influence on a primary phase carrying those particles, even when the particle volume fractions are below  $10^{-4}$ . Another well known method is to use a Lagrangian approach for particle tracking. However, this method may require tracking of millions of particles for real transient solutions of the flow problems which is almost impractical due to high computational costs. Dilute phase approximation, in which some continuum

equations are derived without pressure-like terms, may be used with the same model problems given above. In this approximation, equations for mass fractions or particle number densities are solved rather than volume fractions.

The scheme presented in this study may be applied to the problems involving diluted phases with the proposed volume fraction capturing algorithm without any modification except for relaxation processes. Below a cutoff volume fraction value relaxation formulations are changed to momentum drag and heat transfer terms in the system given by Eq. (3.1). The most problematic part of this approach is the physical modeling of the transformation from a continuum phase to particle phase. The inverse process of phase dilution is accumulation of some dilute phases (such as particles) to form a continuum phase. Over a threshold value of volume fraction, particulate phases may be considered as a continuum or a porous mix and the pressure relaxation processes may become important. These considerations are out of scope of the present study and may be included as a future work.

#### **6.4 The Algorithm**

Explicit time stepping is done using a four stage Runge-Kutta scheme with optimized stage coefficients as described in [31]. Time step is calculated for each cell according to the stability condition defined as in [54] using standard CFL condition. A CFL number of 2 is sufficient for the stability of the first order scheme with four Runge-Kutta stages. For sharper interface resolution CFL number should be reduced. Each time step is completed through the following algorithm:

1. Calculate face volume fraction values as described in Section 6.1 for a sharper interface. If first order resolution is sufficient for interface capturing or for faster results, this stage may be passed.
2. Calculate residuals with the formulation described in Section 4.4.4,
3. Update solution variables and fluid properties,
4. Relax velocities and update energy,
5. Relax pressures then update volume fractions and energy.

## 6.5 Test Cases for CHRIC Scheme

In this section, some numerical results are provided to show both the accuracy and effectiveness of the high resolution scheme described and discussed in the previous chapter. The first problem is a one dimensional water/air shock tube problem considered for validation of the interface capturing scheme in one dimension. The second problem is similar to the first one, but this time it is in two dimensions. The third and fourth test cases are one and two dimensional particulate flow problems in which the relaxation processes are replaced by momentum and heat transfer laws to show the applicability of the multi-material solver to different multi-phase flow regimes without any modification in the flux solver. All these problems and the attained numerical solutions are presented and discussed below.

### 6.5.1 1D Water/Air Shock Tube Problem

In this test case, a one dimensional shock tube tube problem is considered with a water/air phase interface. The problem setup is the same as that given in [37]. The length of the problem domain is 4 m, with the coordinate range being  $0 < x < 4$  m. The initial position of the water/air interface is at  $x = 2.7$  m. Water and air are modeled as pure fluids in contrast to similar studies found in literature which form the phase interface by a mixture approach using negligible amount of the other phases in the problem. The equations of state (EOS) for water and air are defined as stiffened gasses (SG), as given below

$$p = (\gamma - 1)\rho e - \gamma\pi \quad (6.26)$$

where  $\gamma = 1.4$  and  $\pi = 0$  for air,  $\gamma = 4.4$  and  $\pi = 6 \times 10^8$  for water. The initial conditions of the problem are defined as

$$\begin{aligned} p_w = 1 \times 10^9 Pa, \quad \rho_w = 1000 kg/m^3, \quad \alpha_w = 1.0, \quad \alpha_a = 0.0 \quad \text{for } x < 2.7 \\ p_a = 1 \times 10^5 Pa, \quad \rho_a = 50 kg/m^3, \quad \alpha_w = 0.0, \quad \alpha_a = 1.0 \quad \text{for } x > 2.7 \end{aligned} \quad (6.27)$$

where subscripts  $w$  and  $a$  denote the water and air phases, respectively. The numerical results were obtained on a grid of 1000 cells and with a CFL number of 0.5. This CFL value was chosen for accuracy rather than for stability considerations. In fact, the solution scheme provides sufficient stability up to a CFL number 1.0, but for capturing the interface with sufficiently high resolution in compressible problems, a CFL value of 0.5 or lower should be used. This issue was discussed in Sec. 6.2. The results for various flow properties are shown in Fig.6.3 together with the exact solution. The numerical results are in very good agreement with the exact results. The exact solutions of volume fractions are not shown since they exactly overlap the computed results. The computed phase interface between water and air by the present method is sharper than those computed by similar interface capturing methods such as [37, 1, 2, 46, 42].

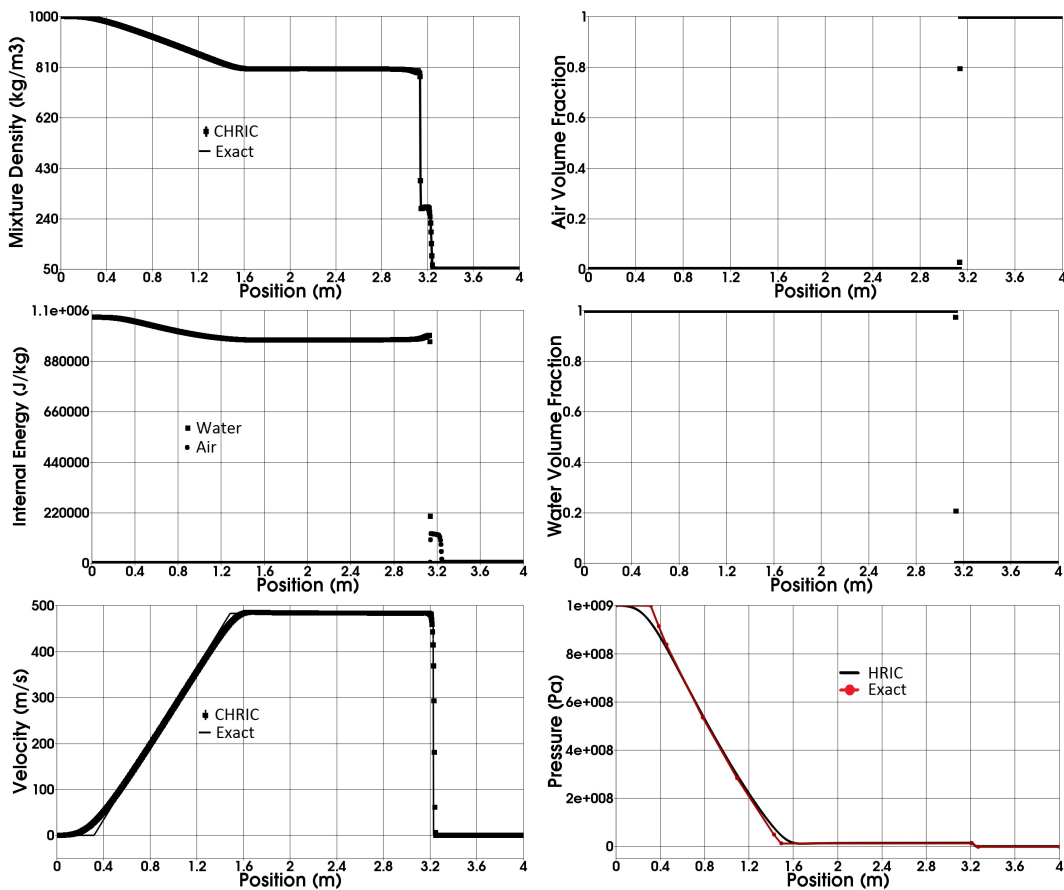


Figure 6.3: Solution of 1D water air shock tube problem at  $t = 900 \mu s$

## 6.5.2 Under Water Explosion

This test problem is concerned with a model underwater explosion problem [46, 19, 21]. The solution domain is a rectangular domain of  $(x, y) \in [-2, 2] \times [-1.5, 1] m^2$ . This domain has three different material zones initially which are illustrated in Fig. 6.4. Initially, there is a water-air interface at  $y = 0$  line and an explosive bubble of radius  $r = 0.12$  m with the center at  $(x, y) = (0, -0.3)$  m in water. The solution grid consists of 100000 cells in total, mostly unstructured. Unstructured solution grid is also shown in Fig. 6.4. As the previous test cases CFL number 0.5 was used.

Air above the water surface is assumed to be a perfect gas at standard atmospheric conditions and defined by

$$p_a = 101325\text{Pa}, \rho_a = 1.225 \text{ kg/m}^3, \gamma_a = 1.4, \alpha_a = 1.0, \quad (6.28)$$

and the explosion gas bubble under the water is also a perfect gas with the state variables given by

$$p_e = 10^9\text{Pa}, \rho_e = 1250 \text{ kg/m}^3, \gamma_e = 1.4, \alpha_e = 1.0, \quad (6.29)$$

while water below the air interface is modeled with the Mie Gruneisen equation of state (Eq. 6.26), and the state variables are given by

$$p_w = 101325\text{Pa}, \rho_w = 1000 \text{ kg/m}^3, \gamma_w = 4.4, \alpha_w = 1.0 \quad (6.30)$$

The initial high pressure of the gas bubble yields a circular shock wave in the water. After this shock wave reaches the water surface, the shape of the water-air interface starts to deform and soon after the circular shape of the gas bubble starts to evolve into an oval shape [19]. The volume fraction solution at  $t = 1.2$  ms is shown in Fig. 6.5. The gas-water interface is again captured at most within two cells which shows the interface capturing ability of the present scheme. This ability is superior to those of the other interface capturing schemes found in literature for compressible flows. In Fig. 6.6, the pressure distributions at times  $t = 0.2, 0.4, 0.6, 0.8$  and  $1.2$  ms

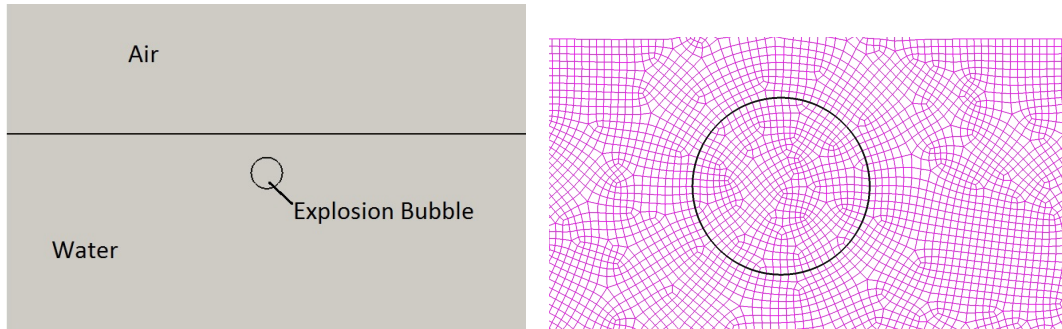


Figure 6.4: Left: Initial material positions for under water explosion problem. Right: Solution grid near the initial gas bubble surface.

are displayed. The captured interfaces at these times are illustrated as white lines on colored pressure contours. The results are very similar to those of others [46, 19, 21].

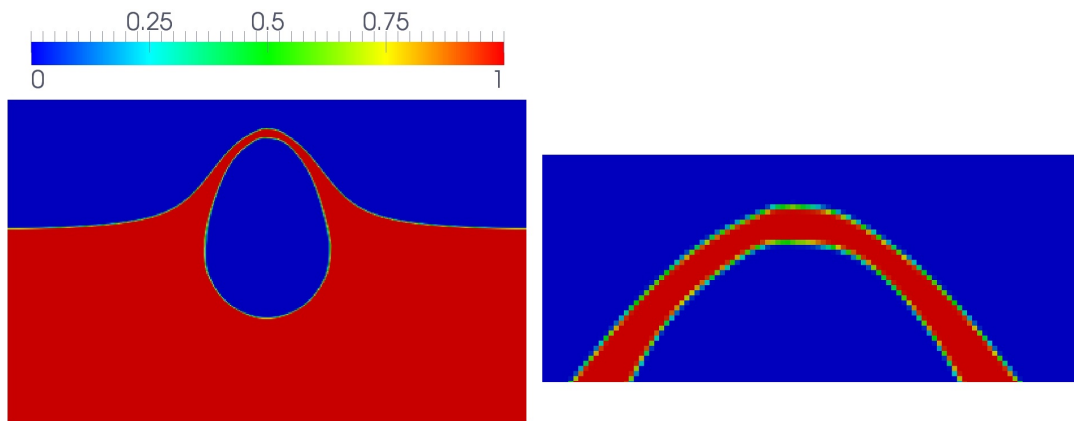


Figure 6.5: Left: Volume fraction solution of underwater explosion problem at  $t = 1.2 \text{ ms}$ . Right: Close-up of the solution.

### 6.5.3 Liquid-Gas Interface Tangential Shock Wave Problem

The previous problem of water-gas interface is a generic problem with applicability of both interface capturing and interface tracking algorithms. In the third test case some interface regions undergo some physical micro scale mixing processes. These micro scale processes may not be resolved with interface tracking algorithms unless very fine meshes (micro scale) are used. Our interface capturing scheme with proper relaxation terms yields physical results in macro scale without a need to resolve the interface in micro scale.

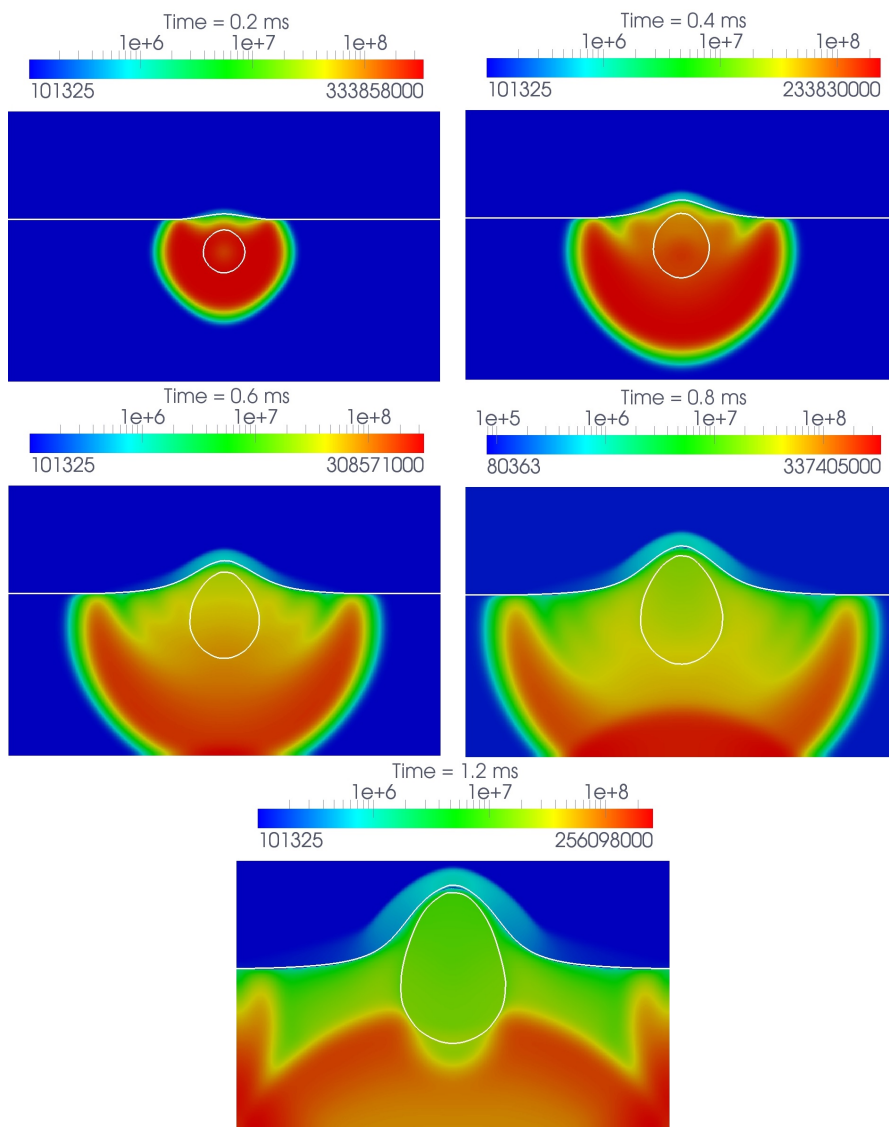


Figure 6.6: Solutions of pressure distribution (Pa) for underwater explosion problem. White lines show material interfaces.

The initial configuration of the problem is shown in Fig. 6.7. There are three fluids in a tube separated by interfaces. Upper right of the tube is filled with gas phase, while the bottom right part of the tube is filled with a liquid. The left part of the tube is filled with a high pressure fluid at  $p = 10^9$  Pa. Since both the gas and liquid phases are considered as compressible, there are two shock waves propagating in both phases. The shock wave in liquid moves faster, and this results in a pressure difference between the gas and liquid phases in the post shock region driving the initial horizontal interface into liquid phase. Transverse waves propagates in gas and liquid phases.

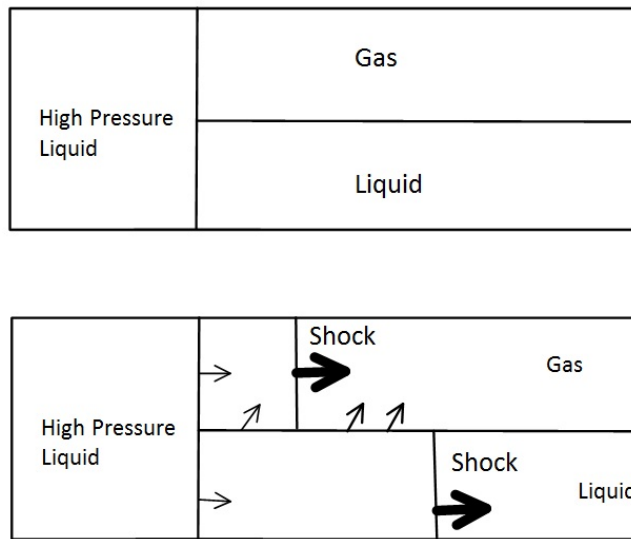


Figure 6.7: Schematic representation of shock tube problem with liquid-water interface.

The solution grid consists of 125000 rectangular cells. As previous example, CFL number of 0.5 was used. A Schlieren like image of the numerical solution at time  $t = 6 \times 10^{-4}$  s is given in Fig 6.8. The complex wave structure due to transverse waves resulting from the pressure difference in the post shock region can be clearly seen in Fig. 6.8. The volume fraction solution at time  $t = 6 \times 10^{-4}$  s is also shown in Fig. 6.9.

A mixing region of the three phases can be seen in Fig. 6.9. This macro scale mixing of the phases is a result of micro scale multi-dimensional processes. These micro scale processes cannot be resolved by the current coarse grid used for the problem using an interface tracking method. These multi-dimensional micro scale motions are

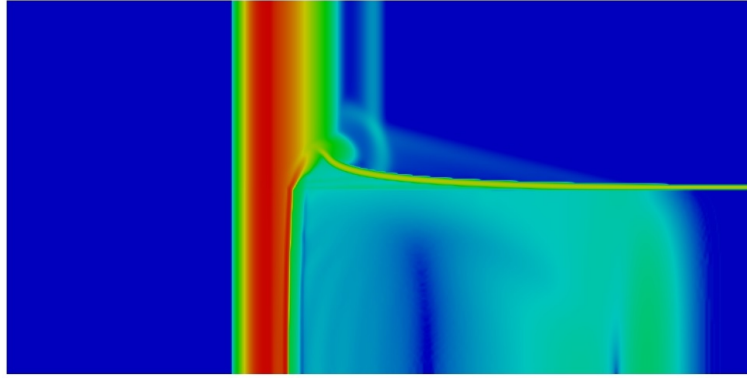


Figure 6.8: Color Schlieren like image (magnitude of the density gradient) of the solution at  $t = 6 \times 10^{-4}$  s.

more deeply considered in [2, 42].

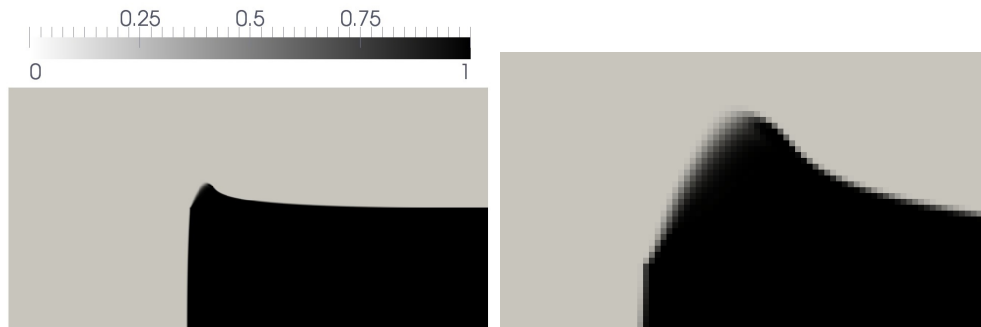


Figure 6.9: Liquid volume fraction at time  $t = 6 \times 10^{-4}$  s. Right is the close-up view of mixing region.

### 6.5.4 Highly Diluted multi-phase Test Cases

Some considerations and applicability of our volume fraction discretization method to particulate phase problems was discussed in Section 6.3. In the next two parts, we give two interesting applications for these types of problems.

#### 6.5.4.1 Attenuation of Acoustic Waves by Suspending Particles

An interesting validation problem for dilute phase models is attenuation of acoustic waves due to particle interactions which is analytically studied by Temkin and Dobbins [47]. The temperature and velocity of a particle suspended in an acoustic field

are subject to fluctuations that may lag behind those of the surrounding fluid [47]. In their paper they present a theory for acoustic attenuation and dispersion in an aerosol-based particulate relaxation processes. Their particulate relaxation theory predicts attenuation and dispersion by small to heavy particles. The predictions by this theory is in close agreement with more detailed theories and existing experimental data [47].

The aim of the test case in this section is to reproduce the results of the analysis explained in [47]. The attenuation and dispersion characteristics of particles of different sizes suspended in a gas phase are studied. The geometry of the channel consists of a simple one dimensional channel. Acoustic waves of 1000 Hz frequency are introduced into the channel. Waves enter the channel with an amplitude of 0.01 % of the mean pressure  $P_0 = 5 \times 10^6$  Pa. A Parametric study is conducted for particle sizes ranging from 1 to  $120 \mu\text{m}$ . Since numerical diffusion may introduce extra non-physical attenuation, a high-order method based on a combination of linear reconstruction and Weighted Average Flux (WAF) [7] is used. This combination of second order methods provides higher resolution than second order methods and 20 finite volume cells per wavelength is sufficient to resolve acoustic propagation with negligible numerical diffusion for the problem. Momentum and heat transfer terms are modeled using Stoke's law [8]. The gas and particle properties used for the simulations are given in Table 5.1.

Acoustic waves are introduced to the domain by a subsonic pressure inlet boundary condition. On the inlet total pressure and total temperature are specified and the outgoing Riemann invariant is used to determine the sound speed. For the outlet of the channel, a non-reflecting boundary condition based on the AUSM scheme [34] was used.

Simulations were carried out for particle diameters of  $R = 5, 8, 10, 12, 15, 18, 20, 30, 40, 80,$  and  $120 \mu\text{m}$ . The results are compared to the analytic solutions based on the method given in [47]. The simulated results are in excellent agreement with theory and the results of the dilute phase model previously given in Chapter 5. In this scheme, although the particle flux terms tends to go to zero due to the flux formula 4.14, volume fractions are still tracked.

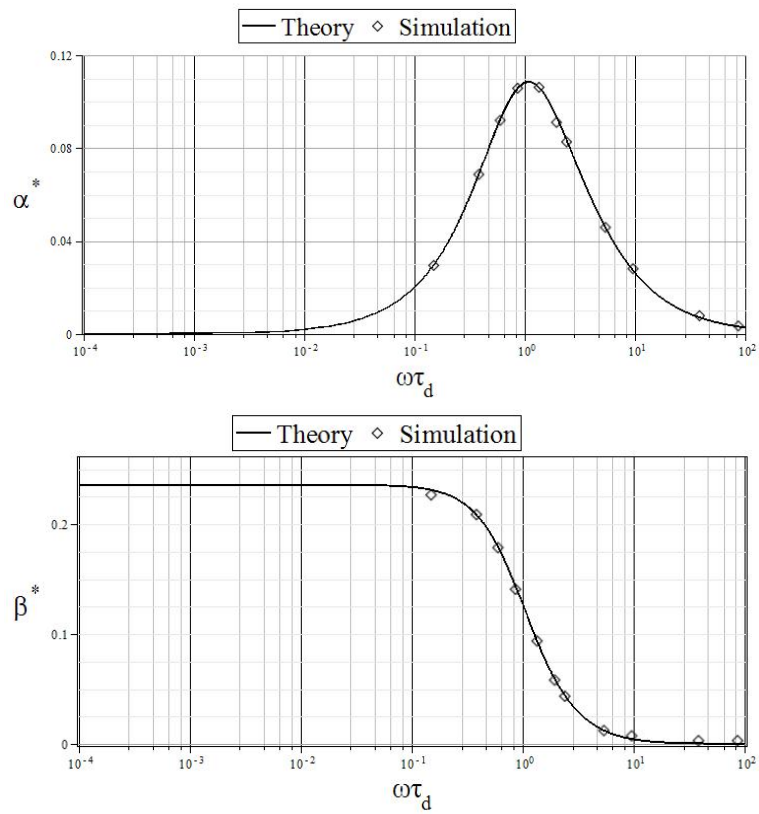


Figure 6.10: Attenuation and dispersion of 1000 Hz acoustic waves due to different sizes of particles suspended in a gas.

### 6.5.4.2 Internal Ballistics of A Solid Propellant Rocket Motor

Another sample problem for dilute phases may be numerical simulation of internal ballistics of solid propellant rocket motors (SPRM). Addition of metal particles to the main ingredient of the solid propellants is very common to increase their internal energy. Fig. 6.11 shows an example computed solution of the volume fraction distribution of the metal particles with the boundary conditions marked for a model motor [27]. Problem was solved on a two dimensional axi-symmetric solution grid. Momentum transfer source terms were calculated using the correlations given in Schiller and Naumann [45]. Similarly, heat transfer source terms were calculated using the correlation given in Ranz and Marshal [39]. The employed values for the gas and material properties are given in Tables 5.2 and 5.3.

At convergence (steady-state) of this kind of problems one usually observes velocity differences between the gas and particle phases because the velocity relaxation for dilute phases is very slow compared to interface problems. The magnitude distribution for the velocity difference  $|V_g - V_p|$  between the gas and particle phases is shown in Fig. 6.12. Temperature differences between these phases are also shown in Fig. 6.12.

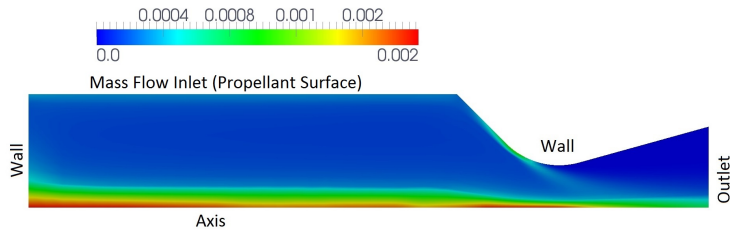


Figure 6.11: Volume fraction distribution of particles in a model SPRM.

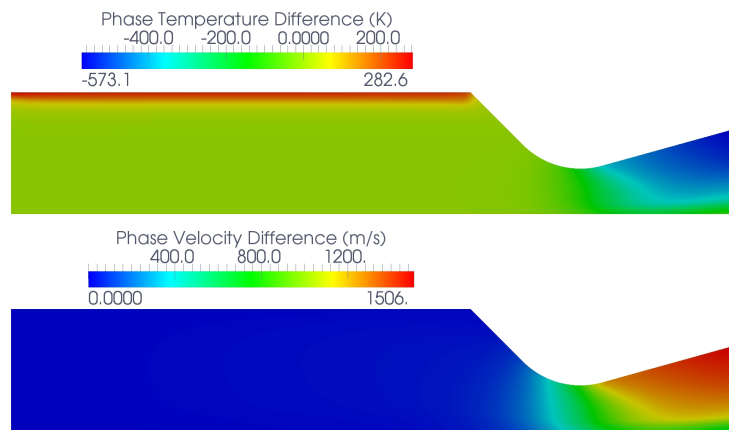


Figure 6.12: Distribution of temperature and velocity differences between gas and particle phase ( $T_g - T_p$  and  $|V_g - V_p|$ ).

## CHAPTER 7

### CONCLUSION

On starting this thesis study, our purpose was to develop a generic discretization method applicable for both compressible interface and compressible mixture problems. This is important because phasic interfaces may undergo micro mixing processes which gradually destroys sharp interfaces and produces mixture regions. This phenomena becomes especially important for high speed flows and explosions which are the main application area of this study.

A novel interface capturing and a generic simulation method for compressible heterogeneous media is developed. The developed differencing scheme used for volume fraction provides comparable resolution of the interfaces with tracking methods on multi-dimensional unstructured grids and very robust compared to other interface capturing methods studied in the related literature. The resulting method provides ignorable numerical mixing of phase interfaces while giving physically correct results for pressure and energy in contrast to other methods available in the literature such as [2, 42, 30, 37]. All the problems associated with the methods given in cited studies are resolved in this thesis study. The method given in [42] is extended to multidimensional problems with more than two phases. Multidimensional and multi-phase versions of the artificial viscosity terms are derived to stabilize the solution of seven equation model used in [42]. Non-conservative terms are discretized with similar methods used to derive the artificial viscosity terms. A new method based on discrete equations is introduced. This method resolves all the problems associated with the non-conservative equations and terms. In contrast to the method given in [2], the application of the method derived in this study to multi-dimensional and

multi-phase problems is very straightforward. The high artificial mixing of interfaces associated with the methods given in [3, 36, 2, 37] are fully resolved. The volume fraction discretization method developed provides the highest possible resolution of phase interfaces (in one cell) even in unstructured tetrahedral meshes when used with the interface capturing methods derived in this study. In addition to these solution methods, some special boundary conditions and preconditioning methods for low speed steady flows were applied. For high spatial resolution, combinations of linear reconstruction and Weighted Average Flux (WAF) methods for unstructured grids were also applied in some problems.

The developed methods can be applied for both interface and mixture problems without any modification. The methods developed in this study may have applications in some other fields including wave propagation with material interfaces such as shallow water equations and plasma flow.

## REFERENCES

- [1] R. Abgrall. How to prevent pressure oscillations in multi component flow calculations: A quasi conservative approach. *J. Comput. Phys.*, 125, 1996.
- [2] R. Abgrall and R. Saurel. Discrete equations for physical and numerical compressible multiphase mixtures. *J. Comput. Phys.*, 186:361–396, 2003.
- [3] G. Allaire, S. Clerc, and S. Kokh. A five-equation model for the simulation of interfaces between compressible fluids. *J. Comput. Phys.*, 181:577–616, 2002.
- [4] M. R. Baer and J. W. Nunziato. A two-phase mixture theory for the deflagration-to-detonation transition (DDT) in reactive granular materials. *Int. J. Multiphase Flow*, 6:861–889, 1986.
- [5] T. J. Bart and D. C. Jespersen. The design and application of upwind schemes on unstructured meshes. *AIAA*, 89-0366, 1989.
- [6] P. Batten, N. Clarke, C. Lambert, and D. M. Causon. On the choice of wave speeds for HLLC riemann solvers. *SIAM J. Scientific Computing*, 18:1553–1570, 1997.
- [7] S. J. Billett and E. F. Toro. On WAF-type schemes for multidimensional hyperbolic conservation laws. *Journal of Computational Physics*, 130:1–24, 1997.
- [8] R. B. Bird, W. E. Stewart, and E. N. Lightfoot. *Transport Phenomena*. John Wiley & Sons, 1960.
- [9] J. Blajek. Computational fluid dynamics: Principles and applications. *Wiley*, 1988.
- [10] A. J. Chorin. Random choice solutions of hyperbolic systems. *J. Comput. Phys.*, 22:517–533, 1976.
- [11] S. Davis. Simplified second-order godunov-type methods. *SIAM J. Sci. Stat. Comput*, 9:445–473, 1988.
- [12] D. Drew. Mathematical modeling of two-phase flows. *Annu. Rev. Fluid Mech*, 15:261–291, 1983.
- [13] D. Drew and S. Passman. *Theory of Multicomponent Fluids*, volume 135 of *Applied Mathematical Sciences*. Springer, New York, 1998.
- [14] J. Dupeys. Proposition of some test cases to validate multiphase codes. *ONERA Presentation*, 2007.
- [15] B. Einfeldt. On godunov-type methods for gas dynamics. *SIAM J. Numer. Anal.*, 25(2):294–318, 1988.

- [16] N. Frink. Recent progress toward a three-dimensional navier-stokes solver. *AIAA Paper*, 94-0061, 1994.
- [17] N. Frink, P. Parikh, and S. Pirzadeh. A fast upwind solver for the euler equations on three-dimensional unstructured meshes. *AIAA Paper*, 91-0102, 1991.
- [18] P. Gaskell and A. Lau. Curvature-compensated convective transport: Smart, a new boundedness-preserving transport algorithm. *Int. J. Numer. Methods Fluids*, 8:617–641, 1988.
- [19] J. Grove and R. Manikoff. Anomalous reflection of shock wave at a fluid interface. *J. Fluid Mech.*, 219:313–336, 1990.
- [20] A. Harten, P. D. Lax, and B. van Leer. On upstream differencing and Godunov-type schemes for hyperbolic conservation laws. *SIAM Review*, 25(1):35–61, 1983.
- [21] D. Harvie and D. Fletcher. A new volume of fluid advection algorithm: the stream scheme. *J. Comput. Phys.*, 162:1–32, 2000.
- [22] O. Heuze. Memoire d’habilitation a driger des recherches. *Universte d’Orleans*, 1997.
- [23] C. Hirsch. Numerical computation of internal and external flows, vol. i: Fundamentals of numerical discretization. *Computers & Fluids*, 34:705–720, 2005.
- [24] D. G. Holmes. Inviscid 2d solutions on unstructured, adaptive grids. numerical methods for flows in turbomachinery. *VKI-LS*, 1989-06, 1989.
- [25] T. Hou and P. L. Floch. Why non-conservative schemes converge to the wrong solution: error analysis. *Math. Comp.*, 62, 1994.
- [26] X. Hu, N. Adams, and G. Iaccarino. On the hllc riemann solver for interface interaction in compressible multi-fluid flow. *J. Comput. Phys.*, 228:6572–6589, 2009.
- [27] B. Kalpakli, J. Dupeys, and Y. Fabignon. NATO RTO-T005 support project ROKETSAN-ONERA. *RTO-AVT Panel Spring 2009*, 2009.
- [28] B. Lafaurie, B. Nardone, C. Scardovelli, R. Zaleski, and G. Zanetti. Modelling merging and fragmentation in multiphase flows with surfer. *J. Comput. Phys.*, 113:134–147, 1994.
- [29] M. H. Lallemand, A. Chinnayya, and O. L. Metayer. Pressure relaxation procedures for multiphase compressible flows. *Int. J. Numer. Meth. Fluids*, 49:1–56, 2005.
- [30] M. H. Lallemand and Saurel. Pressure relaxation procedures for multiphase compressible flows. *Projet M3N, INRIA Rapport de recherche n° 4038*, Octobre 2000.
- [31] B. V. Leer, C.-H. Thai, and K. Powell. Design of optimally smoothing multi-stage schemes for euler equations. *AIAA Paper*, 89-1933, 1989.

- [32] B. Leonard. The ultimate conservative difference scheme applied to unsteady one-dimensional advection. *Comp. Math. in Appl. Mech. and Eng.*, 88:17–74, 1991.
- [33] M.-S. Liou. A sequel to AUSM, part I:  $AUSM^+$ . *Journal of Computational Physics*, 129:137–170, 1996.
- [34] M.-S. Liou. A sequel to AUSM, part II:  $AUSM^+$ -up for all speeds. *Journal of Computational Physics*, 214:137–170, 2006.
- [35] Maplesoft. A division of waterloo maple inc. 2009, <http://www.maplesoft.com>.
- [36] J. Massoni, R. Saurel, B. Nkonga, and R. Abgrall. Propositions de methodes et modeles euleriens pour les problemes a interfaces entre fluides compressibles en presence de transfert de chaleur. *Int. J. Heat Mass Trans.*, 45(6):1287–1307, 2001.
- [37] A. Murrone and H. Guillard. A five equation reduced model for compressible two phase flow problems. *Journal of Computational Physics*, 202:664–698, 2005.
- [38] W. E. Ranz and J. W. R. Marshall. Evaporation from Drops, Part II. *Chem. Eng. Prog.*, 48(4):173–180, April, 1952.
- [39] W. E. Ranz and J. W. R. Marshall. Evaporation from Drops, Part I. *Chem. Eng. Prog.*, 48(3):141–146, March, 1952.
- [40] P. L. Roe. Approximate riemann solvers, parameter vectors, and difference schemes. *J. Comput. Phys.*, 90:141–160, 1981.
- [41] V. Rusanov. Calculation of interaction of non-steady shock waves with obstacles. *J. Comput. Math. Phys. USSR*, 1:267–279, 1961.
- [42] R. Saurel and R. Abgrall. A multiphase godunov method for compressible multifluid and multiphase flows. *J. Comput. Phys.*, 150:425–467, 1999.
- [43] R. Saurel, E. Daniel, and J. C. Loraud. Two-phase flows: Second-order schemes and boundary conditions. *AIAA*, 32:1214–1221, June 1994.
- [44] R. Saurel and T. Gallouet. Modèles et methodes numeriques pour les ecoulements fluides. *Cours de DEA, Centre de Mathematiques et dInformatique, Universite de Provence*, 1998.
- [45] L. Schiller and Z. Naumann. . *VDI Zeits*, 77:318, 1933.
- [46] K. Shyue. A wave-propagation based volume tracking method for compressible multicomponent flow in two space dimensions. *J. Comput. Phys.*, 215:219–244, 2006.
- [47] S. Temkin and R. A. Dobbins. Attenuation and dispersion of sound by particulate-relaxation processes. *The journal of acoustical society of America*, 40:317–324, 1966.
- [48] E. F. Toro. *Riemann Solvers and Numerical Methods for Fluid Dynamics*. Springer, 1997.

- [49] E. F. Toro, M. Spruce, and W. Speares. Restoration of contact surface in the HLL-Riemann solver. *Shock Waves*, 4:25–34, 1994.
- [50] O. Ubbink. Numerical prediction of two fluid systems with sharp interfaces. *PhD thesis submitted to University of London*, 1997.
- [51] P. ˇ Solin, Linz, and K. Segeth. Description of multi-dimensional finite volume solver EULER. *Application of Mathematics*, 47(2):169–185, 2002.
- [52] V. Venkatakrishnan. On the accuracy of limiters and convergence to steady state solutions. *AIAA*, January 1993.
- [53] H. K. Versteeg and W. Malalasekera. An introduction to computational fluid dynamics, the finite volume method. *Harlow: Longman Scientific & Technical*, 1995.
- [54] P. Vijayan and Y. Kallinderis. A 3d finite volume scheme for the eiuler equations on adaptive tetrahedral grids. *J. Comput. Phys.*, 113:249–267, 1999.
- [55] J. M. Weiss and W. A. Smith. Preconditioning applied to variable and constant density flows. *AIAA J.*, 33(11):2050–2057, 1995.
- [56] D. Whitfield and J. Janus. Three-dimensional unsteady Euler equations solution using flux vector splitting. *AIAA Paper*, 84-1552, 1984.
- [57] S. T. Yu. Convenient method to convert two-dimensional CFD codes into axisymmetric ones. *Journal of Propulsion And Power*, 9(3):493–495, May-June, 1993.

# CURRICULUM VITAE

## PERSONAL INFORMATION

**Surname, Name:** Kalpaklı, Bora

**Nationality:** Turkish (TC)

**Date and Place of Birth:** 11-03-1978, Ankara

**Marital Status:** Married

**Phone:** + 90 533 422 27 46

## EDUCATION

<b>Degree</b>	<b>Institution</b>	<b>Year of Graduation</b>
M.S.	Nuclear Engineering, Hacettepe University	2005
B.S.	Nuclear Engineering, Hacettepe University	2002

## PUBLICATIONS

### International Conference Publications

High resolution interface capturing method for compressible multi-phase flows, FEMTEC 2013, Las Vegas, USA.

Multi-phase modeling of missile systems, NATO-RTO Spring Meeting 2012, San Diego, USA.